Engineering Journal

AMERICAN INSTITUTE OF STEEL CONSTRUCTION · FOUNDED 1921 · AISC

Smarter.
Stronger.
Steel.

Engineering Journal

American Institute of Steel Construction

Dedicated to the development and improvement of steel construction, through the interchange of ideas, experiences, and data.

The articles contained herein are not intended to represent official attitudes, recommendations or policies of the Institute. The Institute is not responsible for any statements made or opinions expressed by contributors to this Journal.

The opinions of the authors herein do not represent an official position of the Institute, and in every case the officially adopted publications of the Institute will control and supersede any suggestions or modifications contained in any articles herein.

The information presented herein is based on recognized engineering principles and is for general information only. While it is believed to be accurate, this information should not be applied to any specific application without competent professional examination and verification by a licensed professional engineer. Anyone making use of this information assumes all liability arising from such use.

Manuscripts are welcomed, but publication cannot be guaranteed. All manuscripts should be submitted in duplicate. Authors do not receive a remuneration. Guidelines for authors are printed on the inside back cover.

Engineering Journal (ISSN 0013-8029) is published quarterly. Subscriptions: Members: one subscription, $40 per year, included in dues; Additional Member Subscriptions: $40 per year. Non-Members U.S.: $160 per year. Foreign (Canada and Mexico): Members $80 per year. Non-Members $160 per year. Published by the American Institute of Steel Construction at 130 E Randolph Street, Suite 2000, Chicago, IL 60601.

Subscriptions: subscriptions@aisc.org
312.670.2400

Archives: Search at **aisc.org/ej**.
Article downloads are free for current members and are avaialable for a nominal fee for non-members.

Experimental Investigation into the Capacity of Concentrically Loaded Steel Connections with Pretensioned High-Strength Bolts and Longitudinal Fillet Welds in Combination

Christopher D. Waite, Ligang Shen, Mohamed Soliman, and Bruce W. Russell

ABSTRACT

This paper presents the results of an experimental study aiming to investigate the behavior of steel connections that combine pretensioned high-strength bolts and longitudinal fillet welds on a common faying surface. A total of 75 double-shear tension splices were tested under direct tension loading to quantify the effect of various connection variables on the load-deformation behavior of the connection. These variables include the (1) bolt pattern (2×2 and 2×3), (2) bolt size (¾ in. and 1 in.), (3) bolt grade (ASTM F3125 Grade A325, A490, and F1852), (4) bolt pretensioning method (turn-of-nut and tension control bolts), (5) faying surface class (Class A and B), and (6) weld/bolt strength ratio. The variation in the connection characteristics covered a wide range of weld/bolt strength ratios from 0.50 to 2.00. The bolts were installed in oversized holes, and the specimens were assembled in a negative bearing condition to allow for a maximum slip distance. The load-deformation behavior of the combination connections was recorded and compared to that of the bolted- and welded-only control specimens. In all tests, the addition of welds increased the capacity of the connection. The investigation shows that the capacity of the combination connection with pretensioned high-strength bolts and longitudinal fillet welds can be computed by adding the capacities of the individual connecting elements while considering the strain compatibility.

Keywords: pretensioned high-strength bolts, slip-critical connection, fillet weld, combination connection, double-shear, tension splice, steel connection, experimental testing.

INTRODUCTION

Structural steel connections have been traditionally designed and constructed as either bolted or welded. The need to supplement a bolted connection with welds may arise during retrofit and strengthening of existing structures or in an effort to accommodate a change in design loads after fabrication. Although a weld tensile coupon can exhibit significant deformation, welded connections are generally considered to be stiffer than snug-tightened bolted connections. As a result, if snug-tightened mechanical fasteners are combined with welds in a single

Christopher D. Waite, Design Engineer, Magnusson Klemencic Associates, Seattle, Wash. Email: CWaite@mka.com

Ligang Shen, Graduate Research Assistant, School of Civil and Environmental Engineering, Oklahoma State University, Stillwater, Okla. Email: leon.shen@okstate.edu

Mohamed Soliman, Assistant Professor, School of Civil and Environmental Engineering, Oklahoma State University, Stillwater, Okla. Email: mohamed.soliman@okstate.edu (corresponding)

Bruce W. Russell, Associate Professor, School of Civil and Environmental Engineering, Oklahoma State University, Stillwater, Okla. Email: bruce.russell@okstate.edu

load sharing system, the welds may reach their ultimate capacity within a very small deformation that is not sufficient for bolts to fully engage in the force transfer. Accordingly, the current American Institute of Steel Construction (AISC) *Specification for Structural Steel Buildings* (2016), herafter referred to as the AISC *Specification*, does not allow snug-tightened bolts to be combined with welds. This situation may be exacerbated if transverse welds are used in combination with snug-tightened bolts given the significant decrease in ductility of connections using this weld orientation. Furthermore, the load-deformation behavior of different connecting elements in the elastic range (i.e., stiffness) may not enable the direct addition of the various capacities (Miller, 2001, 2002).

Experimental investigations to quantify the capacity and load-deformation characteristics of connections utilizing bolts and welds in combination began in the late 1960s. One of the earliest known studies into combination connections is highlighted in the *Guide to Design Criteria of Bolted and Riveted Joints*, 2nd Ed. (Kulak et al., 2001). The authors discuss an experimental study by Steinhardt et al. (1969) into the load-deformation behavior of small tension butt splices with bolts and welds in combination. This early study concluded that the connection capacity can be predicted as the sum of the individual bolted-only slip load and the ultimate load of the welded-only connection.

Perhaps the largest research body in literature aiming at characterizing the behavior of combination connections can be attributed to the efforts made by Dr. Kulak and his co-workers. Holtz and Kulak (1970) started this endeavor by investigating how connection variables—that is, weld orientation (longitudinal or transverse), bolt pretension, and bolt hole clearance—influenced the connection performance. Their testing program included three different configurations of double-lap connections that vary the aforementioned connection variables. Although the combination connections implementing transverse welds reached higher capacities than connections with longitudinal welds, the researchers advised against the use of transverse welds in combination connections due to the limited ductility of connections utilizing this weld orientation. Longitudinal welds, however, showed a higher deformation capacity when combined with bolts. The connections without bolt hole clearances provided higher factors of safety than the connections with standard bolt hole clearances. However, these direct bearing bolt conditions are not representative of typical steel construction when standard holes are used.

The effect of weld orientation was further studied through an additional experimental investigation by Jarosch and Bowman (1986). The researchers tested tension splices with pretensioned high-strength bolts employed with varying weld orientation (longitudinal and/or transverse). Again, the study recommended that transverse welds should not be combined with pretensioned high-strength bolts due to the limited ductility of this weld orientation. Additionally, they showed that the frictional resistance of the bolts may not contribute to the overall connection capacity when combined with transverse welds. For their tested connections implementing longitudinal welds, the ultimate capacity was conservatively predicted by summing the weld shear strength and the bolt slip force.

Further investigations were continued by Manuel and Kulak (2000) to study the effect of weld orientation, bolt pretension (pretensioned or snug-tight), and bolt bearing condition. The researchers defined two bearing conditions: positive bearing and negative bearing. For negative bearing, the connection is assembled in a way that allows the bolts to slip over a distance equal to twice the hole clearances before the bolts would engage in bearing. Positive bearing bolts would engage in bearing immediately when load is applied. Similar to previous research, the authors recommended that transverse welds should not be combined with pretensioned high-strength bolts due to ductility limitations of the connections with this weld orientation. The frictional resistance of tested connections was noticeable in the experimental data but not clearly understood. For connections with bolts in positive bearing, certain connections displayed a capacity increase that reached 81% compared with the capacities achieved with the negative bearing condition.

The following model was proposed to estimate the ultimate capacity of a combination connection:

$$R_{ult} = R_{friction} + R_{bolts} + R_{trans.welds} + R_{long.welds} \quad (1)$$

In this model, when pretensioned bolts are utilized, the frictional contribution, $R_{friction}$, is equal to 25% of the total slip resistance of the bolts. When it is certain that the bolts are in negative bearing or when transverse welds are used, the resistance provided by the bolt shear strength, R_{bolts}, is removed from the equation. When the bolts are in positive bearing or intermediate bearing (middle of the hole), R_{bolts} is 75% or 50% of the bolt shear strength, respectively. Lastly, when both transverse and longitudinal welds are used together, the longitudinal weld shear strength, $R_{long.welds}$, is reduced to 85% of the weld shear strength. $R_{trans.welds}$ is equal to the weld shear strength of the transverse welds.

Additional research by Kulak and Grondin (2003) and Sato (2000) sought to understand how the randomness in the bolt bearing condition influenced the accuracy of the model presented in Equation 1. Their testing program included nominally similar connections with pretensioned high-strength bolts and longitudinal welds. During the connection assembly, the bolt bearing condition was not controlled. To test the effectiveness of the model, the bolt bearing condition was classified as intermediate bearing. The model predicted the connection capacities with an average error of 2.4%.

Shi et al. (2011a, 2011b) investigated the ultimate capacity of combination connections both experimentally and numerically. The researchers studied combination connections with pretensioned high-strength bolts in combination with longitudinal and transverse welds. They concluded that the ultimate capacity may be dependent on the ratio a between the bolt slip capacity, $R_{friction}$, and the longitudinal weld capacity, $R_{long.welds}$. The following stepwise model was developed to predict the capacity:

$$R_{ult} = \begin{cases} R_{long.welds} & \text{for } a < 0.5 \\ 0.75R_{long.welds} + R_{friction} & \text{for } 0.5 \leq a < 0.8 \\ 0.9R_{long.welds} + 0.8R_{friction} & \text{for } 0.8 \leq a \leq 2 \text{ , } a = \dfrac{R_{friction}}{R_{long.welds}} \\ R_{long.welds} + 0.75R_{friction} & \text{for } 2 \leq a < 3 \\ R_{friction} & \text{for } a \geq 3 \end{cases} \quad (2)$$

More recently, a study by Kim and Lee (2020) sought to understand how the steel grade, bolt bearing condition, and weld orientation influenced the performance of combination connections. They concluded that the steel grade had little effect on load-deformation behavior of the connection. Similar to previous research conducted by Manuel and Kulak (2000), connections with positive bearing bolts resulted in higher capacities. The researchers proposed the following capacity equation for connections with pretensioned high-strength bolts and longitudinal welds:

$$R_{ult} = 0.8R_{bolts} + UR_{long.welds}, \; U = \begin{cases} 1.0 & \text{for } L \geq 2W \\ 0.87 & \text{for } 2W > L \geq 1.5W \quad (3) \\ 0.75 & \text{for } 1.5W > L \geq W \end{cases}$$

In this model, R_{bolts} is the ultimate strength of the bearing-type bolted connection, and $R_{long.welds}$ is the ultimate shear strength of the welds. Any frictional resistance provided by the connection was neglected to be conservative. The weld strength contribution is multiplied by the shear lag factor, U. This factor is characterized by the variables L and W, which represent the connection length and plate width, respectively.

AISC *Specification* Section J1.8 currently provides guidelines for connections using bolts and welds in combination. The specification allows combining pretensioned high-strength bolts and longitudinal fillet welds in shear connections with common faying surface. The available strength is permitted to be taken as the sum of the bolt slip capacity and the longitudinal fillet weld strength. The specification imposes limitations on the percentage of force carried by the bolts and welds given the bolt pretensioning method.

The AISC *Specification* nominal slip resistance of the bolts, R_{nb}, is defined as:

$$R_{nb} = \mu D_u h_f T_b n_s$$

(AISC *Spec.* Eq. J3-4)

in which μ is the mean slip coefficient for Class A or B surfaces; D_u is a multiplier that reflects the ratio of the mean installed bolt pretension to specified minimum bolt pretension, taken as 1.13; h_f is a factor for filters; T_b is the minimum fastener pretension force; and n_s is the number of slip planes in the connection.

The AISC *Specification* nominal shear strength of the weld, R_{nw}, is defined as:

$$R_{nw} = F_{nw} A_{we}$$

(AISC *Spec.* Eq. J2-3)

where $F_{nw} = 0.6 F_{EXX}$ for fillet welds (from Table J2.5) and A_{we} is the effective fillet weld area. F_{EXX} is defined as the filler metal classification strength. The effective fillet weld area, A_{we}, is equal to the effective weld length multiplied by the effective weld throat. The throat is the shortest distance from the weld root to the face of the fillet weld.

Although previous research provides several models for predicting the capacity of connections with bolts and welds in combination, the combined connection behavior is still not fully understood. For instance, the contribution of the bolt slip capacity is not well characterized. While Shi et al. (2011b) recommended using the slip capacity as the bolt contribution, Kim and Lee (2020) advocated against its use, and the model proposed in Manuel and Kulak (2000) uses only 25% of this friction force. It is also apparent in literature that the positive bearing condition led to a higher connection capacity; however, it may not be practical to specify that combination connections must be assembled in a positive bearing condition. Based on this discussion, it seems that the effects of the plate steel grade and weld orientation are well understood. Furthermore, there exist additional connection variables that may also influence the behavior of the combination connection. These include bolt pattern, bolt size, bolt grade, pretensioning method, and faying surface class. Additionally, further experimental work is necessary to fully understand and quantify the influence of the weld/bolt strength ratio. The comprehensive experimental testing program discussed herein investigates these connection variables.

EXPERIMENTAL TESTING PROGRAM

In this paper, the behavior of connections with bolts and welds in combination was studied experimentally through a testing program encompassing 75 double-shear tension splice connections. The connections were loaded in a direct tension test frame that was designed and constructed for this study. This section illustrates the test specimens as well as the experimental methods used for the research program.

Test Connection Matrix and Specimens

The connections included in this study are separated into groups according to the connection bolt pattern and faying surface class. These connections are highlighted in the test connection matrix depicted in Table 1. Of the total connections tested, 30 were either bolted only or welded only. These tests are classified as ancillary and were utilized to establish experimental material characteristics such as the bolt pretension, slip coefficient, and weld shear stress. The remaining 45 connections in the test matrix combine pretensioned high-strength bolts and longitudinal fillet welds. For these connections, the following test variables were investigated: bolt size, bolt grade, pretensioning method, faying surface class, and, more importantly, the weld/bolt strength ratio. Each test consisted of three connection samples to better characterize the statistical variability of the capacity and how it is affected by the variability of various input parameters. As will be seen later in this paper (e.g., Figure 8), due to this variability, several connections would show a capacity that is equal to or higher than other connections with larger weld size. Accordingly, simply testing one specimen from each configuration would have not provided data that enables understanding the combinational behavior. Further, the proper consideration of this variability allows for predicting the reliability of these connections. The connection samples in the test series were named A, B, and C (e.g., 1A, 1B, 1C.). Additional samples were added to Test 1 and Test 16 to better understand the randomness

	Test No.	Bolt Pattern	Bolt Grade	Bolt Pretensioning Method	Faying Surface Class	Weld Geometry	Weld/Bolt Strength Ratio	Number of Samples
Table 1. Test Connection Matrix								
Bolted only	1	2×2	A325	ToN	B	—	—	5
	2	2×2	A325	ToN	A	—	—	3
	3	2×2	A490	ToN	B	—	—	3
	4	2×2	A325	TC	A	—	—	3
	5	2×2	A490	ToN	A	—	—	3
Welded only	6	—	—	—	—	⁵⁄₁₆ × 3.0	—	3
Bolted and welded	7	2×2	A325	ToN	B	⁵⁄₁₆ × 5.0	1.50	3
	8	2×2	A325	ToN	B	⁵⁄₁₆ × 2.25	0.67	3
	9	2×2	A325	ToN	B	⁵⁄₁₆ × 3.5	1.00	3
	10	2×2	A325	TC	B	⁵⁄₁₆ × 2.25	0.67	3
	11	2×2	A490	ToN	B	⁵⁄₁₆ × 2.75	0.67	3
	12	2×2	A325	ToN	A	⁵⁄₁₆ × 1.25	0.67	3
	13	2×2	A325	ToN	A	⁵⁄₁₆ × 2.0	1.00	3
	14	2×2	A325	ToN	A	⁵⁄₁₆ × 3.0	1.50	3
	15*	2×2	A325	ToN	A	⁵⁄₁₆ × 3.5	1.00	3
Bolted only	16	2×3	A325	ToN	A	—	—	5
Welded only	17-2	—	—	—	—	⁵⁄₁₆ × 2.0	—	3
	17-4	—	—	—	—	⁵⁄₁₆ × 4.0	—	2
Bolted and welded	18	2×3	A325	ToN	A	⁵⁄₁₆ × 2.0	0.67	3
	19	2×3	A325	ToN	A	⁵⁄₁₆ × 3.0	1.00	3
	20	2×3	A325	ToN	A	⁵⁄₁₆ × 4.0	1.33	3
	21	2×3	A325	ToN	A	⁵⁄₁₆ × 6.25	2.00	3
	22	2×3	A325	TC	A	⁵⁄₁₆ × 3.0	1.00	3
	23	2×3	A490	ToN	A	⁵⁄₁₆ × 2.0	0.50	3

NOTE: All bolts are ¾ in. diameter (oversized holes) unless noted otherwise.
TC = tension control bolt; ToN = turn-of-nut method
Four fillet weld lines of the specified geometry per connection. Units are inches.
* Bolts are 1-in.-diameter Grade A325 in oversized holes.

of the steel friction coefficient. Test 17 also included additional samples to record the experimental load-deformation behavior of welds with different lengths.

The test matrix in Table 1 outlines the specific variables studied for each connection type. All connections utilized ¾-in.-diameter bolts, except Test 15 where 1 in. bolts were used. For the bolt grade, either A325 or A490 pretensioned high-strength bolts were used, which represent ASTM F3125 Grade A325 and Grade A490 (ASTM, 2021b), respectively. The pretensioning methods included both the turn-of-nut method (ToN) as well as tension control (TC) bolts (i.e., ASTM F3125 Grade F1852). All bolts used in the test program are Type 1 bolts. Class A connections utilize plates with clean mill scale, while Class B connections are classified as SSPC-SP6 commercial blast-cleaning in the AISC *Steel Construction Manual* (2017), hereafter referred to as the AISC *Manual*. The Class B plates were blast-cleaned by the steel fabricator and were free of all visible rust, mill scale, paint, and foreign matter. All welded-only and combination connections include four equal length longitudinal fillet welds, with a ⁵⁄₁₆ in. weld leg size, using a E70 weld electrode. A ⅛ in. Lincoln Electric E7018 H4R weld electrode was used with the shielded metal arc welding (SMAW) process. Each weld length was specifically designed to achieve a target weld/bolt strength ratio ranging from 0.50 to 2.00, depending on the test. The ratio was computed based on the nominal capacity of connecting bolted-only and welded-only connections.

Each test specimen is composed of three components: the tested connection, the anchorage zone, and the connection grip. Figure 1 shows the typical 2×2 and 2×3 test specimen and highlights the aforementioned components. The tested connection zone indicates the portion of the sample that is to be studied and corresponds to the designated test characteristics highlighted in Table 1. The bolts in this zone are pretensioned and are placed in oversized holes to allow the connection to slip over a longer distance. This leads to a better understanding of the load-deformation behavior of the joint. The bolts in the anchorage zone are placed in standard holes and work in bearing. Finally, a large pin in the connection grip provides an attachment mechanism for the specimen to the load frame to minimize loading eccentricities. The steel used for all specimen plates is ASTM A572 Gr. 50 (ASTM, 2021a).

Experimental Methodology

A direct tension load frame, shown in Figures 2 and 3, was designed and constructed for this study. The frame is self-reacting and is hung off a W30×99 top header beam that is supported on either side with supplemental framing support. The load application occurs on each side of the test specimen through a load column that is attached to the top and bottom header beams. The bottom header beam is made up of two W24×66 sections. Each load column consists of a hydraulic cylinder, load cell, and filler column made of four HSS3×3×⅜ and two end plates. Each hydraulic cylinder was retrofitted with servo valves and a linear variable displacement transducer (LVDT) to be controlled with an MTS FlexTest 60 controller. During the load application, the actuators extend simultaneously at a rate of 0.02-in./min. This rate was adopted to simulate a static loading condition and is similar to the test rate adopted by Holtz and Kulak (1970). This actuator displacement rate also ensured that the average slip rate of the connections was below 0.003-in./min as recommended by the Research Council on Structural Connections (RCSC, 2020). This extension lowers the bottom header beam and applies direct tension to the specimen.
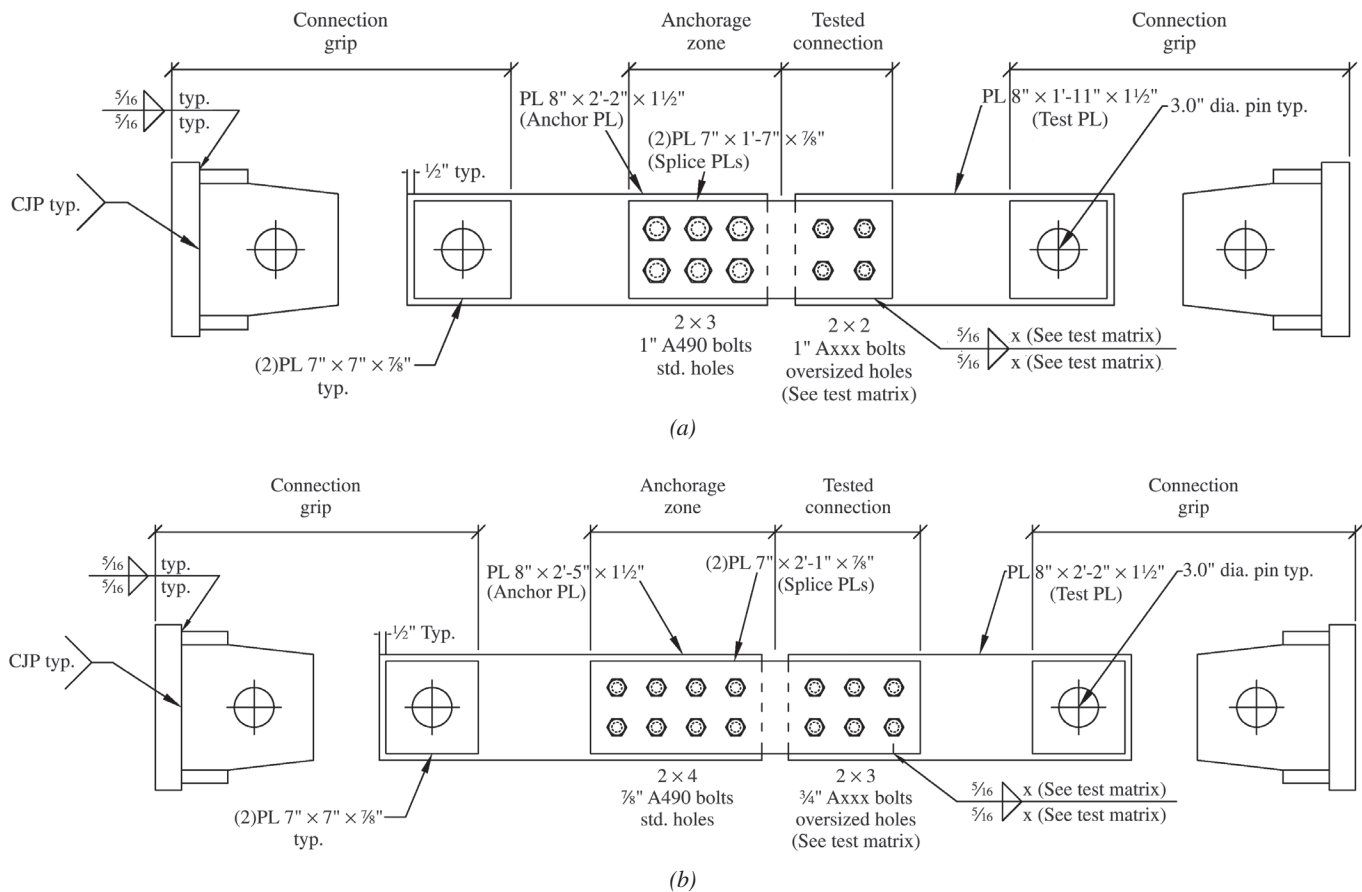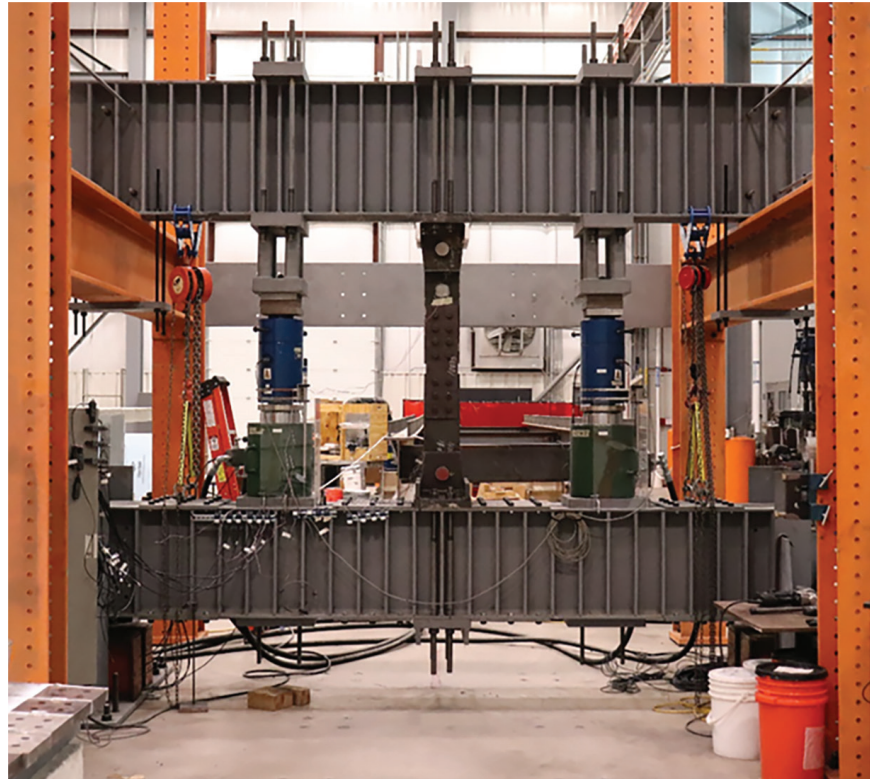

Fig. 1. Details of test specimens.
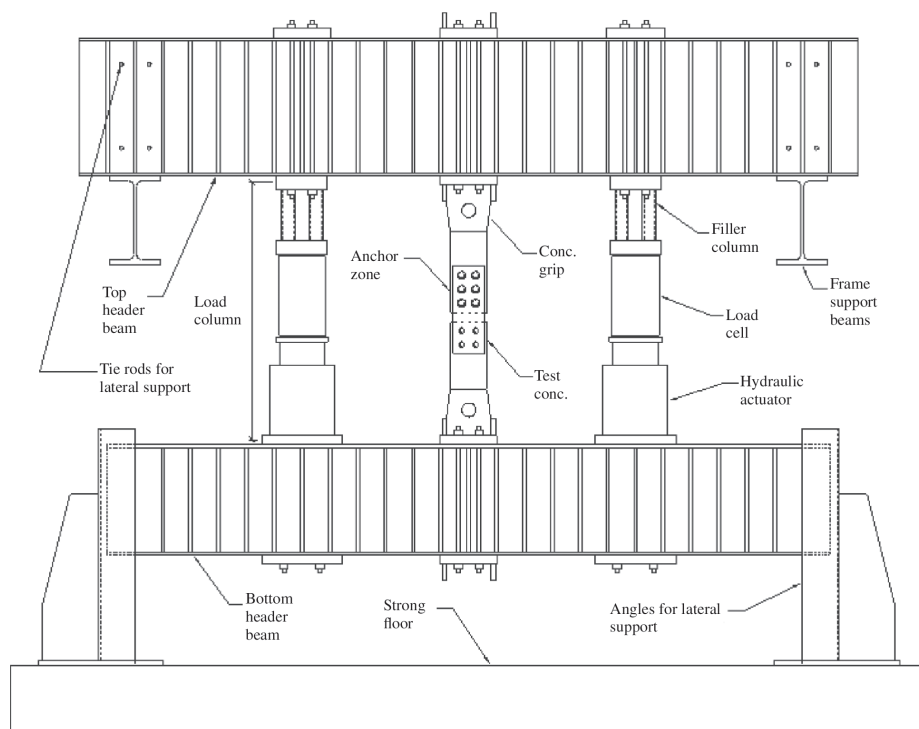
Fig. 2. Experimental test frame.

Fig. 3. Experimental test frame details.

Each connection was instrumented with bolt load cells, LVDTs, and strain gauges, as shown in Figure 4. Four high-accuracy AC-LVDTs, with a stroke of 0.20 in., measure the relative displacement between the connection components (i.e., slip) and are located at the bottom corners of each splice plate. The total slip of the connection is measured as the average of the four AC-LVDTs. Two global DC-LVDTs measure the separation of the top and bottom center plates. These devices capture the slip behavior of the connection past the limits of the AC-LVDTs (i.e., 0.20 in. of slip). Each bolt was fitted with a bolt load cell to verify that the minimum pretension was provided and to monitor the bolt pretension during the test. Finally, strain gauges were applied to the tested connection to monitor the strains during testing. Additional gauges were applied in the anchorage zone to detect any load eccentricity. A National Instruments NI-cDAQ-9178 was used in conjunction with LabVIEW NXG (NI, 2018) to record all instrumentation data.

A testing protocol was developed to ensure that all specimens were tested consistently. Before connection assembly, all faying surfaces were cleaned to remove any media that could contaminate the surface. The bolted connection in the anchorage zone was assembled in positive bearing, while the tested connection was assembled in negative bearing. Because literature indicated that connections assembled

in positive bearing provide higher capacities (Manuel and Kulak, 2000), the negative bearing condition was chosen for the tested zone to provide a lower bound of the capacity and to allow for the accurate investigation of the bolt frictional contribution to the capacity and load-deformation behavior of the connection.

Before the test connection bolts were pretensioned, three additional bolts that represent the test bolt group (A325/A490 and ToN/TC) were tested in a bolt tension measurement device, and their pretension data was recorded. These additional tests ensured that the pretensioning equipment was operating properly and provided supplemental bolt pretension data. All ToN bolts were pretensioned with a turn-of-nut wrench, and all TC bolts were pretensioned with a shear wrench. After bolt pretensioning, the connections were welded by a certified welder according to the test matrix, and their lengths and leg dimensions were measured. The leg dimension measurements were taken at three locations along the weld length and were used to estimate the experimental effective throat of the fillet weld. An effective throat computation was adopted from Salmon et al. (2009) and accounted for unequal leg size geometry. Finally, all strain gauges and LVDTs were placed on the connection according to the instrumentation plan in Figure 4.

ANCILLARY TESTING

In order to properly evaluate the capacity of the combination connections, several ancillary tests were completed throughout the research program to establish the following experimental test variables:

T_b = bolt pretension force, kips
μ = slip coefficient of tested plates
τ = weld shear strength

These experimental test variables allow for the proper prediction of the capacity of the connection based on actual material characteristics rather than nominal values.

Pretension Evaluation

Slip-critical bolted connections rely on the frictional forces developed between the faying surfaces for strength. This resistance is both a function of the steel frictional coefficient and the bolt pretension. Throughout the testing program, 201 bolt pretension tests were conducted over a range of bolt styles, grades, and sizes. Before every connection test, three bolts were tested in a bolt tension measurement device. Moreover, the pretension force of the ¾ in. bolts was recorded using washer-type bolt load cells. The load cells were installed on the nut side. The bolt load cell model is Omega LC901-¾-65K. These load cells also come with a conical washer to center the load cell as the nut is being tightened. Both the bolt pretension tests and the bolt load
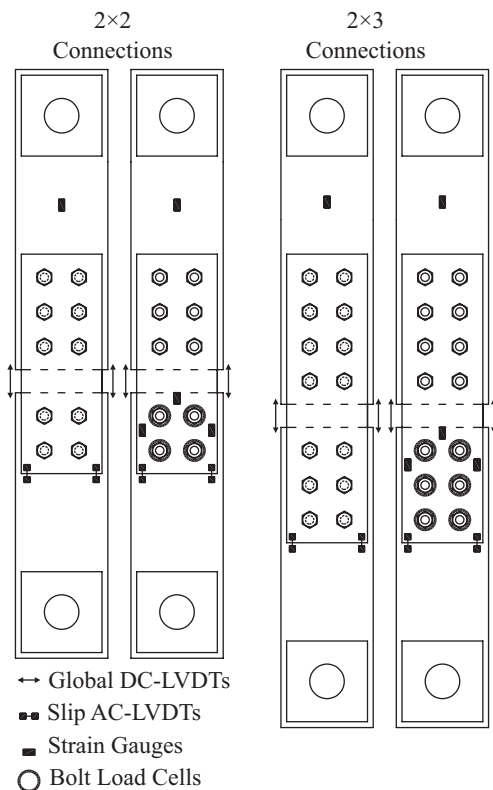

Fig. 4. Specimen instrumentation layout.

Table 2. Bolt Pretension Test Probabilistic Measurements				
	¾ in. A325-ToN	¾ in. A325-TC	¾ in. A490-ToN	1 in. A325-ToN
Number of samples	129	27	36	9
AISC minimum pretension* (kips)	28	28	35	51
Mean value (kips)	42.7	38.5	46.8	64.1
Standard deviation (kips)	1.99	2.76	2.30	3.07
NOTE: TC = tension control bolt; ToN = turn-of-nut method * Table J3.1 (AISC, 2016)				

cell measurements provided insight into the experimental bolt pretension that is applied to the connection and ensured that the pretensioning was completed properly.

During the testing program, it was noted that the pretension data from the bolt load cells displayed higher amounts of variability than the bolt pretension test data. For example, the bolt tension measurement device recorded an average pretension of 42.7 kips with a standard deviation of 1.99 kips for the A325 ToN bolt group, whereas the bolt load cells recorded an average pretension of 39.3 kips with a standard deviation of 5.42 kips for this same bolt group. After benchmarking the results of the bolt load cells against those obtained from the bolt pretension test of the bolts from the same lot, it was determined that the higher variability in these measurements can be attributed to the load cell measurement accuracy. Because no probabilistic analysis is performed to account for this variability in this paper, it was decided to use the bolt pretension readings in the capacity prediction models presented herein. The variability in bolt load cell data was properly captured in developing a probabilistic approach to investigate the reliability of these connections in Khandel et al. (2022). Table 2 shows the experimental bolt pretension data from the bolt pretension tests. The mean experimental pretension values were used to evaluate the steel fictional coefficient as well as the predicted capacity of the combination connections.

Bolted-Only Tests and Friction Coefficient Evaluation

The testing program included 22 bolted-only connection samples that were used to evaluate both the steel frictional coefficient used in the study, as well as develop a baseline for bolted-only connection behavior. The test characteristics of the bolted-only connections correspond to Tests 1–5 and Test 16 in the connection matrix shown in Table 1. The RCSC (2020) provides typical load-slip curves for slip-critical bolted connections. These curves are illustrated in Figure 5 and were adopted to determine the slip load of the connections. The slip load corresponds to the maximum load before 0.02 in. of slip for connections following Case a, the load before sudden slip for Case b, and the load at 0.02-in. of slip for Case c.

The bolted-only connections with Class A surfaces displayed load-slip behaviors similar to Case c while Class B surfaces displayed a slip response similar to Case a. However, it should be noted that two of the 2×3 Class A specimens displayed a behavior similar to Case a. The slip load for each bolted-only connection was identified based on these outlined behaviors. Typical bolted-only load-slip curves are presented in Figure 6 for Class A and Class B surfaces (Tests 5 and 3, respectively) and the experimentally obtained connection capacities, denoted by Test R_n in this paper, are shown in Table 3. Note that the deformation levels at which slip occurs are significantly lower than those occurring at the failure of a bearing-type bolted connection. Using the slip load for each test connection, the slip coefficient, k_s, is computed for each sample as:

$$k_s = \frac{slip\ load}{2 \times clamping\ force} \qquad \text{(RCSC Eq. A3.1)}$$

where the *clamping force* is equal to the average bolt pretension pretension force (see Table 2) multiplied by the number of bolts used in the connection. Table 3 presents a summary of this computation for each bolted-only connection. Note that separate computations for the 2×2 Class A and 2×3 Class A surfaces were required due to the different behavior observed during the bolted-only tests for the two groups of plates. The plates used for the 2×2 Class A surfaces displayed a more uniformly textured oxide layer than the plates used for the 2×3 Class A connections. The properties of the oxides layer (e.g., uniformity, chemical composition, adhesion, etc.) may have led to this difference in the load-slip behavior of the connections.

For each faying surface group, the experimental slip coefficient, μ, was identified as the average of all individual slip coefficients, k_s, for connections in the group. The slip coefficients for both the 2×2 and 2×3 Class A surfaces were higher than the AISC *Specification* minimum of 0.3. The 2×2 Class A surface was found to have an average slip coefficient of 0.457. The test data was very consistent with a standard deviation of 0.022 and coefficient of variation of 4.87%. Unlike the 2×2 Class A friction data, the 2×3 Class A data displayed high variability with a mean slip
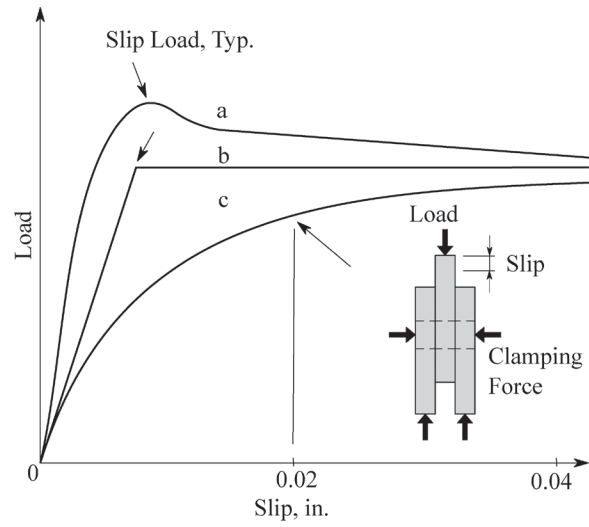
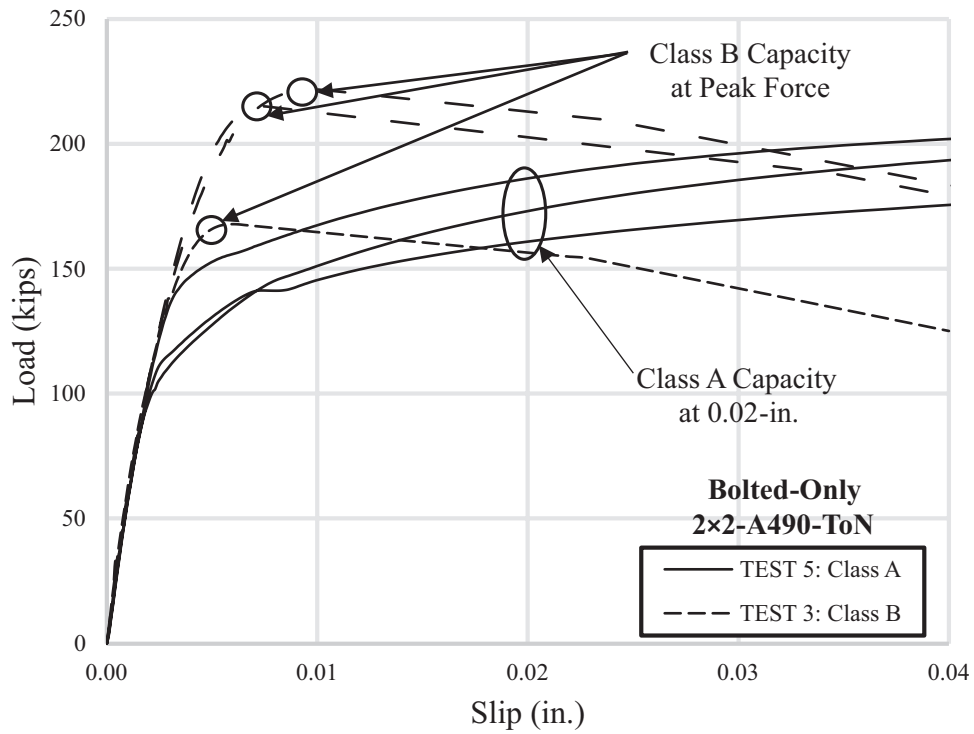*Fig. 5. RCSC load-slip definition (RCSC, 2020).*

Fig. 6. Bolted-only experimental load-slip curves.

Table 3. Slip Coefficient Evaluation					
Faying Surface	**Bolt Type**	**Test**	**Bolt Pretension (kips)**	**Clamping Force (kips)**	**Test Rn (kips)**	**Slip Coefficient k_s**
2×2 Class A	A325 ToN	2A	42.7	171	153	0.446
		2B			158	0.462
		2C			145	0.424
	A325 TC	4A	38.5	154	143	0.465
		4B			146	0.474
		4C			139	0.452
	A490 ToN	5A	46.8	187	173	0.462
		5B			161	0.430
		5C			186	0.497
						AVG = 0.457 **SD = 0.022** **CV = 4.87%**
2×2 Class B	A325 ToN	1A	42.7	171	189	0.552
		1C			142	0.414
		1D			181	0.530
		1E			217	0.636
	A490 ToN	3A	46.8	187	168	0.448
		3B			222	0.592
		3C			215	0.575
						AVG = 0.535 **SD = 0.079** **CV = 14.8%**
2×3 Class A	A325 ToN	16B	42.7	256	170	0.331
		16C			169	0.329
		16E			183	0.357
NOTE: All bolts are ¾ in. diameter (oversized holes) unless noted otherwise. TC = tension control bolt; ToN = turn-of-nut method AVG = average; SD = standard deviation; CV = coefficient of variation						**AVG = 0.339** **SD = 0.016** **CV = 4.61%**

coefficient of 0.382 and resulted in a standard deviation of 0.079 and a coefficient of variation of 16.3%. To improve confidence in the slip coefficient prediction for the 2×3 Class A surface, a two-tailed Z-test was conducted using slip coefficient data described in Grondin et al. (2007) where a mean value of 0.301 was reported for Class A surfaces. For the Z-test, the null hypothesis was that the mean value of the slip coefficient calculated from the experimental test data was equal to the value reported by Grondin et al. (2007); an alternative hypothesis was that the two values were not equal. Two samples were rejected (16D and 16F) from the 2×3 group with a 90% significance level based on the hypothesis test. A mean slip coefficient of 0.339 was calculated based on the remaining three tests.

Similar to the Class A surfaces, the Class B surface produced an experimental slip coefficient that exceeded the AISC *Specification* minimum of 0.5, but with higher variability. The 2×2 Class B surface displayed a slip coefficient of 0.535 with a standard deviation of 0.079 and coefficient of variation of 14.8%. Note that specimen Test 1B was removed from the study due to a faying surface contamination (hydraulic oil) that would be unlikely to occur under typical construction field conditions. The slip coefficient computed in this ancillary test was found to be very close to the mean value of 0.524 reported by Grondin et al. (2007); however, additional statistical analysis was performed to gain confidence in the slip coefficient prediction. A similar two-tailed Z-test was conducted for the Class B surface data and a *p*-value was computed as 0.764. Accordingly, the obtained experimental mean was considered to belong to the population distribution. Although these tested Class B bolted-only connections included only four bolts,

the slip level at which the first slip event occurred was found to be comparable to experimental results of bolted connection with 32 bolts reported in Borello et al. (2009). These experimental slip coefficients were used to evaluate and predict the slip contribution into the combination connections capacity.

Welded-Only Tests and Weld Shear Strength Evaluation

In addition to the bolted-only connection tests, eight welded-only tests were conducted to evaluate the experimental weld shear strength. These tests include Tests 6 and 17 in the connection test matrix and cover weld lengths of 2, 3, and 4 in. The experimental load-deformation curves for the welded connections are depicted in Figure 7. These curves show similar profiles compared to those reported by Lesik and Kennedy (1990). The ultimate capacity of these connections corresponds to the maximum load sustained during the test.

To compute the experimental weld shear stress, AISC *Specification* Equation J2-3 was adopted and rearranged to solve for the stress. In this equation, R_{nw} corresponds to the test connection ultimate capacity and A_{we} to an effective fillet weld area. This effective fillet weld area is equal to the measured fillet weld length multiplied by the average effective throat. The average effective throat was computed

from the weld measurements of all the welded-only and combination tests and was found to be 0.194 in. with a standard deviation of 0.012 in. and a coefficient of variation of 6.13%.

The welded-only connection data highlighted in Table 4 provides the weld shear stress computation for each individual connection. Overall, this data concluded that the experimental weld shear strength is approximately 69.5 ksi with a standard deviation of 3.77 ksi and a coefficient of variation of 5.42%. This weld shear stress is roughly 30% higher than previous experimental work reported in literature for the similar E70 filler metal (Manuel, 1996). The high shear stress computed from the welded-only test data can be attributed to the higher mechanical properties of the weld electrodes used in the study and the use of the pre-fracture measured effective weld area. The higher mechanical properties of the weld electrodes were confirmed by the results of two weld coupons that were fabricated and tested according to AWS B4 (2016). These weld specimens showed a yield stress of 74 ksi and ultimate stress of 83 ksi. As noted in the literature (e.g., Deng et al., 2003), the actual fracture area of the weld is approximately 27% larger than the effective pre-fracture area. A similar value was also observed in this research program. Accordingly, using the actual fracture area would lead to a significantly lower shear stress value. However, since the pre-fracture area is
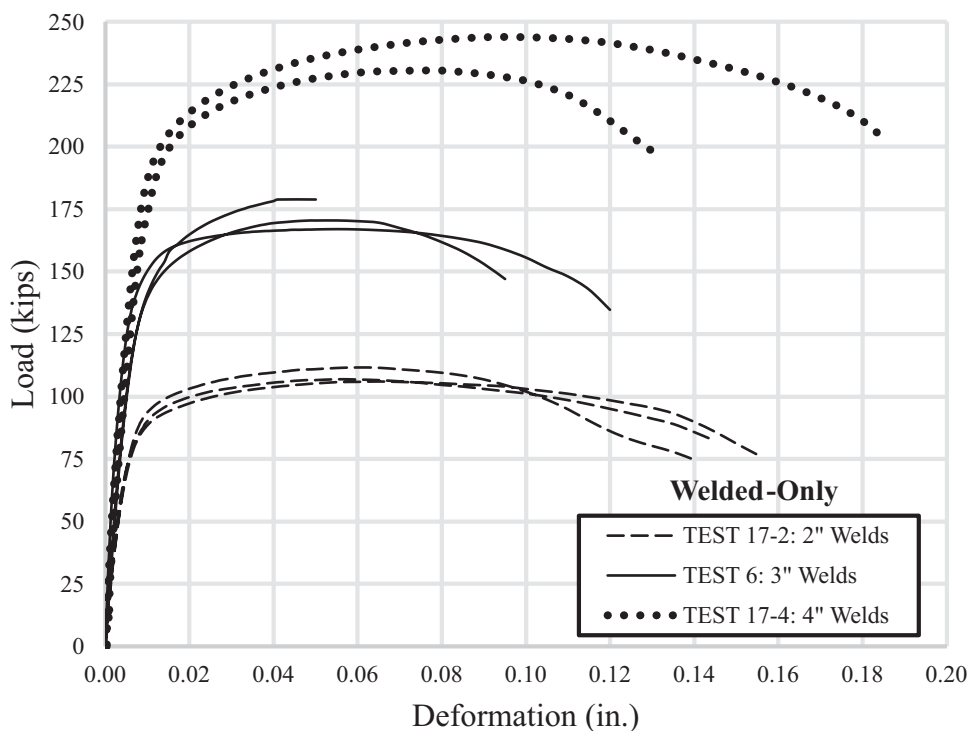

Fig. 7. Welded-only experimental load-deformation curves.

Table 4. Weld Shear Strength Evaluation				
Weld Size	**Test**	**Effective Throat Area (in.^{2})**	**Test Rn (kips)**	**Weld Shear Stress (ksi)**
⅝₆ × 3 in.	6A	2.49	181	72.5
	6B	2.47	170	68.9
	6C	2.36	167	70.8
⅝₆ × 2 in.	17-2A	1.65	107	65.0
	17-2B	1.64	112	68.0
	17-2C	1.65	106	64.2
⅝₆ × 4 in.	17-4D	3.23	231	71.4
	17-4E	3.23	244	75.4
NOTE: Four fillet weld lines of the specified geometry per connection. Units are inches. Average effective weld throat: 0.194 in.			AVG = 69.5 SD = 3.77 CV = 5.42%	

normally reported in the connection design, it was decided to use the 69.5 ksi as the ultimate weld shear stress in conjunction with the pre-fracture area for capacity calculation.

COMBINATION CONNECTIONS TESTING RESULTS AND CAPACITY PREDICTION

A total of 45 connections were tested to investigate the capacity and load-deformation (i.e., load-slip) behavior of connections utilizing bolts and welds in combination. These tests correspond to Tests 7–15 and Tests 18–23 in Table 1. The combination tests are grouped based on their bolt pattern and faying surface as 2×2 Class A, 2×2 Class B, and 2×3 Class A. Using the known properties of the connecting elements (i.e., bolt pretension, slip coefficient, average effective throat, and weld shear stress), a model can be constructed to predict the connection capacity. Figures 8(a)–(c) show, respectively, the load-deformation behavior of the 2×2 Class A (i.e., Tests 12–14), 2×2 Class B (i.e., Tests 7–9), and the 2×3 Class A (i.e., Tests 18–21) connections.

Combination Connection Capacity Prediction

The predicted capacity of the combination tests is highlighted in Table 5 as the As-Built R_n. This value incorporates the results of the ancillary tests with the current AISC *Specification* model for capacity prediction of combination connections. This capacity is computed as:

$$R_n = R_b + R_w \tag{4}$$

where R_b is the slip resistance of the bolted components and R_w is the weld shear strength. AISC *Specification* Equation J3-4 is adopted for the slip resistance, R_b, calculation; however, the term D_u is omitted because the actual bolt pretension from Table 2 is used. The mean slip coefficient,

µ, is equal to the values highlighted in Table 3 based on the connections bolt pattern and faying surface class. AISC *Specification* Equation J2-3 is adopted for the weld shear strength computation, R_w, where the weld shear stress, F_{nw}, is equal to 69.5 ksi based on the data in Table 4, and the effective fillet weld area, A_{we}, is equal to the average effective throat multiplied by the measured weld lengths for the individual connection.

For determining the connection capacity based on the experimentally obtained load-deformation profiles (i.e., Test R_n reported in Table 5), it was decided to follow the RCSC (2020) curves depicted in Figure 5. Because these connections may fundamentally be slip-critical bolted connections in need of retrofit, it is essential to limit the slip in the connections to prescribed RCSC limitations. The deformation level at which the slip capacity occurs in a slip-critical bolted connection varies widely depending on the faying surface condition. For Class A surface, some bolted-only connection continued to carry force at displacement levels well beyond 0.02-in. However, connections with other Class A surfaces (i.e., 2×3 plates) and Class B surfaces slipped at very low displacement levels, and the ultimate capacity occurred at less than 0.02 in. of slip. Accordingly, it may be difficult to provide a reliable prediction of the force carried by the bolted connection at slip levels higher than 0.02 in.

Accordingly, the ultimate capacity, Test R_n, is taken as the maximum force carried by the connection at or before 0.02 in. of slip. For Class A connections, this capacity represents, on average, 87% of the maximum load carried by the connection based on the load-slip curves. The ultimate capacity of connections with Class B faying surfaces occurs on average at 0.017 in. of slip. For each combination connection test, the strength ratio, ρ, of the AISC prediction model, Test R_n/As-Built R_n, was computed, both for the

	Test	Connection Variables	Average As-Built R_n (kips)	Average Test R_n (kips)	Average Strength Ratio ρ	Group Strength Ratio ρ
				Table 5. AISC As-Built Capacity Prediction		
2×2 Class A	Test 12	A325 ToN ratio: 0.67	235	241	1.02	**AVG = 0.977** **SD = 0.054** **CV = 5.55%**
	Test 13	A325 ToN ratio: 1.00	278	262	0.94	
	Test 14	A325 ToN ratio: 1.50	321	309	0.96	
	Test 15*	A325 ToN ratio: 1.00	439	352	0.80	–
2×2 Class B	Test 7	A325 ToN ratio: 1.50	460	470	1.02	**AVG = 1.07** **SD = 0.106** **CV = 9.94%**
	Test 8	A325 ToN ratio: 0.67	321	348	1.09	
	Test 9	A325 ToN ratio: 1.00	376	391	1.04	
	Test 10	A325 TC ratio: 0.67	289	331	1.15	
	Test 11	A490 ToN ratio: 0.67	355	377	1.06	
2×3 Class A	Test 18	A325 ToN ratio: 0.67	292	266	0.91	**AVG = 0.958** **SD = 0.069** **CV = 7.25%**
	Test 19	A325 ToN ratio: 1.00	335	323	0.97	
	Test 20	A325 ToN ratio: 1.33	394	355	0.90	
	Test 21	A325 ToN ratio: 2.00	518	490	0.95	
	Test 22	A325 TC ratio: 1.00	327	321	0.98	
	Test 23	A490 ToN ratio: 0.50	306	319	1.04	

NOTE: *Test 15 uses 1-in.-diameter bolts and is not included in the 2×2 Class A group statistics.

individual test series and connection group, to evaluate the efficacy of the current model.

2×2 Class A Connections

In the 2×2 Class A connection group, 12 specimens were tested. These correspond to Tests 12–15 shown in Table 1. The 2×2 Class A specimens isolate the weld/bolt strength ratio and aim to understand its effects on the connection behavior. The ratios studied in this test group are 0.67, 1.00, and 1.50 for Tests 12, 13, and 14, respectively. These connections use A325 bolts and are pretensioned with the ToN method. To complement this specimen group, Test 15 includes bolts that are 1 in. in diameter to provide insight into the effect of larger bolts.

Figure 8(a) displays the load-deformation curves for Tests 12–14. The behavior of these connections follows the profile outlined by Case c in Figure 5. Therefore, the experimental capacity, Test R_n, for these connections corresponds to the sustained load at 0.02-in. of slip. Test 15 performed in a similar manner, and the Test R_n was also recorded at this slip level. The Test R_n for these connections is highlighted in Table 5. The overall strength ratio ρ for the connections utilizing ¾ in. bolts, Tests 12–14, was 0.977 with a standard deviation of 0.054 and a coefficient of variation of 5.55%. Meaning, on average, the AISC model slightly overpredicted the capacity of the connection. The AISC model also overpredicted the capacity of the

connections with 1 in. bolts, Test 15, but at a much higher margin. These connections display a strength ratio, ρ, of 0.80 with a standard deviation of 0.082 and a coefficient of variation of 10.2%. It should be noted, however, that none of the connections failed under the AISC *Specification* predicted capacity using nominal material properties.
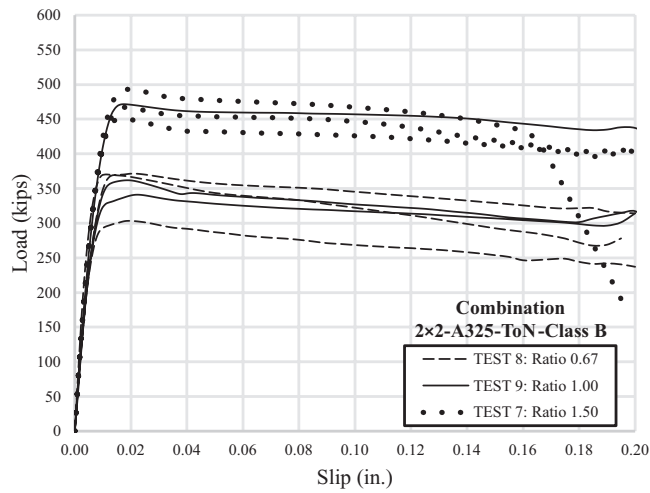
2×2 Class B Connections

A total of 15 specimens were tested in the 2×2 Class B combination connection group. These connections correspond to Tests 7–11. Similar to samples in the 2×2 Class A connection group, Tests 7–9 specifically study the effect of the weld/bolt strength ratio. The connections are constructed with ratios of 0.67, 1.00, and 1.50, respectively, and utilize A325 bolts that are pretensioned with the ToN method. The specimens in Test 10 study the effect of the bolt pretensioning method by using TC bolts. Test 11 includes connections with A490 bolts that are pretensioned with the ToN method to understand the effect of higher bolt grades. Both Tests 10 and 11 are constructed with weld/bolt strength ratios of 0.67.
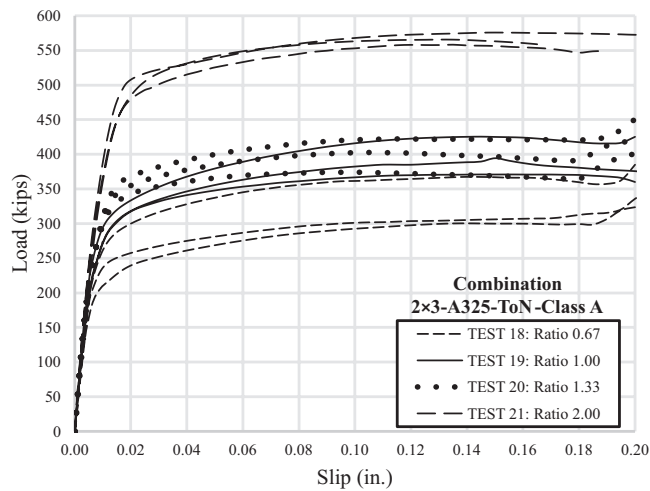
The load-deformation curves for Tests 7–9 are plotted in Figure 8(b). The connections display behaviors similar to that of Case a in Figure 5. Tests 10 and 11 also showed a similar behavior. Therefore, the Test R_n for this connection group is reported in Table 5 as the maximum sustained load before 0.02 in. of slip. The overall strength ratio ρ for
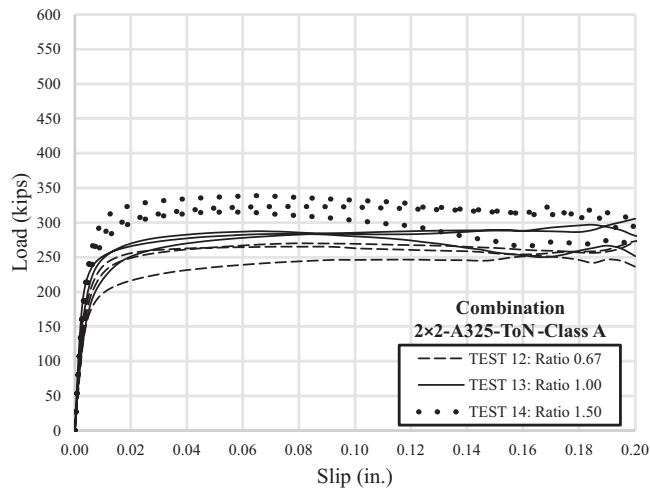
(a) 2×2 Class A

(b) 2×2 Class B

(c) 2×3 Class A

Fig. 8. Combination connection load-slip curves.

this connection group was 1.07 with a standard deviation of 0.106 and a coefficient of variation of 9.94%.

2×3 Class A Connections

The 2×3 Class A connection group is the largest of the combination groups and contains 18 samples. These connections correspond to Tests 18–23 in Table 1. Tests 18–21 vary the weld/bolt strength ratio similar to the other connection groups but include 1.33 and 2.00 ratios. These specimens are constructed with A325 bolts that are pretensioned with the ToN method. The last two test series, Tests 22 and 23, respectively, study the effect of the bolt pretensioning method by using TC bolts, and higher bolt grades with A490 bolts. Test 22 is constructed with a weld/bolt strength ratio of 1.00 and Test 23 with a ratio of 0.50.

The load-deformation curves for Tests 18–21 are depicted in Figure 8(c). Similar to the 2×2 Class A connections, the 2×3 Class A connections show a behavior that closely follows Case c in Figure 5. The Test R_n for these connections is thus considered as the sustained load at 0.02 in. of slip. These values can be found in Table 5. Tests 22 and 23 also followed this behavior, and the same methodology was used to report the Test R_n. The overall strength ratio ρ for the connection group was 0.958 with a standard deviation of 0.069 and a coefficient of variation of 7.25%.

AISC Model Efficacy

Based on the experimental behavior and the analysis of the prediction results of the combination connections, it seems that the current AISC model may overpredict the available strength of certain connection groups. Although the average overprediction is minor (e.g., 4.2% for the 2×3 Class A connections), certain test series even exhibited a 10% overprediction (e.g., Test 20). This overprediction may be attributed to the lack of consideration of strain compatibility within the prediction model. Figure 9(a) further illustrates this observation by analyzing the independent load-deformation curves (bolted only and welded only) that make up the combination connections of Test 14. For this connection, the average of the following experimentally obtained curves are plotted: (A) bolted only, (B) welded only, and (C) combination. The figure also includes a profile that shows the arithmetic summation of curves A and B. As shown, the average experimental behavior of the combination connection given by Curve C can be reasonably approximated by the summation of the individual contributions of the connecting elements (i.e., Curve A + Curve B). This is especially true at lower slip levels. However, for computing the combination connection capacity, the current prediction model adds the friction capacity of bolts, computed at 0.02 in. of slip, to the ultimate weld capacity, which occurs at higher deformation levels; accordingly, strain compatibility may not be properly accounted for.

A similar behavior to that reported in Figure 9(a) was observed for most of the tested connection series. However, for some connections—mostly belonging to the 2×3 Class A group—the summation of the individual element contributions led to an unconservative prediction of the combined connection behavior. An example of these connections is shown in Figure 9(b). As shown, the summation (i.e., Curve A + Curve B) yielded a higher capacity than the average test results (i.e., Curve C). This mainly occurred for Test 18 and 20 and can be attributed to the high variability associated with the friction coefficient of the 2×3 Class A faying surfaces.
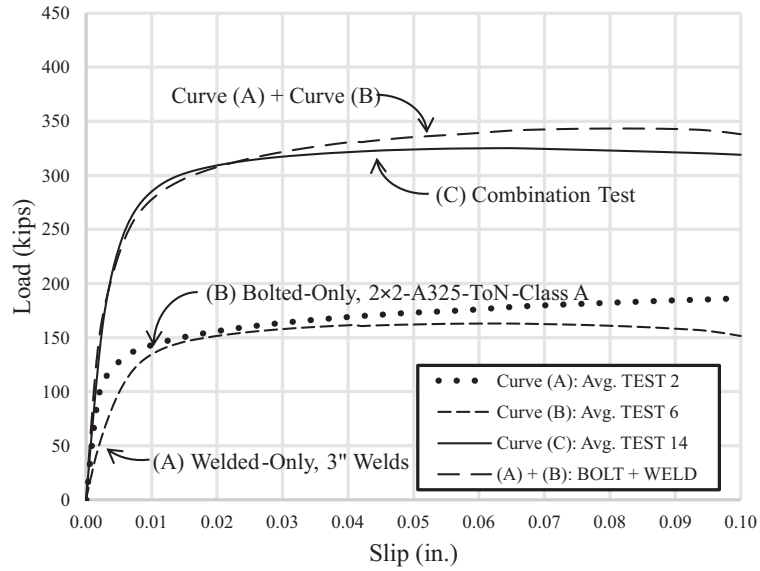
Proposed Capacity Model

A prediction model that accounts for the strain compatibility between the connection elements can be achieved by identifying the weld shear stress at 0.02 in. of slip. This will allow for a better prediction of the combination connection capacity. For the welded-only connections tests, the average weld shear stress associated to this deformation level was found to be 64.0 ksi. Furthermore, the ratio of the weld shear stress at 0.02 in. of deformation over the ultimate weld shear stress was computed to be 0.92 for the 5⁄16 in. welds used in the testing program. A prediction model accounting for this strain compatibility between the bolt slip resistance and the weld shear strength can then be expressed as:

$$R_n = R_b + C_w R_w \qquad (5)$$

where C_w is the ratio of the weld shear stress at 0.02 in. of slip to the ultimate weld shear strength.

Based on the experimental results reported in Table 4, the C_w factor in Equation 5 is equal to 0.92 for the studied combination connection using 5⁄16 in. welds. The efficacy of the proposed capacity prediction model is shown in Figure 10. For all connections plotted, the model provides an average strength ratio ρ of 1.04. For each connection group, the model shows appropriate levels of conservatism with strength ratio ρ of 1.01, 1.11, and 0.998, for 2×2 Class A, 2×2 Class B, and 2×3 Class A connections, respectively. This data is highlighted in Table 6. The coefficient of variation is 5.29%, 9.73%, and 7.01% for the three respective connection groups considered herein.

It is noted that the capacity prediction model presented in Equation 5, specifically with $C_w = 0.92$, only applies to the tested connections given the weld dimensions measured during the experimental analysis. The tested welds were completed in an ideal environment by a highly trained certified welder. Furthermore, research reported by Lesik and Kennedy (1990) suggests that the load-deformation behavior of welded connections can depend on the weld leg size. The load-deformation prediction model in Lesik and Kennedy captures this effect and is adopted in AISC *Manual* Part 8 to compute the capacity of welds using the instantaneous

(a) 2×2 Class A
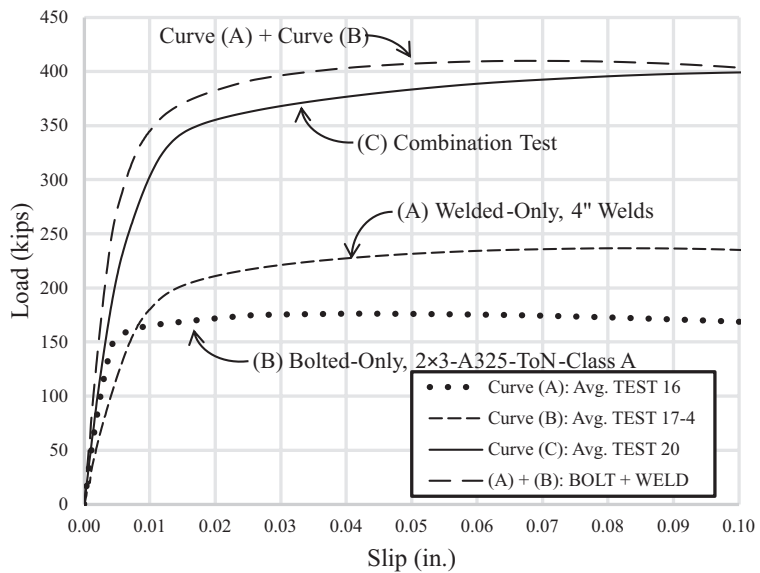
(b) 2×3 Class A

Fig. 9. Combination prediction load-slip curves.

	Test	Connection Variables	Average Model R_n (kips)	Average Test R_n (kips)	Average Strength Ratio ρ	Group Strength Ratio ρ
			Table 6. Proposed Model Capacity Prediction			
2×2 Class A	Test 12	A325 ToN ratio: 0.67	229	241	1.05	**AVG = 1.01** **SD = 0.053** **CV = 5.29%**
	Test 13	A325 ToN ratio: 1.00	268	262	0.98	
	Test 14	A325 ToN ratio: 1.50	308	309	1.01	
	Test 15*	A325 ToN ratio: 1.00	423	352	0.83	—
2×2 Class B	Test 7	A325 ToN ratio: 1.50	438	470	1.07	**AVG = 1.11** **SD = 0.108** **CV = 9.73%**
	Test 8	A325 ToN ratio: 0.67	310	348	1.12	
	Test 9	A325 ToN ratio: 1.00	361	391	1.08	
	Test 10	A325 TC ratio: 0.67	279	331	1.19	
	Test 11	A490 ToN ratio: 0.67	343	377	1.10	
2×3 Class A	Test 18	A325 ToN ratio: 0.67	282	266	0.94	**AVG = 0.998** **SD = 0.070** **CV = 7.01%**
	Test 19	A325 ToN ratio: 1.00	322	323	1.00	
	Test 20	A325 ToN ratio: 1.33	376	355	0.94	
	Test 21	A325 ToN ratio: 2.00	491	490	1.00	
	Test 22	A325 TC ratio: 1.00	313	321	1.02	
	Test 23	A490 ToN ratio: 0.50	297	319	1.07	

NOTE: * Test 15 uses 1-in.-diameter bolts and is not included in the 2×2 Class A group statistics.
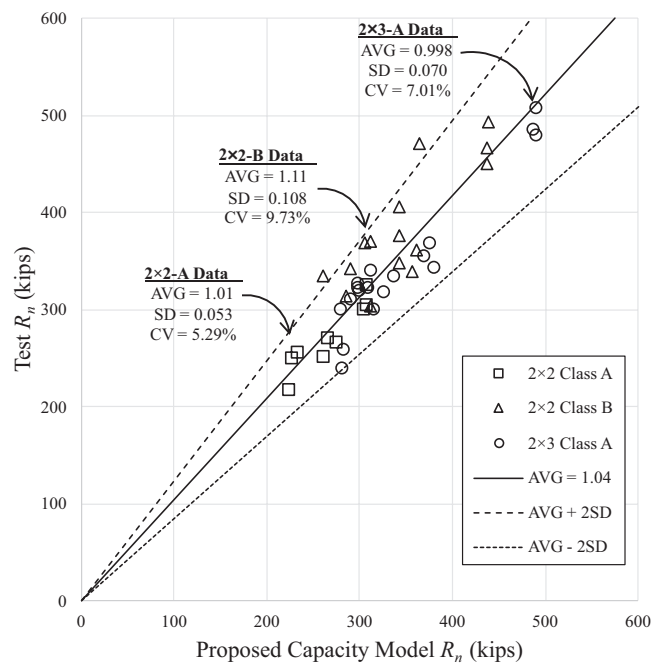

Fig. 10. Proposed capacity model prediction efficacy.

Table 7. C_w Factor (using Equation 8)	
Weld Size (in.)	C_w Factor
⅛	0.995
³⁄₁₆	0.949
¼	0.899
⁵⁄₁₆	0.855
⅜	0.818
⁷⁄₁₆	0.787
½	0.761

center of rotation method. This model can be used to establish a relationship that represents the ratio between the weld strength at 0.02 in. of slip to the ultimate strength as a function of the fillet weld leg size. The deformation of a weld element at the ultimate strength Δ_u is (Lesik and Kennedy, 1990; AISC, 2017):

$$\Delta_u = 0.209(\theta + 2)^{-0.32} w \qquad (6)$$

where θ is the weld orientation and w is the weld leg size. Using AISC *Manual* Equation 8-3, the ratio of the weld strength at a specific deformation, Δ, to the ultimate strength can be computed as:

$$f(\Delta) = \left[\frac{\Delta}{\Delta_u} \left(1.9 - 0.9 \frac{\Delta}{\Delta_u} \right) \right]^{0.3} \qquad (7)$$

By setting Δ equal to 0.02 in., the value of C_w can be found as a function of the weld leg size as:

$$C_w = f(0.02 \text{ in.}) = \left(\frac{0.227w - 0.013}{w^2} \right)^{0.3} \qquad (8)$$

Adopting Equation 8 for the ⁵⁄₁₆ in. weld leg size used in the study would result in a C_w equal to 0.855. This value seems lower than the experimentally obtained value of 0.92; however, with the average measured weld leg size of 0.275 in. in the experimental program, the value of C_w obtained by Equation 8 is 0.880, which is within a 4% difference from the experimental value. Accounting for the effect of weld leg size becomes more important as it increases. For connections with ½ in. welds, the C_w factor is further reduced to 0.761 according to Equation 8. However, limited experimental data exists to validate this result for larger fillet welds. Experimental data on welds mostly report the ultimate capacity rather than the full load-deformation behavior. Accordingly, more experimental work is needed to properly characterize the load-deformation of large fillet welds. Until more data is available, it is recommended to compute a C_w factor using the formulation provided by Equation 8. Table 7 presents the C_w factor for various typical weld leg sizes ranging from ⅛ in. to ½ in.

THE INFLUENCE OF DIFFERENT CONNECTION VARIABLES

The results reported in Figure 8 and Table 6 highlight the ultimate capacity and load-deformation behavior of combination connections. The following discussion provides insight into how critical connection variables influence the connection performance. The variables considered herein are the bolt pattern, bolt size, bolt grade, bolt pretensioning method, faying surface class, and weld/bolt strength ratio.

Bolt Pattern

Two types of connection sizes were included in the test matrix to study the influence of the bolt pattern, 2×2 and 2×3. The results of both configurations can be seen in Figures 8(a) and 8(c). Both connection sets use A325 bolts pretensioned with the ToN method and are constructed with Class A faying surfaces. Although the plates for both groups have the same steel grade, they came from different heats, which affected their surface friction characteristics. As seen in Figures 8(a) and 8(c), the two groups displayed similar load-deformation behaviors. After the elastic region, the 2×2 plates reached their ultimate capacity at an average slip of 0.090 in., whereas the 2×3 plates reached their ultimate capacity at 0.137 in. In comparing the proposed capacity prediction model for both bolt patterns, as reported in Table 6, the group prediction results show similar strength ratios, ρ. As seen from Figures 8(a) and 8(c), at a weld/bolt strength ratio of 0.67, two specimens in Test 12 (2×2) showed similar capacities to those of Test 18 (2×3), even though the connection had two fewer bolts. This is due to the higher slip coefficient of the 2×2 Class A plates versus the 2×3 plates reported in Table 3. Overall, the test data shows that the bolt pattern has a negligible effect on the accuracy of the capacity prediction model for the tested configurations. For these combination connections, load sharing between the frictional resistance of the plates and the longitudinal weld elements was found to occur effectively given the strain compatibility (at low slip levels), between the load-deformation behavior of the

frictional resistance and weld shear forces. For connections with different bolt patterns, if typical AISC *Specifications* detailing practices are followed with respect to maximum/minimum edge distances and bolt spacing, loading sharing between the frictional resistance and the weld shear forces is expected to occur. With reliable load sharing, the connection capacity can be computed using the proposed capacity prediction equation.

Bolt Size

Nearly all connections studied in the research program are constructed with ¾ in. bolts, except Test 15, which utilized 1 in. bolts. Figure 11 compares the load-deformation behaviors of Tests 13 and 15 at the same weld/bolt strength ratio. The load-deformation behavior of the 1 in. bolts follows other 2×2 Class A combination connections depicted in Figure 8(a). Accordingly, the Test R_n for the Test 15 specimens is reported at 0.02 in. of slip in Table 6. The test data shows that the AISC model overpredicts the capacity of connections utilizing 1 in. bolts by roughly 20% and the proposed model, as shown in Table 6, overpredicts the connection capacity by 17%. Both models show the strength ratio, ρ, that is significantly lower than the values obtained for connections made with ¾ in. bolts. This drop in capacity may be attributed to the loss of pretension force arising from the localized yielding that was observed around the bolt holes. Significant deformations around bolt holes were observed in the 1 in. tests, while no similar deformation

occurred with the ¾ in. bolts. Figure 12 shows the deformations around the bolt holes in one of the splice plates of Test 15. Allan and Fisher (1968) reported a 15% drop in the pretension force for 1 in. bolts when oversized holes are used. A similar reduction in the slip capacity of bolted connections when larger bolts are used has been reported in Shoukry and Haisch (1970) and Heistermann et al. (2013). Accordingly, it is believed that the drop in capacity for these connections is primarily attributed to the lower contribution of the bolt slip load.

Bolt Grade

The connections in Tests 23 and 11 are utilized to study the influence that bolt grade has on the combination connection performance. These specimens utilize A490 bolts, while comparative tests—Tests 18 and 11—use A325 bolts. Test 23 is constructed with the same weld length of Test 18, and Test 11 is constructed with the same weld/bolt strength ratio as Test 8. The load-deformation behaviors shown in Figures 13(a) and 13(b) indicate that the bolt grade does not alter the slip behavior but leads to a change in the connection capacity that is comparable to the increase in the pretension force introduced by the higher grade.

Bolt Pretensioning Method

Two connection groups were added to the test program to investigate the effect of the bolt pretensioning method on the capacity: Tests 22 and 10. These connections are
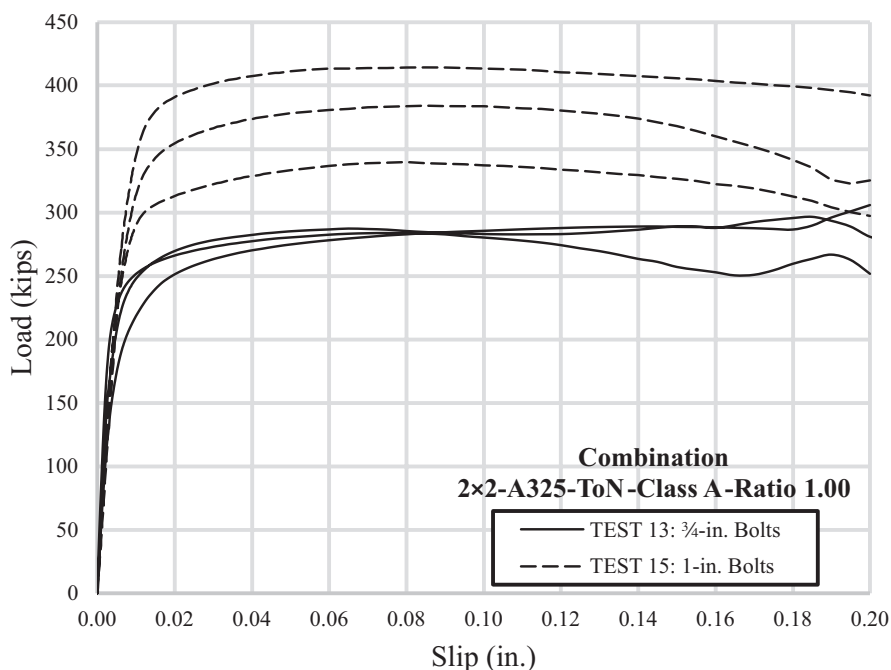

Fig. 11. Bolt size load-slip curve comparison: ¾ in. diameter vs. 1 in. diameter.

constructed with TC bolts while all other connections in the study are pretensioned with the turn-of-nut (ToN) method. The performance of these two connection groups can be analyzed against similar connections pretensioned with the ToN method—Tests 19 and 8, respectively. The load-deformation curves plotted in Figures 14(a) and 14(b) show that the pretensioning method does not alter the general connection behavior. The Class A connections in Test 19 (ToN) show an average slip load of 323 kips, while Test 22 (TC) slipped at an average load of 321 kips, as shown in Table 6. This comparison shows a less than 1% drop in the capacity of the Class A connections using TC bolts. In comparing Tests 8 and 10, a 5% drop in capacity is observed in the TC bolted connection made with Class B plates. This drop in capacity is expected based on the bolt pretension data reported in Table 2, where the ToN method achieved higher pretension than the TC bolts on average. However, it should be noted that the sample size for the TC bolts was significantly smaller than that of the ToN bolts. Furthermore, the TC bolts achieved, on average, a pretension level that is 37% higher than the minimum required pretension force for this bolt style.

Faying Surface Class

The faying surface was found to have a significant influence on the load-deformation behavior of a combination connection. The load-deformation behavior highlighted in Figures 8(a) and 8(c) for Class A connections shows a stiffness in the elastic region that is comparable to Class B

connections. However, as the displacement increases, the connection begins to soften, and a reduction in stiffness occurs. The slip gradually increases until the ultimate load is reached, and the welds start to show fractures at the ends of the weld lines. Further loading leads to additional crack propagation and a gradual drop in the capacity until welds completely fracture or bolt bearing is achieved. Overall, the connections with Class A faying surfaces displayed a highly ductile behavior and were able to sustain loads over large deformations as the bolts slipped into bearing.

The Class B load-deformation behavior depicted in Figure 8(b) is also very stiff in the elastic region of the connection. At approximately 0.017 in. of slip, the connection softens, and the load drops continuously as the deformation increases. These connections rely on the mechanical interlock established between the blast-cleaned surfaces to provide friction resistance. As the interlock between the steel surfaces is disturbed, the friction resistance is diminished. Overall, the addition of weld to a connection with a Class B faying surface significantly increased the ductility of the connection and improved its behavior. Instead of the sudden slip occurring with the Class B bolted-only connections as they reach their slip load, the combination connections were able to sustain loads over a longer slip distance.

Weld/Bolt Strength Ratio

In this test program, weld/bolt ratios ranging from 0.50 to 2.00 were studied across different connection groups. In all tested connections, an increase in the average slip
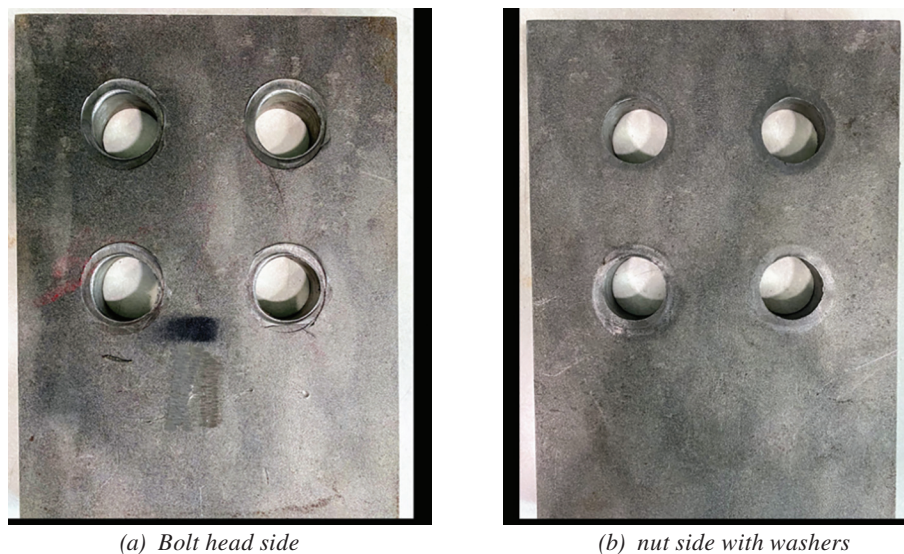

(a) Bolt head side   *(b) nut side with washers*

Fig. 12. Plate dents from 1 in. bolt specimens.

load occurs as the weld/bolt ratio increases. This is to be expected given the additional weld length utilized with higher weld/bolt strength ratios. In examining the strength ratio, ρ, reported for each independent test series in a connection group, it is apparent that the weld/bolt ratio also has a negligible effect on the capacity prediction accuracy. As shown in Table 6, ρ does not display a consistent trend with respect to the weld/bolt ratio. Finally, Figure 8 shows that the weld/bolt ratio also does not influence the general load-deformation behavior the combination connection.

SUMMARY AND CONCLUSIONS

This paper presented the results of an experimental investigation into the load-deformation behavior of double-shear tension splice connections made with pretensioned high-strength bolts and longitudinal fillet welds in combination. The tested connections varied the bolt pattern, bolt size, bolt grade, bolt pretensioning method, faying surface class, and weld/bolt strength ratio. An assessment of the AISC prediction model for a combination connection was made, and a prediction model that maintains strain compatibility
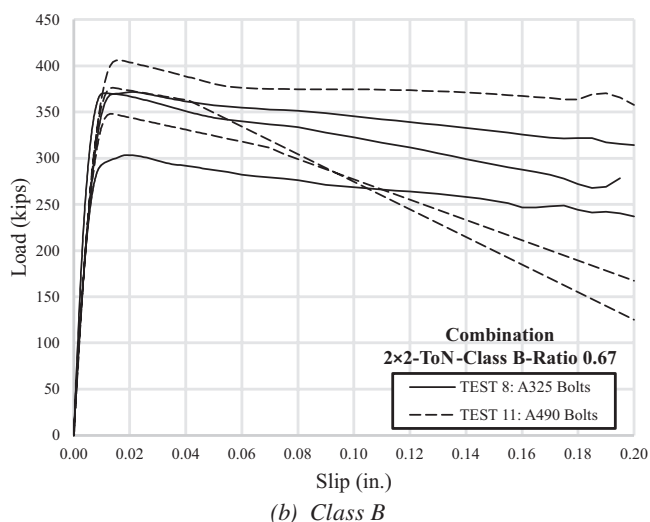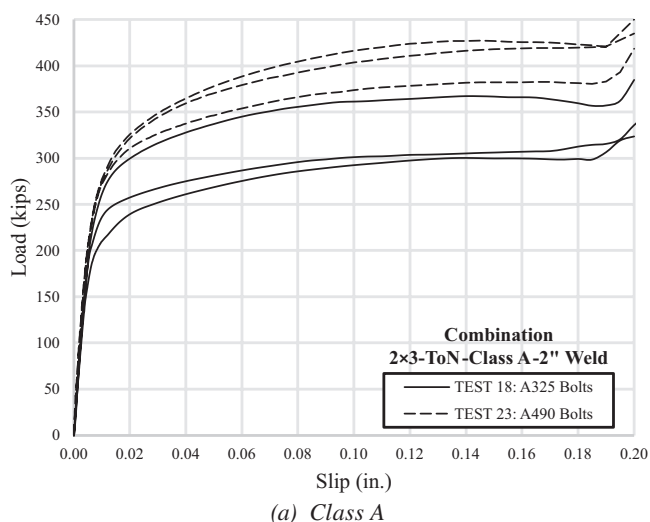

(a) Class A *(b) Class B*

Fig. 13. Bolt grade load-slip curve comparison: A325 vs. A490.
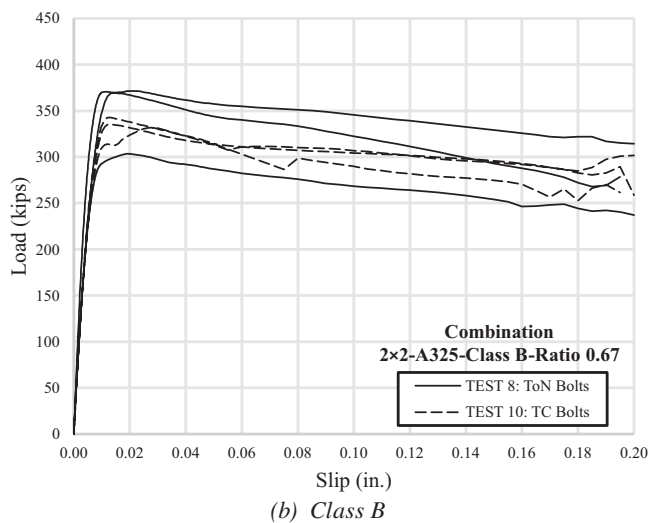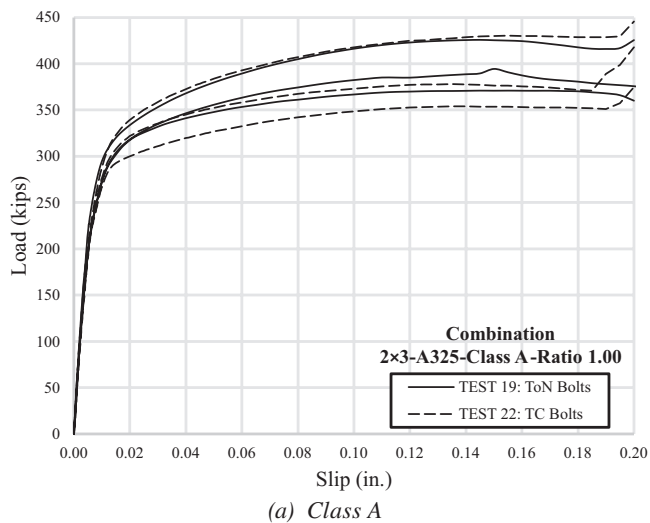

(a) Class A *(b) Class B*

Fig. 14. Bolt tensioning method load-slip curve comparison: ToN vs. TC.

was presented. Based on the observations made during the research program, the following conclusions and recommendations can be made:

1. The addition of longitudinal fillet welds to concentrically loaded slip-critical bolted connections leads to an increase of the connection capacity as well as an improvement in the stiffness of the connection. Connections made with Class B faying surfaces also exhibit an improvement in the ductility when welds are used.

2. Bolted-only connections with Class A (clean mill scale) faying surfaces are ductile and display a hardening behavior. For the tested configurations, combination connections made with these surfaces reach their ultimate capacity at a slip displacement ranging from 0.055 in. to 0.165 in. However, to limit slip of the connection, it is recommended that the connection capacity be limited to the load sustained at 0.02 in. of slip. This load level accounts for 76% to 96% of the capacity.

3. Bolted-only connections with Class B surfaces (SSPC-SP6 commercial blast-cleaning) may slip suddenly before 0.02 in. of deformation. Combination connections with these surfaces reach their ultimate capacity, on average, at approximately 0.017 in. of slip but are more ductile than their bolted-only counterparts. It is recommended that the connection capacity be limited to the maximum sustained load before 0.02 in. of slip.

4. The proposed model, given by Equation 5, which considers strain compatibility of the weld at 0.02 in. of slip, can predict the combination connection capacity with strength ratio value, ρ, of 1.04. This model evaluates the welded component contribution to the combination connection capacity based on the fillet weld load-deformation prediction model provided in AISC *Manual* Part 8. It is recommended that this equation be adopted when determining the ultimate strength of connections utilizing pretensioned high-strength bolts and longitudinal welds in combination.

5. Other connection variables such as the bolt pattern, bolt grade, bolt pretensioning method, and weld/bolt strength ratio show a negligible effect on the general load-deformation behavior of the tested combination connection or accuracy of the prediction model.

6. Future experimental investigations of connections utilizing larger bolts—for example, 1 in. diameter and greater—are recommended to quantify how localized yielding at the bolt holes may affect the bolt pretension, frictional resistance, and ultimate capacity of the connection. These studies may also include connections using ASTM F3125 Grade A490, F1852, and F2280 bolts as well as bolt assemblies using ASTM F959 DTI washers

to understand the sensitivity between the pretensioning method and the localized yielding at the bolt hole for large-bolt diameters.

ACKNOWLEDGMENTS

REFERENCES

AISC (2016), *Specification for Structural Steel Buildings*, ANSI/AISC 360-16, American Institute of Steel Construction, Chicago, Ill.

AISC (2017), *Steel Construction Manual,* 15th Ed., American Institute of Steel Construction, Chicago, Ill.

Allan, R.N. and Fisher, J.W. (1968), "Bolted Joints with Oversize or Slotted Holes," *Journal of the Structural Division*, ASCE, Vol. 94, No. 9, pp. 2061–2080.

ASTM (2021a), *Standard Specification for High Strength Low-Alloy Columbium-Vanadium Structural Steel*, ASTM A572/A572M, ASTM International, West Conshocken, Pa.

ASTM (2021b), *Standard Specification for High Strength Structural Bolts and Assemblies, Steel and Alloy Steel, Heat Treated, In. Dimensions 120 ksi and 150 ksi Minimum Tensile Strength, and Metric Dimensions 830 MPa and 1040 MPa Minimum Tensile Strength*, ASTM F3125, ASTM International, West Conshocken, Pa.

AWS (2016), *Standard Method for Mechanical Testing of Welds*, B4.0:2016, American Welding Society, Miami, Fla.

Borello, D.J., Denavit, M.D., and Hajjar, J.F. (2009), *Behavior of Bolted Steel Slip-Critical Connections with Fillers*, Newmark Structural Engineering Laboratory, University of Illinois at Urbana-Champaign, Champaign, Ill.

Deng, K., Grondin, G.Y., and Driver, R.G. (2003), *Effect of Loading Angle on the Behavior of Fillet Welds,* Structural Engineering Report 251, Department of Civil and Environmental Engineering, University of Alberta, Edmonton, Alta, Canada.

Grondin, G., Jin, M., and Josi, G. (2007), *Slip Critical Bolted Connections—A Reliability Analysis for Design at the Ultimate Limit State*, Structural Engineering Report No. 274, University of Alberta, Edmonton, Alberta, Canada.

Heistermann, C., Veljkovic, M., Simões, R., Rebelo, C., and Da Silva, L.S. (2013), "Design of Slip Resistant Lap Joints with Long Open Slotted Holes," *Journal of Constructional Steel Research*, Vol. 82, pp. 223–233.

Holtz, N.M. and Kulak, G.L. (1970), *High-Strength Bolts and Welds in Load-Sharing Systems,* Structural Engineering Report No. 8, Department of Civil Engineering, Nova Scotia Technical College, Halifax, Nova Scotia.

Jarosch, K.H. and Bowman, M.D. (1986), "Tension Butt Joints with Bolts and Welds," *Engineering Journal*, AISC, Vol. 23, No. 1, pp. 25–34.

Khandel, O., Tamimi, M.F., Soliman, M., Russell B.W., and Waite, C.D. (2022), "Reliability Assessment of Connections with Slip-Critical Bolts and Fillet Welds in Combination," *Journal of Constructional Steel Research*, Vol. 188, 107036.

Kim, D.K. and Lee, C.H. (2020), "Experimental and Analytical Study of Combined Bolted-Welded Lap Joints Including High-Strength Steel," *Journal of Constructional Steel Research*, Vol. 168, 105995.

Kulak, G.L., Fisher, J.W., and Struik, J.H.A. (2001), *Guide to Design Criteria for Bolted and Riveted Joints*, 2nd Ed., American Institute of Steel Construction, Chicago, Ill.

Kulak, G.L. and Grondin, G.Y. (2003), "Strength of Joints that Combine Bolts and Welds," *Engineering Journal*, Vol. 40, pp. 89–98.

Lesik, D.F. and Kennedy, D.L. (1990), "Ultimate Strength of Fillet Welded Connections Loaded in Plane," *Canadian Journal of Civil Engineering,* Vol. 17, pp. 55–67.

Manuel, T.J. (1996), *Strength of Joints That Combine Bolts and Welds*, M.Sc. Thesis, Department of Civil Engineering, University of Alberta, Edmonton, Alberta, Canada.

Manuel, T.J. and Kulak, G.L. (2000), "Strength of Joints That Combine Bolts and Welds," *Journal of Structural Engineering*, Vol. 126, pp. 279–287.

Miller, D.K. (2001), "Mixing Welds and Bolts, Part 1," *Welding Innovation*, Vol. 18, No. 2.

Miller, D.K. (2002), "Mixing Welds and Bolts, Part 2," *Welding Innovation*, Vol. 19, No. 2.

NI (2018), *LabVIEW NXG 3.0 User Manual*, National Instruments, Austin, Tex., https://www.ni.com/documentation/en/labview/3.0/manual/manual-overview/, accessed December 10, 2018.

RCSC (2020), *Specification for Structural Joints Using High-Strength Bolts*, Research Council on Structural Connections, AISC, Chicago, Ill.

Salmon, C.G., Johnson, J.E., and Malhas, F.A. (2009), *Steel Structures: Design and Behavior: Emphasizing Load and Resistance Factor Design*, Pearson Education, Upper Saddle River, N.J.

Sato, T.L. (2000), *Strength of Joints That Combine High Strength Bolts and Longitudinal Welds*, M.Eng. Report, Department of Civil and Environmental Engineering, University of Alberta, Edmonton, Alberta, Canada.

Shi, Y., Wang, L., Wang, Y., Ma, J., and Bai, R. (2011a), "Finite Element Analysis of the Combined Connection with Bolts and Welds," *Applied Mechanics and Materials*, Vol. 94–96, pp. 316–321.

Shi, Y., Wang, L., Wang, Y., Ma, J., and Bai, R. (2011b), "Proposed Design Method of Combined Connections with Bolts and Longitudinal Welds," *Applied Mechanics and Materials*, Vol. 94–96, pp. 923–928.

Shoukry, Z. and Haisch, W.T. (1970), "Bolted Connections with Varied Hole Diameters," *Journal of the Structural Division*, Vol. 96, No. 6, pp. 1,105–1,118.

Steinhardt, O., Möhler, K., and Valtinat, G. (1969), *Experiments on the Use of Pretressed Screws in Steel Construction, Part IV*, Reports of the German Committee for Steel Construction, 25.

Wind Design of Composite Plate Shear Walls/Concrete Filled (SpeedCore) Systems

Soheil Shafaei, Amit H. Varma, Jungil Seo, Devin Huber, and Ron Klemencic

ABSTRACT

Composite steel plate shear walls/concrete filled (C-PSW/CF), also known as the SpeedCore system, are a composite solution for the design of mid- to high-rise buildings. A C-PSW/CF system consists of steel plates (web and flange plates) and an infill concrete core. The composite interaction between steel plates and concrete core is developed by either tie bars or tie bars and shear studs. Generally, in low- to mid-rise buildings (less than 15 stories), planar (uncoupled) C-PSW/CFs are adequate for resisting lateral loading and deformations. Coupled C-PSW/CFs become more prevalent in mid- to high-rise buildings when increased lateral stiffness is desirable. The steel parts of SpeedCore system (steel plates, tie bars, and shear studs) are prefabricated in the shop and then transported to the site for assembly and erection. The erected empty steel module serves as falsework and formwork during construction and concrete casting, which reduces construction schedule considerably. This is a major advantage of SpeedCore systems, especially when compared with conventional reinforced concrete core systems. This paper presents the wind (nonseismic) design requirements and procedures for planar uncoupled and coupled C-PSW/CF systems. It includes a design example of a 15-story building located in Chicago, Illinois, using both uncoupled and coupled systems.

Keywords: composite plate shear walls/concrete-filled; SpeedCore system; uncoupled C-PSW/CF; coupled C-PSW/CF; wind design; nonseismic design, cyclic behavior of C-PSW/CF.

INTRODUCTION

The selection and proper specification of a lateral force-resisting system (LFRS) is one of the most critical design decisions for mid- to high-rise buildings. One popular lateral system used in both steel and reinforced concrete construction is a coupled reinforced concrete (RC) core wall system. As the overall structural height increases, the required lateral stiffness increases. For "signature" tall buildings—for example, 432 Park and Stenway Tower in New York City—the RC concrete wall thickness and reinforcement ratio can become very high (greater than 2%), leading to rebar congestion, concrete placement issues, and potential schedule delays. Composite plate shear walls/concrete filled (C-PSW/CF), also known as the SpeedCore system, offer a steel-concrete composite solution to such concrete core walls. Planar (uncoupled) or coupled C-PSW/CF systems offer several advantages compared to traditional RC core walls in mid- to high-rise buildings, including:

1. Steel modules are prefabricated in the shop and assembled together once at site, which reduces the construction schedule associated with assembling rebar cages.

2. Empty steel modules of C-PSW/CF, including steel web and flange plates, tie bars, and shear studs, serve as falsework and formwork during the construction and concrete casting.

3. Steel web and flange plates serve as permanent formwork and steel reinforcement of the composite wall after concrete sets, which further helps reduce the construction schedule by eliminating an additional step for form removal.

4. Rebar congestion issues are reduced by eliminating rebar cages.

5. Easier concrete placement is allowed by using conventional or self-consolidating concrete (SCC).

6. Core walls can be constructed at the same pace as steel framing. Unlike RC construction, there is no need to construct the core much further ahead of the steel framing. This reduces the number of trades that need to be coordinated at the site and also reduces construction tolerance issues with embed plates connecting the steel framing to the core.

Soheil Shafaei, PhD, Post-Doctoral Research Associate, Purdue University, Lyles School of Civil Engineering, West Lafayette, Ind. Email: sshafaei@purdue.edu (corresponding)

Amit H. Varma, PhD, Karl H. Kettelhut Professor, Purdue University, Lyles School of Civil Engineering, West Lafayette, Ind. Email: ahvarma@purdue.edu

Jungil Seo, PhD, Research Assistant Professor, Purdue University, Lyles School of Civil Engineering, West Lafayette, Ind. Email: seo2@purdue.edu

Devin Huber, PE, PhD, Director of Research, American Institute of Steel Construction, Chicago, Ill. Email: huber@aisc.org

Ron Klemencic, PE, SE, Hon. AIA, F. SEI., Dist. M. ASCE, NAE, Chairman and CEO, Magnusson Klemencic and Associates, Seattle, Wash. Email: rklemencic@mka.com

7. Higher reinforcement ratios (if needed) are achieved by using steel plates.

C-PSW/CF systems can have some challenges as well. For example:

1. The minimum steel plate thickness must be limited to ⅜ in. due to practical considerations of handling, fabrication, and transportation.

2. The steel fabrication costs may be larger than those in RC construction.

3. In-situ welding requirements may be a limitation in some locations due to costs or safety.

4. Design criteria and guidance are not yet available to the profession.

This paper provides an introduction as well as clarity on the nonseismic design of uncoupled (planar) and coupled C-PSW/CF systems when subjected to wind loading. Similar guidance for uncoupled C-PSW/CF systems subjected to seismic loading is available in AISC *Seismic Provisions* (2016a) Section H7 and Agarwal et al. (2020). Seismic design requirements and procedure for coupled systems are also provided in the FEMA P-2082 (FEMA, 2020) provisions and through expected changes in the 2022 edition of the AISC *Seismic Provisions* (AISC, 2022a) and the 2022 edition of ASCE 7 (ASCE, 2016; Bruneau et al., 2019; Broberg et al., 2022). Similarly, revisions to the 2022 edition of the AISC *Specification* (AISC, 2022b) will aim to address wind design of C-PSW/CF systems. However, no other literature is currently readily available for the wind design of uncoupled and coupled C-PSW/CF systems, and this paper serves to provide the interim guidance for this subject.

BACKGROUND

Composite plate shear walls/concrete filled (C-PSW/CF) consist of steel modules that are filled with plain concrete. Figure 1 shows a typical representation of a planar (uncoupled) C-PSW/CF panel. The modules consist of two exterior steel web plates that are connected to one another using tie bars, threaded rods, or other steel shapes, and there are steel flange plates (closure plates) at the end. The composite interaction between the steel plates and infill concrete is developed by tie bars or by a combination of tie bars and shear studs. Note that shear studs are not a specific requirement of the system, but they can be used to reduce the total number of ties in a C-PSW/CF.

The empty steel modules of C-PSW/CF consisting of steel plates (webs and flanges), tie bars, and shear studs are prefabricated in the shop and then shipped to the site for final assembly and concrete casting. The modules get shipped to the site "empty" (no concrete fill), are assembled and connected together to other panels into a final configuration, and then concrete is placed into the panels. The empty modules are stacked to a certain height, typically two to three stories, for each placement of concrete, and the process is repeated as the structure is constructed. A photo of an assembled empty module with coupling beams being placed at a site is shown in Figure 2. Generally, the empty steel modules come without painting, but after assembly, they might be fireproofed or painted, if needed (Anvari et al. 2020).

The steel plates act compos;ely with the hardened concrete using different configurations of tie bars, tie bars and shear studs, or other types of anchorage (i.e., steel shapes). These regularly spaced steel anchors and tie bars restrain local buckling of the steel faceplates, provide
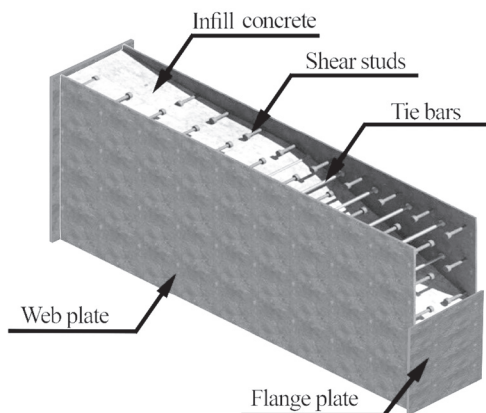

Fig. 1. Typical details of planar (uncoupled) C-PSW/CF (Shafaei et al., 2021a).

horizontal shear resistance, and develop composite action between the steel plates and the concrete infill (Zhang et al., 2014). Additionally, the tie bars (1) provide out-of-plane shear resistance, (2) provide confinement for concrete, and (3) resist potential delamination failure mode through the plain concrete (Sener and Varma, 2014).

C-PSW/CF systems do not include any conventional reinforcing steel of the plain concrete infill. The steel plates serve as the primary reinforcement for resisting all in-plane forces and moments as well as out-of-plane flexure. Out-of-plane shear resistance is provided by the concrete infill and the tie bars (Sener and Varma, 2014) and interfacial shear resistance by the steel anchors and tie bars (Zhang et al., 2014; Sener et al., 2016).

The lateral load behavior of planar C-PSW/CF systems, including their lateral force-deflection behavior and ductility, has been experimentally and numerically evaluated by Shafaei et al. (2021a, 2021b). Research on the lateral load behavior of coupled C-PSW/CF core wall structures is limited with studies ongoing by the authors. The behavior of C-PSW/CF subjected to cyclic lateral loading was investigated by Ramesh (2013). The study focused on (1) the stability of the C-PSW/CF module for construction loads and (2) the cyclic performance of welded details and other structural elements. The specimens were subjected to limited inelastic deformations prior to failure of welded details. The findings were limited to specific wall and faceplate thicknesses, tie bar ratio and spacing, and T-shaped intersections. Additional research is needed and is ongoing to investigate the behavior of planar and coupled C-PSW/CF as explained in the following section.

COMPOSITE PLATE SHEAR WALLS/CONCRETE FILLED (C-PSW/CF)

In mid- to high-rise buildings, planar (uncoupled) or coupled C-PSW/CF systems can be selected based on the architectural plan to resists the lateral loads. Figure 3 shows several examples of typical planar and coupled C-PSW/CF core wall structures.

As shown in Figure 3, coupled systems consist of two (or more) individual C-PSW/CF connected together by coupling beams (link beams) along the height of the structure. Individual C-PSW/CF with planar, C, U, I, or T shapes are utilized to make coupled CPSW/CF core wall systems.

In higher seismic areas, the use of composite coupling beams is more common due to the large forces to be transferred and to meet ductility requirements for performing a capacity-based design. However, coupling beams using all-steel rolled shapes or built-up shapes can be more readily utilized in nonseismic areas where they can be sized to resist only the applied lateral loading, as discussed in subsequent sections.

At the time of publication, research by the authors is ongoing to investigate behavior of coupling beams in both seismic and nonseismic (i.e., wind-governed) regions. Configurations being investigated for the coupling beam research include standard wide-flange structural shapes, steel-only built-up sections, and composite steel-concrete built-up box shaped beams.

There are no specific ductility requirements or performance criteria for connections in nonseismic design (wind-governed design) of C-PSW/CF systems. Different types of

Fig. 2. Assembled coupled C-PSW/CF module being lifted into place at Rainier Square Project in Seattle, Washington (photo courtesy of Keith Evans/ENR).
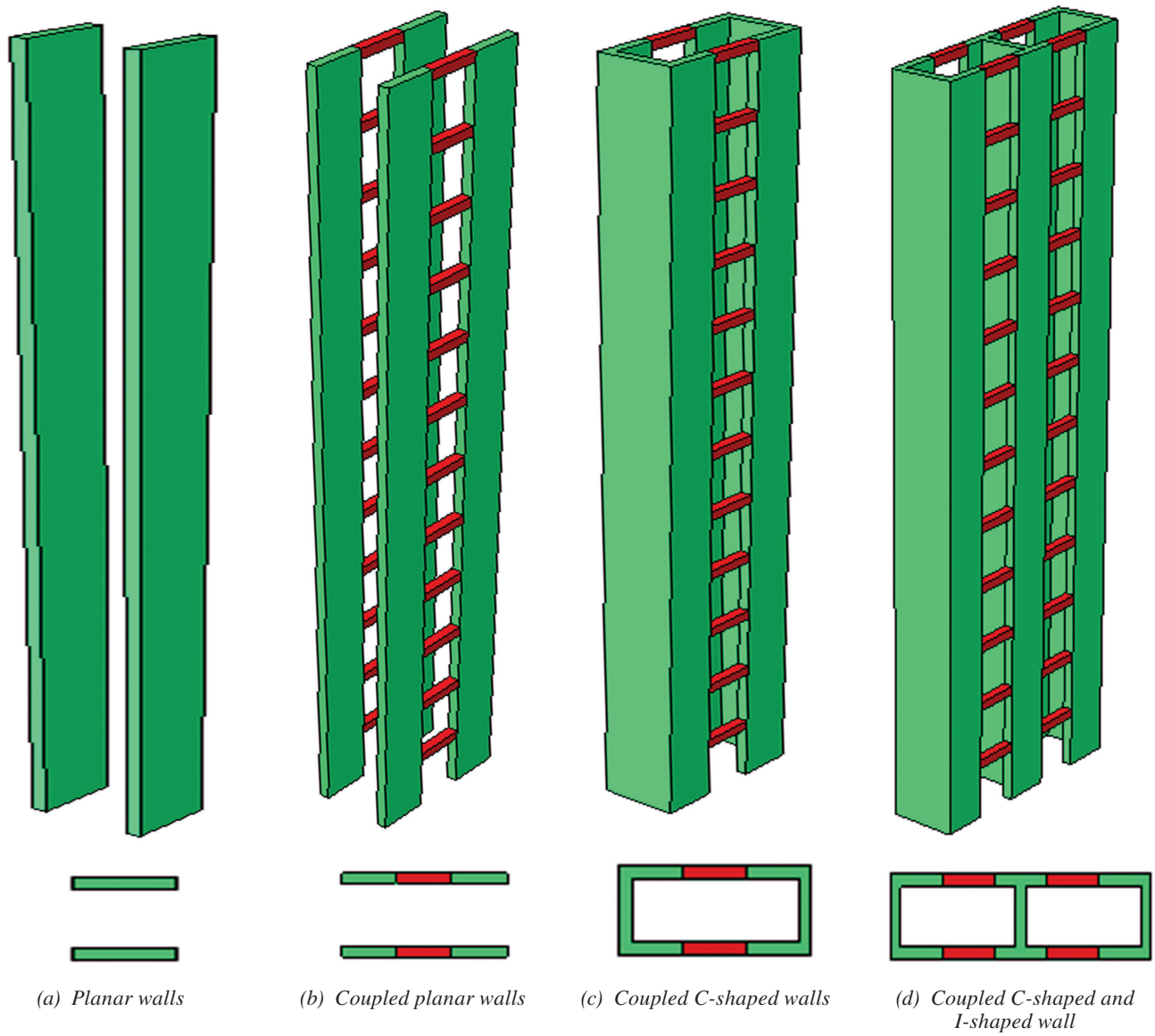
(a) Planar walls   *(b) Coupled planar walls*   *(c) Coupled C-shaped walls*   *(d) Coupled C-shaped and I-shaped wall*

Fig. 3. Variations of composite plate shear walls/concrete-filled.

welded or bolted connections at the section, member, and structure levels can be designed according to the AISC *Specification* (2016b) Chapter J requirements. Tie bar-to-steel plate, flange-to-web plate, and wall segment connection are examples of connections at the section levels. Connections at the member level can be coupling beam-to-wall and wall splice connections, and connections at the structure level can be wall-to-foundation and floor-to-wall connections. In wind design of C-PSW/CF systems, the connections at the member or structure levels can be designed based on the required strength using AISC *Specification* Chapter J provisions.

LATERAL LOAD BEHAVIOR OF C-PSW/CF SYSTEMS

Figure 4 illustrates idealized responses of planar and coupled shear wall systems under wind lateral loading. The lateral load behavior of planar C-PSW/CF is totally different from coupled C-PSW/CF and is described herein.

Planar C-PSW/CF Response

Planar C-PSW/CF structures are being considered in seismic and wind design of low- to mid-rise building (less than 15 stories) considering the architectural design. When a planar C-PSW/CF system is used, the planar wall resists the lateral load like a cantilever beam, as shown in Figure 4(a). The lateral load response of a planar C-PSW/CF system is governed by in-plane flexural behavior.

Coupled C-PSW/CF Response

In seismic and wind design of mid- to high-rise buildings utilizing C-PSW/CF systems, coupled configurations are typically used. Figure 4(b) illustrates an idealized coupled shear wall system deformed under wind lateral loads, which cause a global system overturning moment (OTM) at the base. The coupled wall system resists the OTM by flexural moment resistances in the individual walls, M_1 and M_2, as well as by developing an axial force couple [$\Sigma V_{beam,j}$ at the lever arm, L, as shown in Figure 4(b)]. The contribution of the axial force couple, $\Sigma V_{beam,j}$, to resisting the OTM is defined as the coupling ratio (*CR*) and it can be calculated using Equation 1. A *CR* of 0% implies that no coupling beams are present or the two individual shear walls are disconnected. A *CR* of 100% is the theoretical case where the coupling beam length is zero.

$$CR = \frac{L\sum V_{beam,j}}{L\sum V_{beam,j} + M_1 + M_2} = \frac{L\sum V_{beam,j}}{OTM} \tag{1}$$

The axial force couple, $\Sigma V_{beam,j}$, is applied to the individual shear wall (in addition to gravity loads). The axial force, either compression, P, or tension, T, acting on the individual shear wall influences the behavior of the wall (El-Tawil et al., 2010). For example, the axial compression force acting on the individual shear wall reduces the ductility of the wall due to concrete crushing failure, and the axial tension force acting on the individual shear wall decreases the flexural stiffness and strength of the wall. Hence, in design of coupled systems, each individual wall (tension or compression wall) should be designed separately.
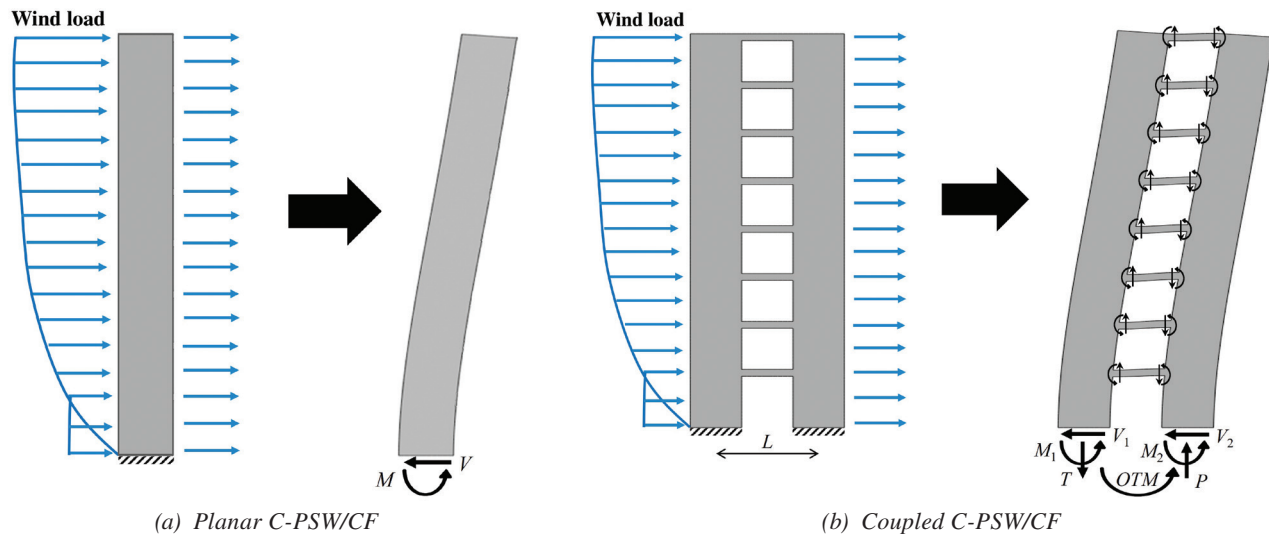

(a) Planar C-PSW/CF

(b) Coupled C-PSW/CF

Fig. 4. Idealized shear wall systems deformed under wind loading.

The ratio of the coupling action is directly correlated with the flexural stiffness of coupling beams and C-PSW/CF. Hence, higher coupling beam flexural stiffness will result in higher coupling action and *CR*. Often, the coupling beam consists of concrete-filled built-up box sections or rectangular HSS since they have similar characteristics in cross section with a C-PSW/CF. However, steel coupling beams can be used for nonseismic applications (wind design).

DESIGN REQUIREMENTS FOR PLANAR AND COUPLED C-PSW/CF SYSTEMS

When this paper was in development, specific and prescribed design requirements for seismic composite plate shear walls existed in various literature, and these references are noted whenever possible. With respect to seismic design requirements, provisions for uncoupled C-PSW/CF currently exist in AISC *Seismic Provisions* (2016a) Section H7. An additional section, Section H8, is currently under development for coupled systems and is expected to be in the 2022 edition of AISC *Seismic Provisions*. Also currently under development are updates to the 2022 edition of the AISC *Specification* that would apply to building design not governed by seismic loads.

Presented in the following sections are design requirements for uncoupled and coupled C-PSW/CF systems to aid engineers in sizing various wall components. It is noted herein where these requirements exist in current provisions in the AISC *Seismic Provisions* or AISC *Specification*. Other recommendations provided, but not within the current specifications, are also noted. Many of these recommendations will become specific requirements in the 2022 editions of the AISC specifications, but they are still under review. Note, there are certain requirements with respect to both seismic and wind design that are the same regardless of what region the structure is located within. Similarly, between planar and coupled C-PSW/CF systems, some design requirements stay constant.

DESIGN REQUIREMENTS FOR C-PSW/CF

The following sections present requirements proposed in the 2022 AISC *Specification* for nonseismic design of C-PSW/CF.

Section Detailing of C-PSW/CFs

As proposed in the AISC *Specification*, the opposing steel web plates of C-PSW/CF have equal nominal thicknesses and are connected to each other using ties consisting of bars, structural shapes, or built-up members. For filled composite plate shear walls, the steel plates are anchored to the concrete using tie bars or a combination of tie bars and steel anchors (steel headed studs). The minimum steel reinforcement ratio of C-PSW/CF is 1%, and the maximum is 10% of the wall gross cross section. C-PSW/CF have steel flange plates (closure plates) or boundary elements at the end of the wall cross-section.

Slenderness Requirement

As proposed for the AISC *Specification*, the slenderness ratio of the steel plates is defined as b/t_p, where b is the largest spacing between rows of tie bars or stud anchors (if included). This slenderness ratio has a significant influence on the local buckling and compressive strength of the steel plate. Zhang et al. (2014, 2020) have experimentally and numerically evaluated the effects of steel plate slenderness ratio on the local buckling and axial compressive strength of composite walls. They established the local buckling classification criterion, shown here as Equation 2. When the plate slenderness ratio satisfies the inequality of Equation 2, then it can develop the nominal yield stress, F_y, before local buckling. It is important to note that the critical buckling stress of slender plates can be estimated using equations provided by Zhang et al. (2020), which are not included here.

$$\frac{b}{t_p} \leq 1.2\sqrt{\frac{E}{F_y}} \tag{2}$$

where
E_s = elastic modulus of steel plate, ksi
F_y = yield stress of steel plate, ksi
b = largest clear distance between rows of tie bars or stud anchors, in.
t_p = steel plate thickness, in.

Tie Bar Requirement

As proposed for the AISC *Specification*, C-PSW/CF need to maintain the structural integrity and prevent concrete splitting of the wall section. For nonseismic applications, there is no minimum tie bar strength requirement, as the tie bar requirement of the empty module governs the design. The empty steel module requirements apply to the steel shell prior to concrete casting. These requirements relate to the required effective shear stiffness, GA_{eff}, of the empty module, which governs the structural behavior and stability during construction and concrete casting (Varma et al. 2019). This limit also ensures that concrete casting pressure and other construction loads do not excessively deform the steel modules prior to concrete curing. This limit is presented in Equations 3 and 4.

$$\frac{s}{t_p} \leq 1.0\sqrt{\frac{E_s}{2\alpha+1}} \tag{3}$$

$$\alpha = 1.7\left(\frac{t_{sc}}{t_p} - 2\right)\left(\frac{t_p}{d_{tie}}\right)^4 \qquad (4)$$

where

d_{tie} = effective diameter of the tie bar, in.

s = largest clear spacing of ties, in. (vertical)

t_p = steel plate thickness, in.

t_{sc} = thickness of composite plate shear wall, in.

Stiffness of C-PSW/CF

As proposed for the AISC *Specification*, the flexural, axial, and shear stiffnesses of composite plate shear walls account for the extent of concrete cracking corresponding to the required strength. The effective flexural, axial, and shear stiffnesses are calculated using Equations 5, 6, and 7, respectively.

$$EI_{eff} = E_s I_s + 0.35 E_c I_c \qquad (5)$$

$$EA_{eff} = E_s A_s + 0.45 E_c A_c \qquad (6)$$

$$GA_{v.eff} = G_s A_{sw} + G_c A_c \qquad (7)$$

where

A_c = area of concrete, in.^{2}

A_s = area of steel section, in.^{2}

A_{sw} = area of steel plates in the direction of in-plane shear, in.^{2}

E_c = modulus of elasticity of concrete
= $w_c^{1.5}\sqrt{f_c'}$, ksi

E_s = modulus of elasticity of steel
= 29,000 ksi

G_c = shear modulus of concrete
= $0.4 E_c$

G_s = shear modulus of steel
= 11,200 ksi

I_c = moment of inertia of the concrete section about the elastic neutral axis of the composite section, in.^{4}

I_s = moment of inertia of steel shape about the elastic neutral axis of the composite section, in.^{4}

w_c = weight of concrete per unit volume ($90 \le w_c \le 155$ lb/ft^3)

Strength of C-PSW/CF

As proposed for the AISC *Specification*, the nominal flexural strength, $M_{n,wall}$, of planar C-PSW/CF can be calculated using the plastic stress distribution method or using a cross-section fiber-based analysis. A strength reduction factor, ϕ_b, of 0.90 is considered in the calculation of the design flexural strength, $\phi M_{n,wall}$, of C-SPW/CF. In the calculation

of the nominal flexural strength using the plastic stress distribution method, it is assumed the steel plates reach the yield stress, F_y, in both tension and compression and the infill concrete core develops compression stress equal to $0.85 f_c'$.

Alternatively, the nominal flexural strength, $M_{n,wall}$, can be computed using fiber cross-section analysis. In fiber analysis, the influence of the axial force, P, from gravity load and induced by the coupling action on the wall flexural strength should considered. Hence, the flexural strength of individual wall subjected to either axial tension or compression force is directly calculated using a fiber analysis.

As proposed for the AISC *Specification*, the nominal in-plane shear strength of C-PSW/CF, $V_{n,wall}$, is computed using Equation 8. In the equation, F_y is the nominal yield stress of the steel wall plate, and A_{sw} is the steel web plate area. A strength reduction factor, ϕ, of 0.90 is used to calculate the design shear strength, $\phi V_{n,wall}$, of C-PSW/CF.

$$V_{n,wall} = \frac{K_s + K_{sc}}{\sqrt{3K_s^2 + K_{sc}^2}} A_{sw} F_y \qquad (8)$$

where

$$K_s = G_s A_{sw} \qquad (9)$$

$$K_{sc} = \frac{0.7(E_c A_c)(E_s A_{sw})}{4 E_s A_{sw} + E_c A_c} \qquad (10)$$

The recomendations given herein for the axial load strength of CPSW/CF systems are based on the following requirements being met:

1. The steel plates comprise at least 1% of the total composite cross-sectional area.

2. The steel plates satisfy the slenderness requirements noted previously.

As proposed for the AISC *Specification*, the nominal compressive strength of axially loaded composite plate shear walls is determined for the limit state of flexural buckling. The value of flexural stiffness, EI_{eff}, from Equation 5 is used along with the section axial compressive strength, P_{no}, calculated using Equation 11. The unsupported length for flexural buckling of composite walls is typically assumed to be equal to the story height.

$$P_{no} = F_y A_s + 0.85 f_c' A_c \qquad (11)$$

As proposed for the AISC *Specification*, the design tensile strength of axially loaded C-PSW/CF is determined by the limit state of steel plate yielding in accordance with Equation 12.

$$P_n = A_s F_y \qquad (12)$$

DESIGN REQUIREMENTS FOR COUPLING BEAMS

For nonseismic applications, composite steel-concrete or steel beams (wide flange steel beams or built-up sections) can be used for the coupling beams of coupled C-PSW/CF systems. Composite coupling beams can be concrete-filled built-up box sections or rectangular HSS sections. For seismic design, the coupling beams are proportioned to be flexure critical (flexural governing behavior); however, for wind design, the coupling beams are designed to resist the demand forces and moments. The requirements for composite coupling beams are based on those in the AISC *Specification* Chapter I as identified in the following subsections.

Section Detailing of Filled Composite Coupling Beams

As required by AISC *Specification* Section I2.2a, the cross-sectional area of the steel section should comprise at least 1% of the total composite cross section. This minimum area of steel requirement is based on AISC *Specification* Section I2 requirements for composite members.

Slenderness Requirement

As proposed for the AISC *Specification*, in composite coupling beams, width-to-thickness of steel plate limits are critical since the structural performance of coupled C-PSW/CF system is directly related to the behavior of the coupling beams. Per AISC *Specification* Section I1.4 (Table I1.1b), the width-to-thickness limits are used to classify the coupling beams as compact, noncompact, or slender for flexure. For wind (nonseismic) design, there is no requirement to select exclusively a compact section as compared to seismic design.

Stiffness of Filled Composite Coupling Beams

As required by AISC *Specification* Section I2.2b, the effective flexural stiffness, EI_{eff}, of the filled composite coupling beams is calculated using Equation 13. The term C_3 in Equation 13 is the coefficient to calculate the effective rigidity of a filled composite member in compression, and it is calculated using Equation 14. For the axial stiffness, EA, the gross area of the coupling beam is used. If the structural analysis is based on the direct analysis method, flexural and axial stiffness values of the composite concrete-filled coupling beams are reduced to $0.64EI_{eff}$ and $0.8EA$.

$$EI_{eff.CB} = E_s I_s + E_s I_{sr} + C_3 E_c I_c \tag{13}$$

$$C_3 = 0.45 + 3\left(\frac{A_s + A_{sr}}{A_g}\right) \leq 0.9 \tag{14}$$

Strength of Filled Composite Coupling Beams

As required by the AISC *Specification* Section I3.4b, the nominal flexural strength of composite coupling beams, $M_{n,CB}$, is determined according to AISC *Specification* Section I3.4b using the plastic stress distribution method. A strength reduction factor, ϕ, of 0.90 is considered in the calculation of the design flexural strength of composite coupling beams, $\phi M_{n,CB}$.

As proposed for the AISC *Specification*, the nominal shear strength of composite coupling beams, $V_{n,CB}$, is calculated as the design shear strength of the steel section and the concrete infill according to Equation 15, where A_v is the area of steel webs and A_c is the cross-sectional area of the concrete. A strength reduction factor, ϕ, equal to 0.90 is considered in the calculation of the design shear strength of concrete-filled coupling beams, $\phi V_{n,CB}$.

$$V_{n.CB} = 0.6A_v F_y + 0.06K_c A_c \sqrt{f'_c} \tag{15}$$

Requirements for Steel Coupling Beams

The use of steel coupling beams is permitted in wind (nonseismic) applications of C-PSW/CF systems. The design of steel coupling beams for flexure and shear is conducted in accordance with AISC *Specification* Chapter F (Design of Members for Flexure), Chapter G (Design of Members for Shear), and Chapter J (Design of Connections), respectively.

CONNECTION REQUIREMENTS

The behavior and design of SpeedCore systems for nonseismic, or wind-governed, loading combinations have no explicit ductility or performance requirements for the connections beyond those of adequate strength for the design demands (required strengths) calculated from the analysis for the applicable factored load combinations. Welded and/or bolted connections are designed in accordance with the requirements of AISC *Specification* Chapter J.

Connections of the tie bars to the steel plate are designed to develop the yield strength of the tie bar in axial tension. This enables yielding of the tie bars before failure of the tie-to-plate connection.

Connections at the member and structure levels are designed in accordance with the calculated design demands (required strengths) at the corresponding levels and location. Some examples of the different types of connections in the systems include (1) coupling beam-to-composite wall connections, (2) composite wall-to-foundation or subgrade structure connections, and (3) splice connections in composite walls.

PRACTICAL AND CONSTRUCTION CONSIDERATIONS OF C-PSW/CF SYSTEMS

In many cases, the plate thicknesses for planar or coupled C-PSW/CF modules govern the design based on construction considerations related to welding requirements or the stability of the empty steel modules during the construction and concrete casting. Previous experience in using these panel type for the Rainier Square Tower in Seattle resulted in minimum plate thicknesses used of ½ in., regardless of demands on the panels. This was ultimately a fabricator and erector preference and is the limit they felt could be practically handled in their particular situation. Additionally, the governing equations presented earlier relate to limits for the empty steel modules, which highlighted that the empty module stability is tied closely to the effective shear stiffness of the empty modules.

There is no prequalified seismic concrete-filled composite coupling beam to wall connection, but research is ongoing on this topic by the authors. Designing the coupling beam-to-wall connection for seismic applications is challenging since the connection should provide specific ductility and rotation capacity. By contrast, for the nonseismic design, the design strength of the coupling beam-to-wall connection should only be equal to, or greater than, the required forces of the coupling beam.

In seismic applications, the structural performance (stiffness and ductility) of uncoupled or coupled C-PSW/CF systems is based on an assumption that the wall-to-foundation connections do not fail prior to the formation of plastic hinges in the walls and coupling beams. By contrast, the nonseismic design of the wall-to-foundation connection of a planar (uncoupled) or coupled C-PSW/CF system is done in accordance with the required force demand. That is, the foundation connections need only be strong enough to resist the required moments and forces at the base of C-PSW/CF.

Although the design strength of the wall-to-foundation connection should be equal to, or greater than, the required moments and forces, the rotational stiffness of the wall-to-foundation has a direct impact on the wind design of uncoupled and coupled C-PSW/CF. As uncoupled C-PSW/CF systems behave structurally like a cantilever beam, the assumed rotational stiffness of the wall-to-foundation connection is critical in estimating the overall drift of the structure. This type of structural behavior leads to lateral deformation limits governing most wind design cases of uncoupled C-PSW/CF systems. Comparatively, in coupled C-PSW/CF, the rotational stiffness of the foundation connection has an effect on the force or moment distribution along the height and lateral deformation, as the system resists the lateral loads by developing coupling action.

An investigation into wall-to-foundation connections for wind applications is ongoing by authors. Three potential wall-to-foundation connection options are illustrated in Figure 5 (JEA, 2005). As shown in Figure 5(a), the steel plates can be continued and embedded into the concrete foundation using stud anchors welded to the steel faceplates. The
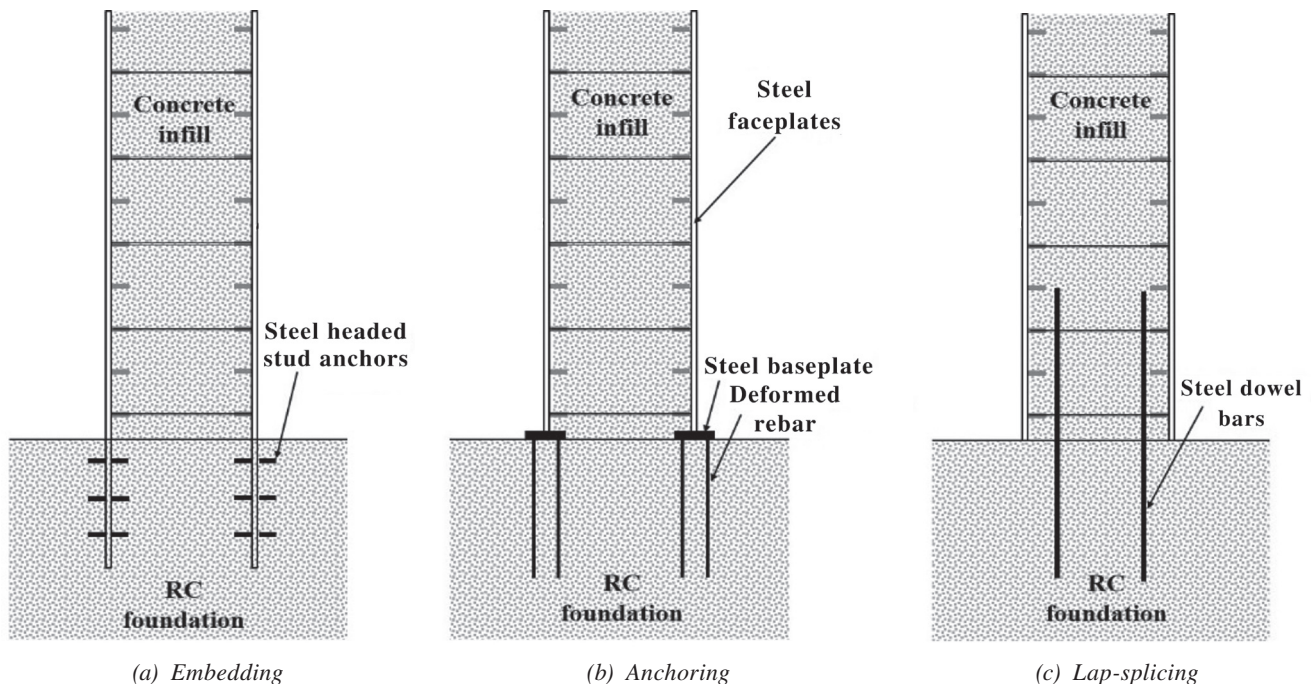

(a) Embedding   *(b) Anchoring*   *(c) Lap-splicing*

Fig. 5. Three different anchoring techniques (adapted from JEA, 2005).

steel plates can also be welded to baseplates with anchor bars that are embedded into the concrete foundation, as shown in Figure 5(b). Alternatively, steel dowel bars can be used to transfer the forces from the C-PSW/CF to the reinforced concrete foundation, as shown in Figure 5(c). Selection of the anchoring option depends on the required strength for the connection and constructor preferences.

WIND DESIGN PROCEDURE FOR C-PSW/CF

The wind design procedure for uncoupled and coupled C-PSW/CF systems is described in the following sections. The requirements presented in the previous sections and applicable building codes are used to develop the wind design procedure.

Wind Design Procedure for Uncoupled C-PSW/CF

This section presents a design procedure for the wind application of uncoupled (planar) C-PSW/CF systems. Figure 6 shows a flowchart summarizing the general wind design procedure for planar C-PSW/CF. A description for each step of the uncoupled C-PSW/CF design process is presented next.

Step 1: General Information of the Considered Building

In this step, the initial design information such as building location, geometry, architectural requirements, number of stories, story height, floor dimension, building importance, material properties, etc., is collected.
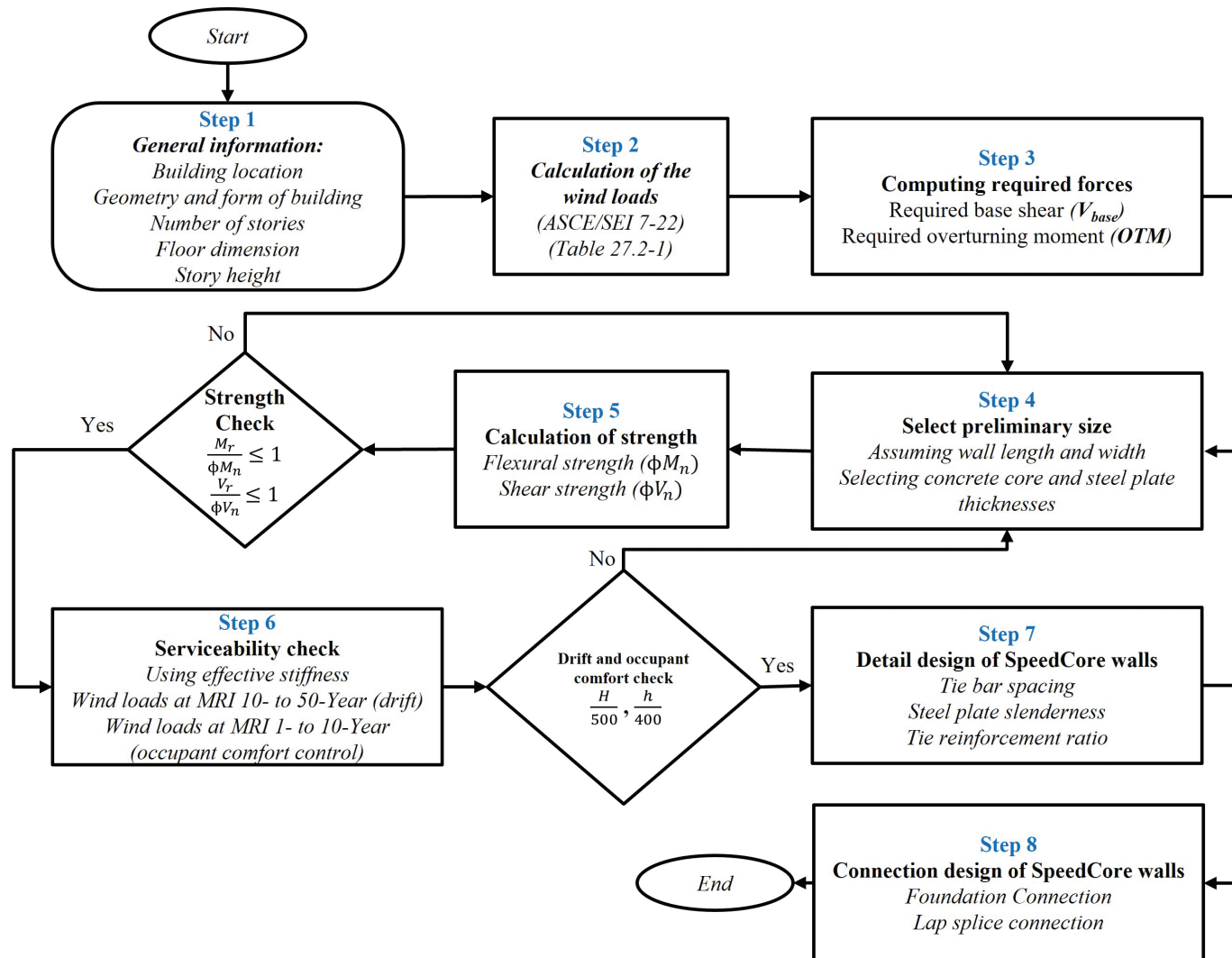

Fig. 6. Flowchart showing general wind design procedure for planar C-PSW/CF.

Step 2: Calculation of the Wind Loads

The C-PSW/CF are designed to resist the code-specified wind loads. In the absence of any wind tunnel testing or other special requirements for the given structure, design wind loads shall be determined based on the location and geometry (form)/building envelope according to ASCE 7, *Minimum Design Loads for Buildings and Other Structures* (2016). The wind loads are determined using the seven-step procedure (simplified procedure) provided in Table 27.2-1 of ASCE 7-16. Basic wind speed for the considered risk category is selected according to ASCE 7-16, Figure 26.5.1-B, to calculate wind loads for the strength design. Additionally, wind loads at mean recurrence interval (MRI) of 10-year or 50-year wind speed are also used to check the drift and occupant comfort checks. It is recommended that drift control of $H/500$ (roof total drift) and $h/400$ (maximum interstory drift) at 10-year MRI be used for the drift check of SpeedCore systems.

Step 3: Calculation of Base Shear and Overturning Moment

The design wind loads determined in Step 2 for the specific risk category are used to calculate the demand base shear and overturning moment (OTM). For uncoupled C-PSW/CF, the required base shear and OTM can be calculated by hand without conducting computational analysis.

Step 4: Select Preliminary Size for the Uncoupled C-PSW/CF

The size of uncoupled C-PSW/CF components is selected in this step considering the floor layout, architectural plan, and required base shear and moment. Components sized at this point include the total wall length, L_{wall}, wall thickness, t_{sc}, and steel plate thickness, t_p. No specific recommendations for the initial sizing are provided in this paper because there could be multiple drivers for sizing components, including architectural requirements, fabricator and erector preference, and designer experience with the system.

Step 5: Strength Check of Uncoupled C-PSW/CF

The flexural strength of the selected planar C-PSW/CF is calculated using one of the methods presented in the AISC *Specification* and compared with the required OTM. The shear strength is calculated using Equation 8 and is compared with the required base shear. If the strength check is not satisfied, the size of uncoupled C-PSW/CF should be revised, and the procedure restarts from Step 4. In design of mid- or high-rise buildings, the strength of planar C-PSW/CF is considerably higher than the demand forces as serviceability (drift limits) generally governs the design.

Step 6: Serviceability (Drift and Occupant Comfort) Check of Uncoupled C-PSW/CF

The lateral deflection is checked to evaluate the serviceability of the uncoupled C-PSW/CF system. The deflection limit for the wind loads is on the order of $1/600$ to $1/400$ of the building or story height (ASCE Task Committee on Drift Control of Steel Building Structures, 1988; Griffis, 1993). AISC Design Guide 3 (Fisher and West, 2003) recommends the roof lateral deflection due to wind loading be limited to $H/500$ using a 10-year mean recurrence interval (MRI) wind pressure, where H is the total height of the building, or $h/400$ for interstory drift, where h is the story height. A commercial finite element program can be used to calculate the roof displacement and interstory drift of uncoupled C-PSW/CF systems. The effective stiffnesses of planar walls presented in the AISC *Specification* are used to estimate the lateral deflection. The effect of the rotational stiffness of the wall-to-foundation connection is also considered in the calculation of lateral deflection. If the drift check is not satisfied, the size of uncoupled C-PSW/CF should be revised, and the procedure restarts from Step 4.

Step 7: Detail Design of Uncoupled C-PSW/CF

In this step, the tie bar spacing and tie bar diameters of planar C-PSW/CF are designed to satisfy the slenderness limits and tie reinforcement ratio requirements. Slenderness limits and tie bar requirements are presented in previous sections. It should be noted that the stability of the empty steel module governs the required tie bar diameter of C-PSW/CF.

Step 8: Connection Design of Uncoupled C-PSW/CF

Finally, after designing the uncoupled C-PSW/CF, the wall-to-foundation connection is designed based on the calculated required strengths. The composite wall splices are also designed based on the calculated demands (required strengths) at the corresponding locations. It is important to consider that when the wall-to-foundation connection is designed according to the demands, the correct rotational stiffness of the connection should be used in Step 6 to check the drift.

Wind Design Procedure for Coupled C-PSW/CF

This section describes the wind design procedure for coupled C-PSW/CF systems. Figure 7 shows a flowchart summarizing the general wind design procedure for coupled C-PSW/CF systems. Working through the noted steps will provide sizing for the walls and coupling beams. A description for each step of the coupled C-PSW/CF design process is presented next.

Step 1: General Information of the Considered Building

This step is similar to Step 1 for uncoupled C-PSW/CF. The building information is collected and compiled, which includes the building location, floor dimension, number of stories, and story height.

Step 2: Calculation of the Wind Loads

Step 2 for coupled C-PSW/CF is also similar to Step 2 for uncoupled C-PSW/CF discussed previously.

Step 3: Select Preliminary Sizes for C-PSW/CF and Coupling Beams

The C-PSW/CF and coupling beams cross-sections are preliminarily sized in this step considering floor layout and architectural design. This includes selecting the wall length, L_{wall}, wall thickness, t_{sc}, steel plate thicknesses, t_p,

and infill concrete core thickness. In addition, the coupling beam depth, h_{CB}, width, b_{CB}, web plate thickness, $t_{pw.CB}$, flange plate thickness, $t_{pf.CB}$, and length, L, are also selected in this step. Recommendations for sizing are not included in this paper because engineering experience and judgement are needed for selecting initial sizes.

Step 4: Calculation of Required Forces

The distribution of forces along the height of coupled C-PSW/CF is directly influenced by the stiffnesses of the C-PSW/CF walls and coupling beams. A finite element model of the coupled C-PSW/CF system is developed using the effective stiffnesses for the composite walls and coupling beams. A commercial structural analysis program can be used to conduct the analysis and calculate the design demands (also referred to as required strengths).
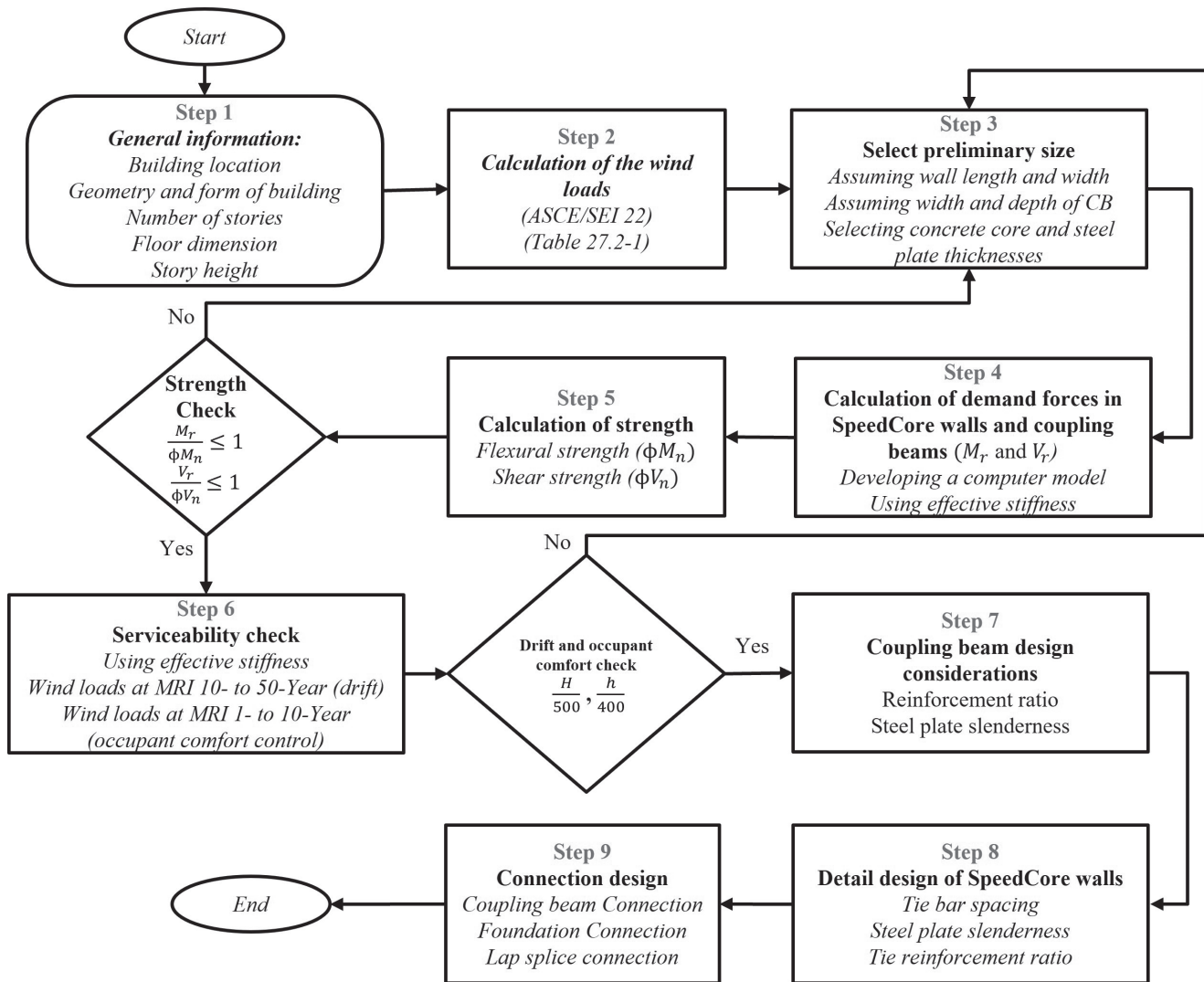
Fig. 7. Flowchart showing general wind design procedure of coupled C-PSW/CF.

Step 5: Strength Check of C-PSW/CF and Coupling Beams

The flexural strength of the selected C-PSW/CF is calculated and compared with the required OTM. The shear strength is calculated using Equation 8 and is compared with the required base shear. Additionally, the design flexural and shear strengths of coupling beams are calculated as outlined in the "Design Requirements for Coupling Beams." If the strength check is not satisfied, the size of coupling beams or C-PSW/CF are revised, and the procedure restarts from Step 4. In the design of mid- to high-rise buildings, the coupling beam strength typically governs the design, and the strengths of C-PSW/CF are considerably higher than the demand forces. In some cases, the lateral drift limits for wind loading govern the design of coupled C-PSW/CF.

Step 6: Serviceability (Drift and Occupant Comfort) Check of Coupled C-PSW/CF

A structural analysis is conducted in this step using a mean recurrence interval (MRI) of 10-year wind loads to check the drift limits. Appropriate effective stiffnesses of the composite walls and coupling beams are used in the structural analysis models of the coupled C-PSW/CF. The lateral deflection due to wind loading is limited to $H/500$, where H is the total height of the building, and the story drift is limited to $h/400$, where h is the story height. Although the rotational stiffness of the wall-to-foundation connection has a small effect on coupled systems due to the benefits of coupling action, the connection stiffness can be included to improve the estimation of lateral displacements. If the roof displacement or interstory drift requirements are not met, the sizes of members (C-PSW/CF or coupling beams) are revised, and the procedure restarts from Step 3.

Step 7: Detail Design of Coupling Beams

The section slenderness requirements and limits for the coupling beams are checked. These slenderness limits were identified previously. The geometric size and details of the coupling beams are used to assess coupling beam-to-wall connection possibilities.

Step 8: Detail Design of C-PSW/CF

Tie bar size (diameter) and spacing of planar C-PSW/CF are designed to satisfy the slenderness limits and tie reinforcement ratio requirements outlined previously.

Step 9: Connection Design

The composite wall-to-foundation (or subgrade structure) connections are designed based on the calculated demands (required strengths). The coupling beam-to-composite wall connections are designed based on the calculated demands (required strengths) at the corresponding levels. The composite wall splices are also designed based on the calculated demands (required strengths) at the corresponding locations.

Wind Design Example of 15-Story Planar and Coupled C-PSW/CF

The following design example presents the wind design procedure of planar (uncoupled) and coupled C-PSW/CF structures discussed in the previous sections. The structure considered in this design is a 15-story office building located in Chicago, Illinois (41.8847687° N, −87.6231634° W), where wind loads are expected to govern the design. Figure 8 illustrates the floor plan of the structure, which has a 200×120 ft footprint. The structure consists of two planar (uncoupled) C-PSW/CF in the East–West direction and two coupled C-CPSW/CF in the North–South direction. The first story height is 17 ft, and the typical story height is 14 ft. The total height of the structure is 213 ft. It is also assumed the floor loading is 120 psf (including superimposed dead loads), resulting in the total structural weight of 43,200 kips. In this example, the uncoupled C-PSW/CF system is designed first, followed by the coupled C-PSW/CF. The design assumed ASTM A992 steel for all steel shapes, ASTM A572, Grade 50 steel for all plates, and a Young's modulus of 29,000 ksi for all steel. The design also assumed normal weight concrete with a compressive strength of 6 ksi and Young's modulus of 4,415 ksi.

The wind loads for the considered building were determined using ASCE 7-16, Chapters 26–27. Table 1 shows the respective wind hazards and basic wind speeds for Chicago per ASCE 7-16. The wind pressures in the East–West direction are used to design planar (uncoupled) C-PSW/CF, and the wind pressures in the North–South direction are considered for the design of coupled C-PSW/CF. The main wind force-resisting system (MWFRS) of the building is designed for four different load cases presented in ASCE 7-16, Figure 27.3-8. The considered building satisfies the requirements in ASCE 7-16, Section D.1, as a torsionally regular building. Therefore, it only needs to be designed for Case 1, as shown in ASCE 7-16, Figure 27.3-8.

The wind loads were determined using the seven-step procedure provided in ASCE 7-16, Table 27.2-1. Table 2 presents a summary of wind pressures on the surface of the building determined using ASCE 7-16, Chapters 26–27, using the basic wind speed for risk category II. The wind pressures are multiplied with the exterior surface area (facades) of the building to calculate the wind loads. Wind loads calculated using wind speed for the given risk category are used for the strength design. Additionally, wind loads computed using a wind speed at the 10-year MRI are considered for checking the lateral deformation of the building to meet serviceability requirements.

Table 1. Basic Wind Speed for Buildings Located in Chicago	
Wind Hazard	Basic Wind Speed
MRI 10-year	74 mph
MRI 25-year	80 mph
MRI 50-year	85 mph
MRI 100-year	92 mph
Risk Category I	100 mph
Risk Category II	107 mph
Risk Category III	114 mph
Risk Category IV	119 mph

Table 2. Design Wind Pressure (Risk Category II) in the East–West and North–South Directions										
Story No.	Story Height (ft)	K_z	q_z (psf)	External Pressure East–West Direction			External Pressure North–South Direction			Internal Pressure (psf)
				Windward (psf)	Leeward (psf)	Side (psf)	Windward (psf)	Leeward (psf)	Side (psf)	
15	213	1.63	40.7	28.3	−17.7	−24.8	28.9	−13.2	−25.2	±7.83
14	199	1.62	40.2	28.0	−17.7	−24.8	28.5	−13.2	−25.2	±7.83
13	185	1.59	39.7	27.7	−17.7	−24.8	28.2	−13.2	−25.2	±7.83
12	171	1.57	39.2	27.3	−17.7	−24.8	27.8	−13.2	−25.2	±7.83
11	157	1.55	38.6	26.9	−17.7	−24.8	27.4	−13.2	−25.2	±7.83
10	143	1.52	37.9	26.4	−17.7	−24.8	26.9	−13.2	−25.2	±7.83
9	129	1.50	37.3	25.9	−17.7	−24.8	26.4	−13.2	−25.2	±7.83
8	115	1.47	36.6	25.5	−17.7	−24.8	25.9	−13.2	−25.2	±7.83
7	101	1.44	35.8	24.9	−17.7	−24.8	25.3	−13.2	−25.2	±7.83
6	87	1.40	34.8	24.3	−17.7	−24.8	24.7	−13.2	−25.2	±7.83
5	73	1.36	33.8	23.5	−17.7	−24.8	23.9	−13.2	−25.2	±7.83
4	59	1.31	32.6	22.7	−17.7	−24.8	23.1	−13.2	−25.2	±7.83
3	45	1.25	31.1	21.6	−17.7	−24.8	22.0	−13.2	−25.2	±7.83
2	31	1.17	29.1	20.3	−17.7	−24.8	20.6	−13.2	−25.2	±7.83
1	17	1.05	26.2	18.3	−17.7	−24.8	18.6	−13.2	−25.2	±7.83

Wind Design of the Uncoupled C-PSW/CF System

This section presents the wind design of the planar (uncoupled) C-PSW/CFs in the East–West direction of the given building. The design of these uncoupled C-PSW/CFs is accomplished according to the design procedure presented in Section 6.

Step 1: General Information of the Considered Building

As shown in Figure 8, there are two uncoupled C-PSW/CF in the West–East direction to resist that wind loads. The length of the planar C-PSW/CF considered is 25 ft. The planar C-PSW/CF resist a small portion of gravity loads (dead load), as shown in Figure 8; therefore, the axial compression force due to gravity loads and C-PSW/CF self-weight is not considered in the design.

Step 2: Calculation of the Wind Loads

Basic wind speeds for risk category II and the 10-year MRI are used in calculation of the wind loads for the wind design (strength check) and serviceability control (drift check), respectively. For Chicago, the basic wind speed is 107 mph for Risk Category II, and the 10-year MRI is 74 mph, as shown in Table 1.

Step 3: Calculation of Base Shear and Overturning Moment

As there are two planar C-PSW/CF in the West–East direction, each wall resists one-half of the wind loads. The required base shear and overturning moment at the base of the planar C-PSW/CF are calculated either by hand calculations or from computer-aided structural analysis. The wind loads calculated for Risk Category II are used to calculate the demand base shear and OTM for uncoupled C-PSW/CF. The wall can be assumed like a cantilever beam subjected to wind loads, so the shear force and overturning moment are simply calculated by hand. The required base shear and moment for each planar wall are 490 kips and 6.96×10^5 kip-in., respectively.

Step 4: Select Preliminary Size for the Uncoupled C-PSW/CF

In this step, the preliminary size of the planar wall is selected. The uncoupled C-PSW/CF length and thickness are assumed to be 300 in. (25 ft) and 18 in., respectively. A steel plate thickness of ½ in. is selected mainly because of construction considerations, including welding requirements and the stability of empty modules during construction and concrete casting. Also, a thicker steel plate allows larger tie bar spacing, which results in more economical fabrication of modules. Figure 9 and Table 3 show the cross-section details of uncoupled C-PSW/CF in the West–East direction.

Step 5: Strength Check of Uncoupled C-PSW/CF

The design flexural and shear strengths, $\phi M_{n,wall}$ and $\phi V_{n,wall}$, respectively, of planar C-PSW/CF sections are calculated in this step. The flexural strength for the planar wall in this example is calculated for the cross section, assuming the plastic stress distribution method where all steel plates reach F_y and concrete in compression reaches $0.85f_c'$, while concrete in tension is assumed not to contribute to the strength. The shear strength of the wall is calculated using Equation 8. Table 4 presents the flexural and shear strength of each planar wall and the comparison with the demand. As shown in the table, the strength of the uncoupled C-PSW/CF is considerably higher than the required
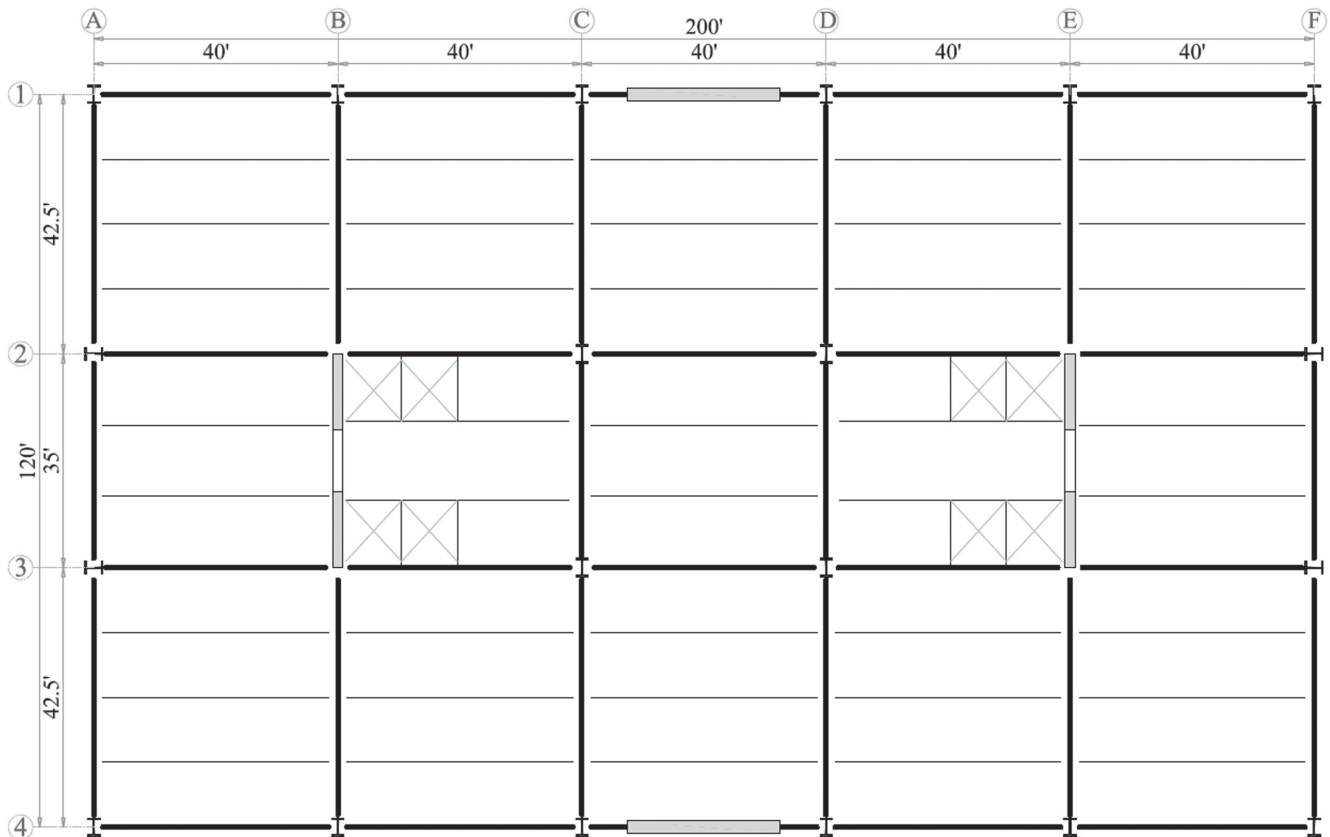

Fig. 8. Floor framing plan of the considered structure.

Table 3. Details of Uncoupled C-PSW/CFs in the West–East Direction				
Uncoupled C-PSW/CF	t_{pf}, in.	t_{pw}, in.	Length, in.	Wall Thickness, in.
	½	½	300	18

Table 4. Strength of Uncoupled C-PSW/CF and Comparison with Required Forces						
Uncoupled C-PSW/CF	$\phi M_{n,wall}$ kip-in.	$\phi V_{n,wall}$ kips	$M_{r,wall}$ kip-in.	$V_{r,wall}$ kips	$\dfrac{M_{r,wall}}{\phi M_{n,wall}}$	$\dfrac{V_{r,wall}}{\phi V_{n,wall}}$
	1.60×10^6	12,200	6.96×10^5	490	0.45	0.06

forces. It should be noted that the design of uncoupled C-PSW/CF structures is generally governed by drift limits; in other words, the flexural stiffness of planar C-PSW/CF governs the wind design. Again, the web and flange plate thicknesses of ½ in. are chosen due to construction considerations, including the welding of modules, stability of empty steel modules during erection, and concrete casting.

Step 6: Serviceability (Drift and Occupant Comfort) Check of Uncoupled C-PSW/CFs

Wind loads calculated using the wind speed at the 10-year MRI are used to check drift requirements. A finite element model, using a commercial software program (SAP2000) (CIS, 2017), of the planar C-PSW/CF can be utilized to check the serviceability and occupant comfort (drift limits). In order to estimate the lateral deflection of uncoupled C-PSW/CF, the effective stiffnesses of planar walls are used in the structural analysis. Additionally, the flexibility of the wall-to-foundation connection increases the lateral deflection; therefore, the rotational stiffness of foundation connection is considered in structural analysis for the drift check.

According to AISC *Specification* (2016b), Chapter B Commentary (Figure C-B3.3), a fully restrained connection shall provide a rotational stiffness at the support greater than or equal to 20 times the flexural stiffness, *EI*, divided by length of member. The required rotational stiffness, $K_{s.con}$, for a foundation connection to be considered fully restrained against rotation is calculated for a planar C-PSW/CF wall using Equation 16. The EI_{eff} given in the equation is the effective flexural stiffness of the uncoupled C-PSW/CF, and *H* is the total height of building.

$$K_{s.con} = \frac{20EI_{eff}}{H} \quad (16)$$

A two-dimensional finite element model of the planar C-PSW/CF for the given structure was developed using a commercial software program (using beam elements). The effective stiffness of the wall was used in the model, and both a completely fixed-base connection and a rotational spring with a stiffness calculated using Equation 16 were considered. Figure 10 shows the model output in terms of (1) the deformation shape, (2) story displacements over the height for both a fixed boundary condition (Fixed B.C.) assumption and rotational spring boundary condition (Spring B.C.), and (3) the interstory drift for both a fixed boundary condition assumption and rotational spring boundary condition. As shown in the figure, using a completely fixed boundary condition at the base of the planar wall results in a 4.1 in. roof displacement. Assuming a rotational spring at the base
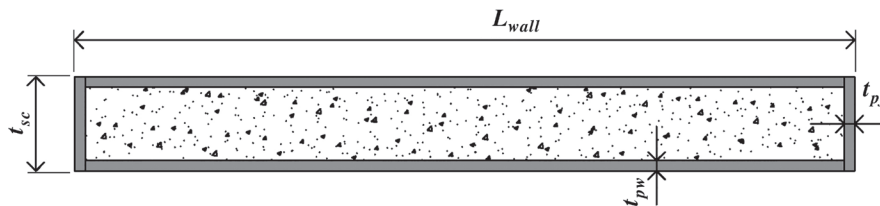

Fig. 9. Cross section of uncoupled C-PSW/CF.

with rotational stiffness calculated by Equation 16 gives a roof displacement of 4.9 in. In this case, considering the rotational stiffness of foundation connection increases the roof displacement by 19%; this highlights the importance of considering the foundation stiffness in checking drift limits for planar C-PSW/CF systems. Lateral drift ($H/500$) and interstory drift ($h/400$) requirements are 5.11 in. and 0.25%, respectively. Hence, the structure meets drift requirements based on the criteria checked. Also, as has been shown in this analysis, the rotational stiffness assumed for the foundation connection has a direct influence on lateral displacements. Therefore, the wall-to-foundation connection stiffness should be considered in the wind design of uncoupled C-PSW/CF structures.

While not a specific design step, it is important to discuss the assumed parameters that can impact drift calculations and, hence, the design of planar C-PSW/CF systems. A sensitivity study to further investigate the effect of flexural stiffness of uncoupled C-PSW/CF on the lateral load response was conducted. A 2D nonlinear finite element model of the uncoupled C-PSW/CF in the given structure was developed using the Abaqus finite element software (2016) and compared with the SAP2000 commercial software model (CIS, 2017). Layered composite shell elements (S4R) were used to model composite walls and three-dimensional truss elements (T3D2) were used for steel flange plates in the Abaqus model. Nonlinear material properties were considered for both steel and concrete. The detailed description of the development of C-PSW/CF model was presented in previous works written by Shafaei et al. (2019) and Bruneau et al. (2019).

Figure 11(a) shows the lateral deformation of 2D nonlinear finite element models of uncoupled C-PSW/CF subjected to wind loads at the 10-year MRI. Figure 11(b) shows the calculated lateral displacements of the uncoupled wall considering four different models using SAP2000 and Abaqus. In one model using SAP2000, the uncracked flexural stiffness, EI_{uncr}, of the wall was used, which resulted in a roof displacement of 2.3 in. Another 2D finite element model with Abaqus was developed using elastic material properties of steel and concrete (no concrete cracking in tension), resulting in a roof displacement of 2.45 in. There is a small difference between the Abaqus and SAP2000 models because the SAP2000 model has beam elements (considering only the flexural behavior), but the elastic Abaqus model has composite shell elements (2D finite element model), which considers the shear deformation of the planar C-PSW/CF as well. Using the effective flexural stiffness

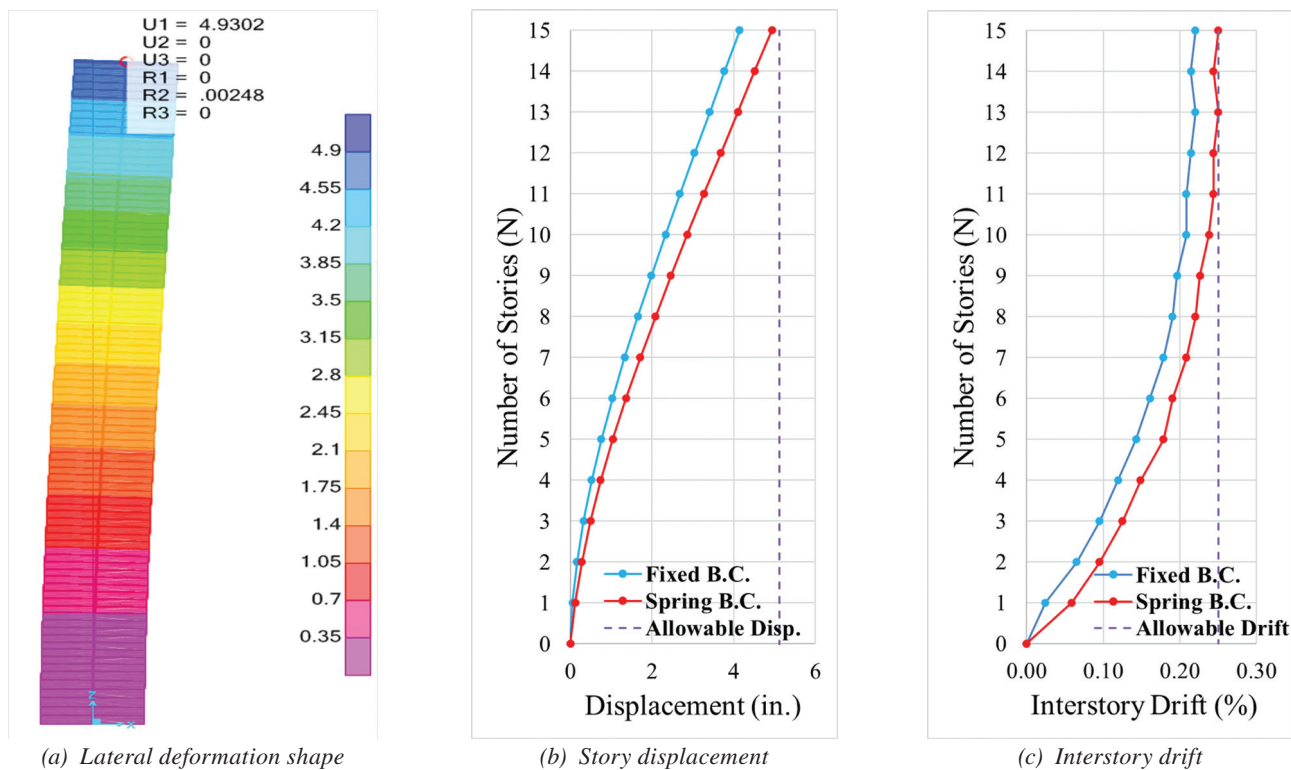(a) Lateral deformation shape   (b) Story displacement   (c) Interstory drift

Fig. 10. Uncoupled C-PSW/CF subjected to wind loads at a 10-year MRI.

of the wall in SAP2000 model results in a roof displacement of 4.9 in., while the Abaqus 2D finite element model using nonlinear material properties of steel and concrete (considering the concrete cracking in tension) gives a roof displacement of 4.2 in. Note that for completeness, other wind speeds were checked in the models and are shown in Figure 12.

The results of these analyses show that using the effective flexural stiffness for a planar wall along the height is a conservative approach when investigating serviceability requirements (drift check). Using the effective flexural stiffness in the higher stories of the building, where concrete may not have cracked, is generally a conservative assumption. In the wind design of tall buildings, it is recommended that the cracking moment for the planar C-PSW/CF be calculated and that the uncracked flexural stiffness be used for the walls, where the required moment is lower than the cracking moment.

Step 7: Detail Design of Uncoupled C-PSW/CF

This step determines the tie bar diameter and spacing requirements based on the stability of the empty steel modules. The tie spacing for the uncoupled C-PSW/CF considered 12 in., which results in a plate slenderness ratio of 24.

The plate slenderness ratio is lower than the required value, as shown in Equation 17.

$$\frac{S_{tie}}{t_p} = 24.0 \;\; < \;\; 1.2\sqrt{\frac{E_s}{F_y}} = 28.9 \tag{17}$$

The tie bar diameter and spacing requirements should also be checked for the stability of the empty steel modules during erection and concrete casting. Tie bars with ⅝ in. diameters are selected for the uncoupled walls. This gives an α value of 23.7 and slenderness requirement of 24.5. As shown in Equations 18 and 19, the tie bar requirements for the empty steel module are satisfied.

$$\alpha = 1.7\left(\frac{t_{sc}}{t_p} - 2\right)\left(\frac{t_p}{d_{tie}}\right)^4 = 23.7 \tag{18}$$

$$\frac{S_{tie}}{t_p} = 24.0 \;\; < \;\; 1.0\sqrt{\frac{E_s}{2\alpha+1}} = 24.5 \tag{19}$$

Step 8: Connection Design of Uncoupled C-PSW/CF

The wall-to-foundation and wall-to-wall connections are designed based on the required forces. In this paper, the connection design (wall-to-foundation and wall-to-wall connection design) is not covered, as it is beyond the scope of this study.

(a) Lateral deformation of
2D finite element model

(b) Lateral displacements
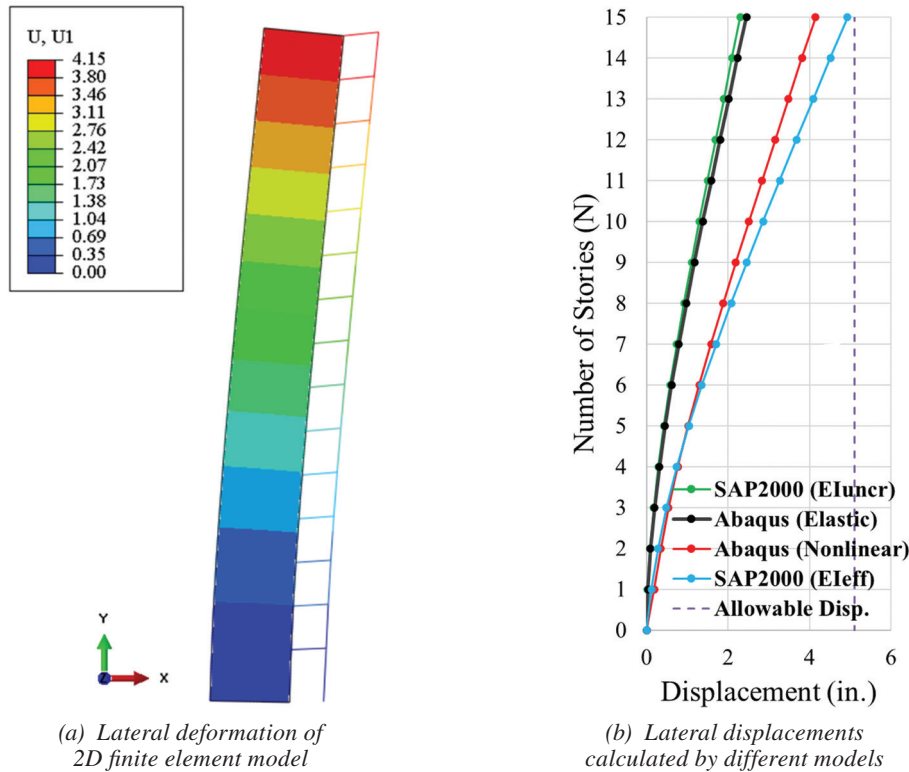calculated by different models

Fig. 11. Uncoupled C-PSW/CF subjected to wind loads at a 10-year MRI.

Wind Design of Coupled C-PSW/CF

For the building considered in this design example, two coupled C-PSW/CF are used to resist the wind loads in the North–South direction. This section presents the wind design of coupled C-PSW/CF.

Step 1: General Information of the Considered Building

In the North–South direction, coupled C-PSW/CF with overall lengths of 35 ft are used to resist the wind loads, as depicted in Figure 8. The coupled C-PSW/CF consist of two 12.5-ft (150-in.)-long planar walls and composite coupling beams with a length of 10 ft (120 in.). The lengths in this case were chosen to fit the geometric requirements of the building, and similarly, in practice, architectural consideration would like to dictate the layout and lengths of these components. Each coupled C-PSW/CF resists gravity loads of a tributary area of 2633 ft^2, as shown in Figure 8, which results in 158 kips of axial compression force at the individual wall at each story. The total axial compression force on the individual C-PSW/CF is 2,370 kips at the first floor.

Step 2: Calculation of the Wind Loads

The wind speeds for Risk Category II and the 10-year MRI are used to calculate the wind loads for the design of members (strength check) and controlling drift limits

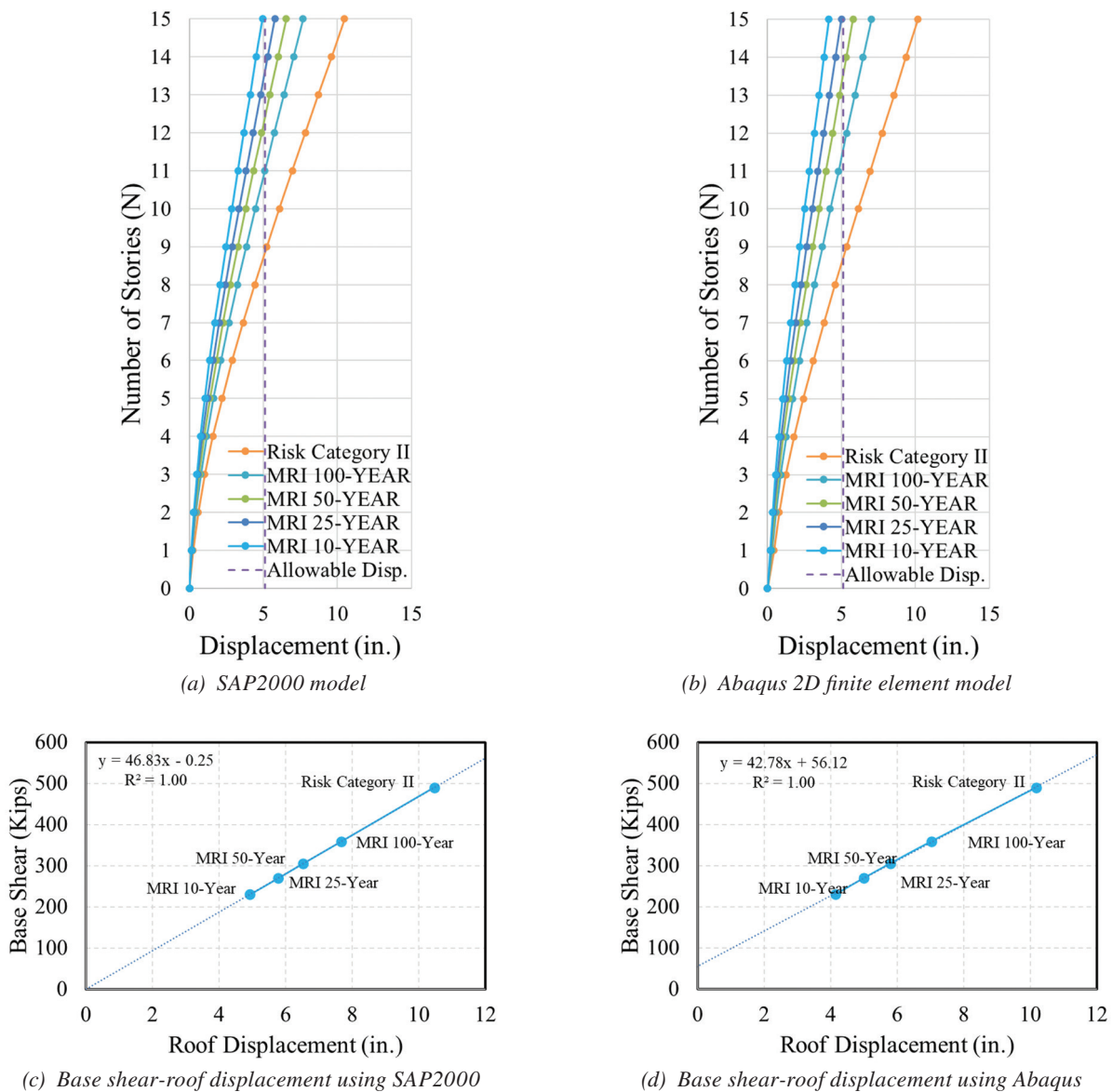
(a) SAP2000 model

(b) Abaqus 2D finite element model

(c) Base shear-roof displacement using SAP2000

(d) Base shear-roof displacement using Abaqus

Fig. 12. Lateral displacement of uncoupled C-PSW/CF subjected to different wind loads.

Table 5. Details of C-PSW/CF in the North–South Direction				
Uncoupled C-PSW/CF	t_{pf}, in.	t_{pw}, in.	Length, in.	Wall Thickness, in.
	½	½	150	18

Table 6. Details of Coupling Beams in the North–South Direction				
Coupling beams	$t_{f.CB}$, in.	$t_{w.CB}$, in.	Depth, h_{CB}, in.	Width, b_{CB}, in.
	¾	½	24	18

Table 7. Required Moments and Forces in Walls and Coupling Beams					
C-PSW/CF				Composite Coupling Beams	
$M_{r,wall}$ kip-in.	$V_{r,wall}$ kips	$P_{r,wall}$ kips	$T_{r,wall}$ kips	$M_{r,CB}$ kip-in.	$V_{r,CB}$ kips
1.47×10^5	458	6,110	1,310	2.28×10^4	381

and occupant comfort of coupled C-PSW/CF in the North–South direction. Since two coupled C-PSW/CF are used in the North–South direction and the building is torsionally regular, one-half of the wind loads is resisted by each coupled system. The wind speeds for Risk Category II and 10-year MRI are 107 mph and 74 mph for Chicago, respectively, as given in Table 1. The resulting wind pressures are shown in Table 2.

Step 3: Select Preliminary Sizes for C-PSW/CF and Coupling Beams

The force and moment distribution along the height in a coupled C-PSW/CF depends directly on the wall and coupling beam sections. Therefore, the preliminary sizes of members need to be selected for calculating the required forces and moments of the members. In other words, member stiffnesses have a direct impact on the coupling ratio. Figure 13, Table 5, and Table 6 summarize the initial sizing

of the wall panels and coupling beams for this design example. As shown, the two planar C-PSW/CF in this example have a length, L_{wall}, of 12.5 ft (150 in.) and overall wall thickness, t_{sc}, of 18 in. Also, the chosen wall thickness is assumed suitable for architectural requirements of the building. Steel web and flange plate thicknesses, t_p, are initially sized at ½ in., which results in a 17-in.-thick concrete infill. The coupling beam width, b_{CB}, and depth, h_{CB}, are initially sized at 18 in. and 24 in., while coupling beam thicknesses are ¾ in. for the steel flange plates, $t_{f.CB}$, and ½ in. web plates, $t_{w.CB}$. The ½ in. wall plate thickness was chosen, like the case in the planar wall example, based on construction considerations including fabrication efficiency and handling the panels during erection.

Step 4: Calculation of Required Forces

This step involves determining the required design forces for the walls and coupling beams. The forces calculated
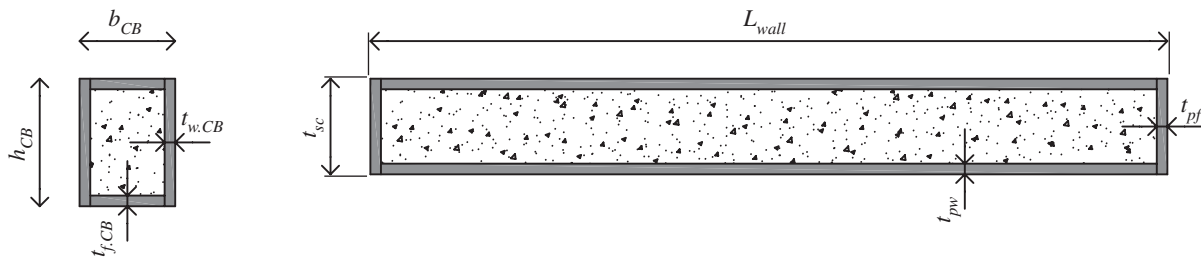

Fig. 13. Cross section of coupling beams and C-PSW/CF.

Table 8. Strength of Composite Coupling Beams and Comparison with the Demand						
Coupling beam	$\phi M_{n.CB}$ kip-in.	$\phi V_{n.CB}$ kips	$M_{r.CB}$ kip-in.	$V_{r.CB}$ kips	$\dfrac{M_{r.CB}}{\phi M_{n.CB}}$	$\dfrac{V_{r.CB}}{\phi V_{n.CB}}$
	2.25×10^4	699	2.28×10^4	381	1.02	0.55

Table 9. Strength of C-PSW/CF and Comparison with Demand							
C-PSW/CF	$\phi M_{n,wall.T}$ kip-in.	$\phi M_{n,wall.C}$ kip-in	$\phi V_{n,wall}$ kips	$M_{r,wall}$ kip-in.	$V_{r,wall}$ kips	$\dfrac{M_{r,wall}}{\phi M_{n,wall.T}}$	$\dfrac{M_{r,wall}}{\phi M_{n,wall.C}}$	$\dfrac{V_{r,wall}}{\phi V_{n,wall}}$
	3.81×10^5	5.27×10^5	6,120	1.47×10^5	458	0.39	0.28	0.07

include the base shear and moments acting on the walls, and coupling beam shear and moment demands. A structural analysis is conducted using the wind loads for Risk Category II to determine the demands. The effective stiffnesses for planar walls and coupling beams are considered to estimate the moments and forces distribution in the members. Table 7 summarizes the required forces and moments in walls and coupling beams, which were calculated considering the wind and dead load combination (wind + 0.90 dead load). Based on the structural analysis, the third-floor coupling beam has the highest required moment and shear force, and in this example, all the coupling beams are designed for these forces. Due to coupling action, tension and compression walls are subjected to axial loads of 1,313 and 6,113 kips, respectively. The overturning moment is 1.28×10^6 kip-in., and the calculated coupling ratio of the system, using Equation 1, is 77%.

Step 5: Strength Check of C-PSW/CF and Coupling Beams

The design flexural and shear strengths, $\phi M_{n,CB}$ and $\phi V_{n,CB}$, of composite concrete-filled coupling beams; the design flexural strengths of the walls in tension and compression, $\phi M_{n,wall.T}$ and $\phi M_{n,wall.C}$, and the design shear strengths of the walls, $\phi V_{n,wall}$, are calculated in this step. The flexural strength for the coupling beams and planar walls in this example is calculated for the cross section, assuming the plastic stress distribution method where all steel plates reach F_y and concrete in compression reach $0.85f_c'$, while concrete in tension is assumed not to contribute to the strength. The shear strength of the coupling beams and planar walls are calculated using Equations 15 and 8, respectively. Tables 8 and 9 present the design strength of coupling beams and C-PSW/CF and comparisons with the demands. As given in Table 8, the flexural strength of the coupling beam governs the design, and the flexural capacities of C-PSW/CF are considerably higher than the required moments.

Step 6: Serviceability (Drift and Occupant Comfort) Check of Coupled C-PSW/CF

Similar to the uncoupled walls, wind loads calculated using the wind speed at the 10-year MRI are used to check drift requirements. Two-dimensional finite element models, developed with the SAP2000 program (using beam elements), of the coupled walls for the considered structure use both a completely fixed-base connection and a rotational spring with a stiffness given from Equation 16. Figure 14 shows the model output in terms of (1) the deformation shape, (2) story displacements over the height for both a fixed boundary condition assumption and rotational spring boundary condition, and (3) the interstory drift for both a fixed boundary condition assumption and rotational spring boundary condition. As shown in the figure, using a completely fixed boundary condition at the base of the wall results in a 3.9 in. roof displacement, while assuming a rotational spring at the base with rotational stiffness calculated by Equation 16 gives a roof displacement of 4.2 in.

In the coupled wall case, considering the rotational stiffness of foundation connection increases the roof displacement by 7%; which is less than the impact for the planar wall-only case. The main reason that foundation stiffness is less important in the coupled wall case is that the coupled systems resist lateral loads by developing coupling action. As a result, considering the rotational stiffness of foundation increases slightly force and moment demands in the members. Lateral drift ($H/500$) and interstory drift ($h/400$) requirements are 5.1 in. and 0.25%. Hence, the structure meets drift requirements based on the criteria checked. Also, as has been shown in this analysis, the rotational stiffness assumed for the foundation connection has a direct influence on lateral displacements, while not as major as the planar wall case.

A sensitivity study to further investigate the effect of flexural stiffness of coupled C-PSW/CF on the lateral load response was conducted. A 2D nonlinear finite element
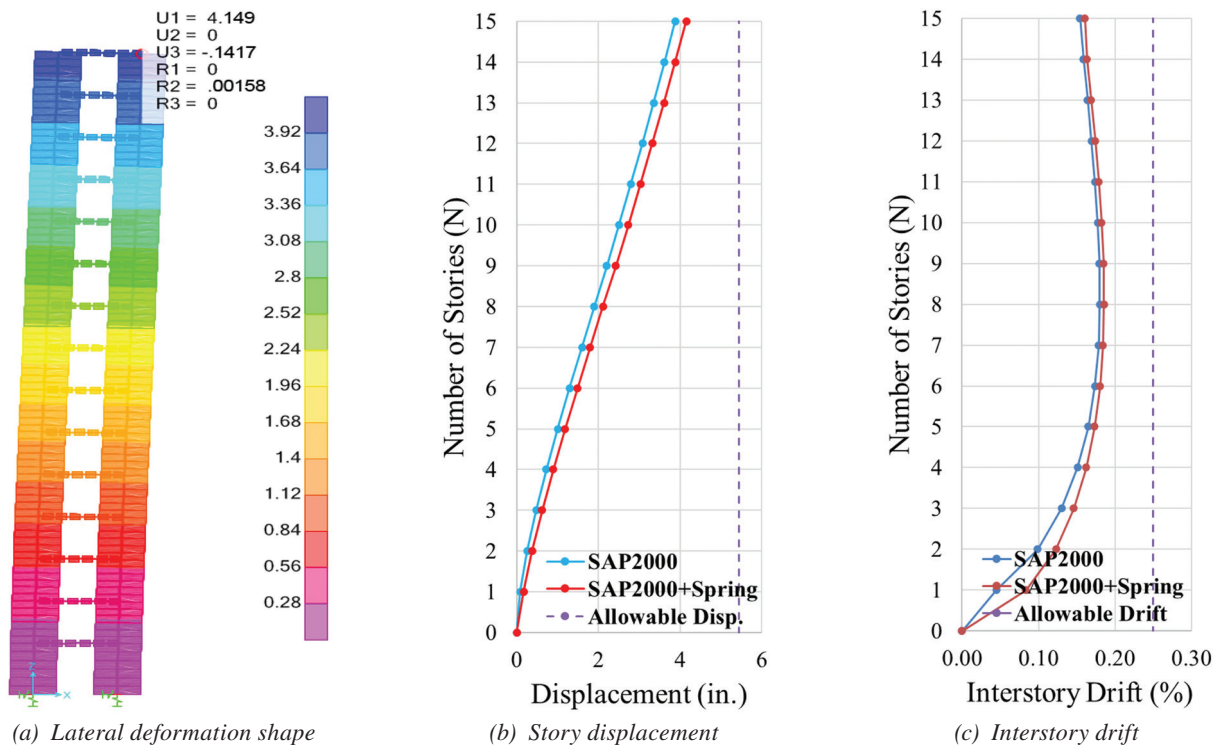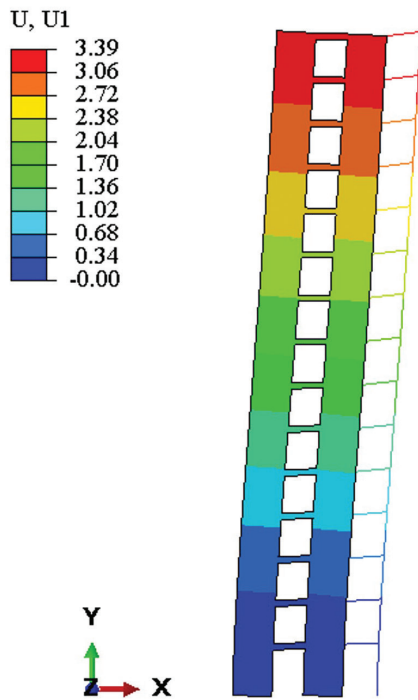
(a) Lateral deformation shape *(b) Story displacement* *(c) Interstory drift*

Fig. 14 Coupled C-PSW/CF subjected to wind loads at a 10-year MRI.

model of the uncoupled C-PSW/CF in the given structure was developed using the finite element software Abaqus and compared with the SAP2000 model. Layered composite shell elements (S4R) were used to model composite walls and three-dimensional truss elements (T3D2) were used for steel flange plates in the Abaqus model. Nonlinear material properties were considered for both steel and concrete. The detailed description of the development of C-PSW/CF model was presented in previous works written by Shafaei et al. (2019 and Bruneau et al. (2019).

Figure 15 shows the lateral deformation of 2D nonlinear finite element models (developed through the Abaqus program) of uncoupled C-PSW/CF subjected to wind loads at the 10-year MRI. Figure 15(b) shows the calculated lateral displacements of the coupled wall considering four different models using SAP2000 and Abaqus. There is a small difference between the elastic Abaqus and SAP2000 (using uncracked section stiffness) models because the SAP2000 model has beam elements (considering only the flexural behavior), but the elastic Abaqus model has composite shell elements (2D finite element model), which consider the shear deformation of the coupling beams and planar C-PSW/CF as well. Also shown in Figure 15(b), there is a difference between the Abaqus 2D nonlinear finite element model and SAP2000 (using beam elements with the effective stiffness). The reason is that the axial compression

forces (gravity loads) result in higher flexural stiffness of walls; in other words, the gravity loads prevent concrete cracking, as shown in Figure 16(a). All of the composite coupling beams undergo cracking as well as the bottom of C-PSW/CF, as shown in Figure 16. Due to this cracking, the effective flexural stiffness of concrete-filled composite coupling beams should be considered in SAP2000 model to estimate conservatively the lateral displacements. Note that for completeness, other wind speeds were checked in the models and are shown in Figure 17.

The results of these analyses show a fundamentally different structural behavior of the uncoupled and coupled wall systems subjected to lateral loading in mid-rise applications. While uncoupled walls primarily resist lateral loading through flexure, the coupled walls develop coupling action to resist applied loading. The practical implications of this are that uncoupled walls are more sensitive to assumptions of the foundation stiffness, and using the effective stiffness yields fairly conservative estimates of drift when applied at service level wind loading. For coupled systems, using the effective stiffness also conservatively captures drift estimations. Because concrete cracking in the coupling beams, even at service level winds, more closely matches the effective stiffnesses calculated from equations presented previously, effective flexural stiffness of coupling beams should be used for the serviceability check of coupled system. Also,
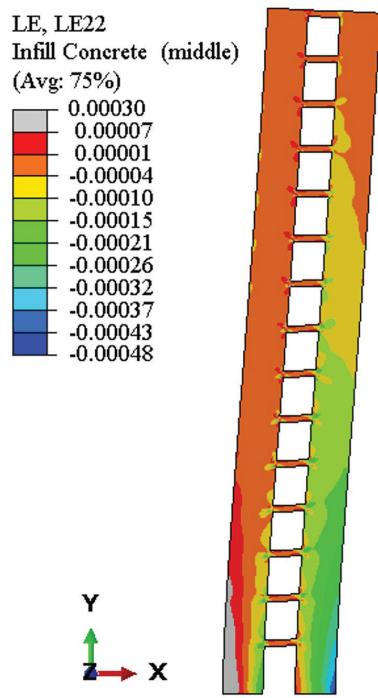
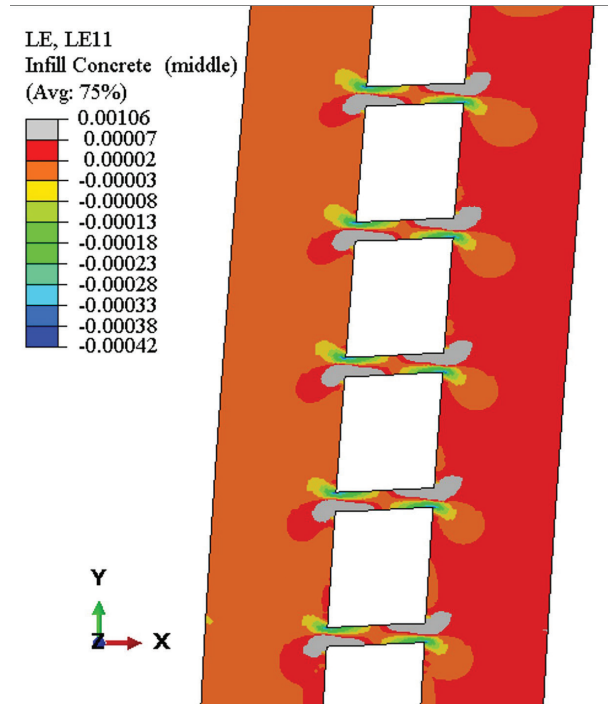*(a) Lateral deformation shape of 2D finite element model*
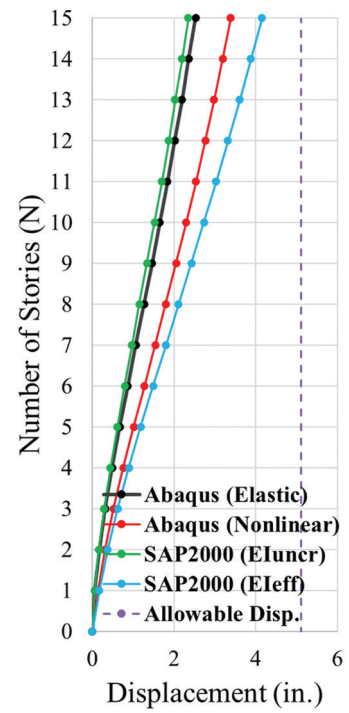
(b) Lateral displacements of models

Fig. 15. Coupled C-PSW/CF with different lateral stiffness.

(a) Concrete cracking strain at the bottom of C-PSW/CF

(b) Concrete cracking strain in coupling beams

Fig. 16. Strain distribution over the coupled C-PSW/CF model.

the coupled systems have less sensitivity to the assumed foundation stiffness, but considering the rotational stiffness of wall-to-foundation connections has a direct effect on the force and moment distributions along the height of the systems. From a design standpoint, in mid-rise structures, using the effective stiffness for checking drift limits in both uncoupled and coupled C-PSW/CF systems appears to be reasonable and conservative.

Step 7: Detail Design of Coupling Beams

In this step, the slenderness of composite coupling beams is checked for compactness requirements and also minimum steel requirements if composite coupling beams are used.

For the given case of a composite coupling beam, the compactness requirements are met, as are the minimum steel requirements. Also, the width of coupling beams (h_{CB}) and wall thickness (t_{sc}) are both 18 in., allowing for a constructible beam-to-wall connection.

Step 8: Detail Design of C-PSW/CF

This step determines the tie bar diameter and spacing requirements based on the stability of the empty steel modules. Tie bars with ⅝ in. diameter and 12 in. spacing are selected based on a ½ in. plate thickness. The process for determining the tie bar diameter and spacing is the same as for the planar wall-only case shown previously.

(a) Lateral displacements

(b) Interstory drift

(c) Base shear-roof displacement
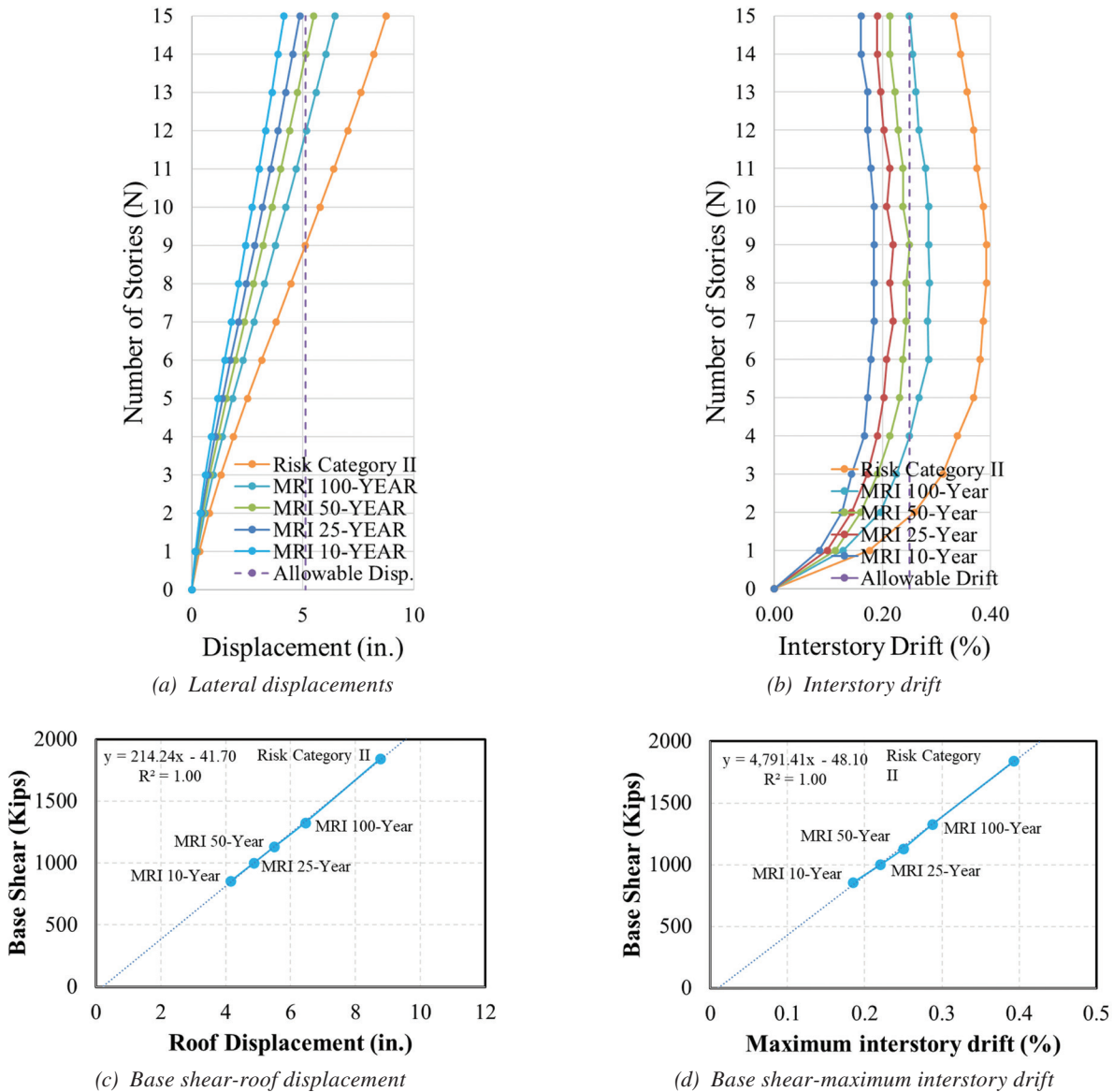
(d) Base shear-maximum interstory drift

Fig. 17. Coupled C-PSW/CF subjected to different wind loads using SAP2000.

Step 9: Connection Design

Finally, the coupling beam-to-wall, wall-to-foundation, and wall-to-wall connections are designed based on the required forces. The connection design is not included in this paper, as research on this topic is still ongoing by authors.

SUMMARY AND CONCLUSIONS

In this paper, wind (nonseismic) design requirements and procedures for uncoupled and coupled C-PSW/CF, also known as the SpeedCore system, were presented. A wind design example for a 15-story building located in Chicago using both planar (uncoupled) and coupled C-PSW/CF is provided. Conclusions and recommendations from this study are as follows:

1. Construction considerations generally govern the steel plate thickness for C-PSW/CF systems in mid-rise structures. Construction considerations include (a) the stability of empty modules during construction, (b) the adequacy to resist fresh concrete hydrostatic pressure, and (c) the weldability of the steel plates while avoiding excessive localized distortions in the assembled pieces.

2. It is recommended to use the provided effective stiffness for walls and coupling beams for the wind design of C-PSW/CF systems when a detailed nonlinear finite element model is not available.

3. In the wind (nonseismic) design, the strength of uncoupled C-PSW/CF systems is considerably higher than the demand in mid- to high-rise structures as drift limits tend to govern design.

4. The rotational stiffness of the wall-to-foundation connection has a direct influence on the lateral displacements of uncoupled C-PSW/CF systems because the behavior is analogous to a cantilever beam and lateral forces are resisted primarily through flexure. Hence, in the wind design of uncoupled C-PSW/CF, the rotational stiffness of the foundation connection should be considered to accurately estimate the lateral displacements.

5. The rotational stiffness of the wall-to-foundation connection has a marginal influence on the lateral displacement of coupled C-PSW/CF systems compared to uncoupled systems, as the coupled system resists lateral by developing coupling action. Additionally, considering rotational stiffness of wall-to-foundation connections has a direct influence on the force and moment distributions along the height of coupled systems.

6. In most cases, the flexural strength of coupling beams governs the wind design of coupled C-PSW/CF systems in mid-rise structures, and the flexural capacities of the walls are considerably higher than the demand.

7. From a design standpoint, in mid-rise structures, using the effective stiffness for checking drift limits in both uncoupled and coupled C-PSW/CF systems appears to be reasonable and conservative.

8. In wind design of C-PSW/CF systems, the coupling beam-to-wall, wall-to-foundation, wall-to-wall connections (plate splices) are designed based on the required forces, rather than doing a capacity-based design, which would be done for a structure governed by seismic loading.

REFERENCES

Abaqus (2016), Abaqus Version 6.16, Analysis User's Manuals. Providence, RI, USA; *Dassault Systemes Simulia Corporation*, 2016.

Agarwal, S., Broberg, M, and Varma, A.H. (2020), "Seismic Design Coefficients for Speedcore or Composite Plate Shear Walls—Concrete Filled (C-PSW/CF)," Purdue University, West Lafayette, Ind., https://doi.org/10.5703/1288284317125.

AISC (2016a), *Seismic Provisions for Structural Steel Buildings*, ANSI/AISC 341-16, American Institute of Steel Construction, Chicago, Ill.

AISC (2016b), *Specification for Structural Steel Buildings*, ANSI/AISC 360-16, American Institute of Steel Construction, Chicago, Ill.

AISC (2022a), *Seismic Provisions for Structural Steel Buildings*, Public Review Ballot 2, AISC 341-22, American Institute of Steel Construction, Chicago, Ill.

AISC (2022b), *Specification for Structural Steel Buildings*, Public Review Ballot 2, AISC 360-22, American Institute of Steel Construction, Chicago, Ill.

Anvari, A.T., Bhardwaj, S.R., Wazalwar, P., and Varma, A.H. (2020), "Performance-Based Structural Fire Engineering of Buildings with Concrete-Filled Composite Plate Shear Walls (CF-CPSW)," Charles Pankow Foundation & American Institute of Steel Construction, https://www.aisc.org/globalassets/aisc/research-library/final_report_cpsw_fire_design_cpf_03-18.pdf

ASCE (1988), "Wind Drift Design of Steel-Framed Buildings: State-of-the-Art Report," Task Committee on Drift Control of Steel Building Structures of the Committee on the Design of Steel Building Structures, *Journal of Structural Engineering*, Vol. 114, No. 9.

ASCE (2016), "Minimum Design Loads and Associated Criteria for Buildings and Other Structures," ASCE/SEI 7-16, American Society of Civil Engineers/Structural Engineering Institute, Reston, Va., https://doi.org/10.1061/9780784414248.

Broberg, M., Shafaei, S., Kizilarslan, E., Seo, J., Varma, A.H., Bruneau, M., and Klemencic, R. (2022), "Capacity Design of Coupled Composite Plate Shear Walls—Concrete Filled (C-CPSW/CF)," *Journal of Structural Engineering*, Vol. 148, No. 4, 04022022-1, https://doi.org/10.1061/(ASCE)ST.1943-541X.0003296.

Bruneau, M., Varma, A.H., Kizilarslan, E., Broberg, M.R., Shafaei, S., and Seo, J. (2019), "R-Factors for Coupled Composite Plate Shear Walls/Concrete Filled (CC-PSW/CF)," Charles Pankow Foundation & American Institute of Steel Construction, https://www.aisc.org/globalassets/aisc/research-library/pankow-aisc-r-factor-final-report-2019-07-19_website.pdf.

CIS (2017), "SAP2000: Integrated Finite Element Analysis and Design of Structures," *Computers and Structures*, Berkeley, Calif.

El-Tawil, S., Harries, K.A., Fortney, P.J., Shahrooz, B.M., and Kurama, Y. (2010), "Seismic Design of Hybrid Coupled Wall Systems: State of the Art," *Journal of Structural Engineering*, Vol. 136, No. 7, pp. 755–769, https://doi.org/10.1061/(ASCE)ST.1943-541X.0000186.

FEMA (2020), *NEHRP Recommended Seismic Provisions for New Buildings and Other Structures*, FEMA P-2082, Federal Emergency Management Agency, Washington, D.C.

Fisher, J. and West, M. (2003), *Serviceability Design Considerations for Steel Buildings*, Design Guide 3, 2nd Ed., AISC, Chicago, Ill.

JEA (2005), *Technical Guidelines for Seismic Design of Steel Plate Reinforced Concrete Structures: Buildings and Structures*, JEAG 4618, Japanese Electric Association, Tokyo, Japan.

Griffis, L. (1993), "Serviceability Limit States under Wind Load," *Engineering Journal*, AISC, Vol. 30, No. 1.

Ramesh, S. (2013), "Behavior and Design of Earthquake-Resistant Dual-Plate Composite Shear Wall Systems," PhD Dissertation, Purdue University, West Lafayette, Ind.

Sener, K. and Varma, A.H. (2014), "Steel-Plate Composite SC Walls: Experimental Database and Design for Out-of-Plane Shear," *Journal of Constructional Steel Research*, Vol. 100, pp. 197–210, http://dx.doi.org/10.1016/j.jcsr.2014.04.014.

Sener, K., Varma, A.H., and Seo, J. (2016), "Experimental and Numerical Investigation of the Shear Behavior of Steel-Plate Composite (SC) Beams without Shear Reinforcement," *Engineering Structure*, Vol. 127, pp. 495–509, https://doi.org/10.1016/j.engstruct.2016.08.053.

Shafaei, S., Varma, A.H., Broberg, M., and Seo, J. (2019), "An Introduction to Numerical Modeling of Composite Plate Shear Walls/Concrete Filled (C-PSW/CF)," *Proc. Structural Stability Research Council (SSRC) Conference*, April 2–5, St. Louis, Mo., https://www.researchgate.net/publication/342109098_An_introduction_to_numerical_modeling_of_composite_plate_shear_walls_concrete_filled_C-PSWCF.

Shafaei, S., Varma, A.H., Seo, J., and Klemencic, R. (2021a), "Cyclic Lateral Loading Behavior of Composite Plate Shear Walls/Concrete Filled (CPSW/CF)," *Journal of Structural Engineering*, Vol. 147, No. 10, 04021145-1, https://doi.org/10.1061/(ASCE)ST.1943-541X.0003091.

Shafaei, S., Varma, A.H., Broberg, M., and Klemencic, R. (2021b), "Modeling the Cyclic Behavior of Planar Composite Plate Shear Walls (CPSW)," *Journal of Constructional Steel Research*, Vol. 184, 106810, https://doi.org/10.1016/j.jcsr.2021.106810,

Varma, A.H., Shafaei, S., and Klemencic, R. (2019), "Steel Modules of Composite Plate Shear Walls: Behavior, Stability, and Design," *Thin-Walled Structures*, Vol. 145, 106384, https://doi.org/10.1016/j.tws.2019.106384.

Zhang, K., Seo, J., and Varma, A.H. (2020), "Local Buckling and Design for Axial Compression," *Journal of Structural Engineering*, Vol. 146, No. 4, https://doi.org/10.1061/(ASCE)ST.1943-541X.0002545.

Zhang, K., Varma, A.H., Malushte, S., and Gallocher, S. (2014), "Effects of Shear Connectors on the Local Buckling and Composite Action in Steel Concrete Composite Walls," *Nuclear Engineering and Design*, Vol. 269, pp. 231–239, http://dx.doi.org/10.1016/j.nucengdes.2013.08.035.

The Chevron Effect: Reserve Strength of Existing Chevron Frames

RAFAEL SABELLI and ERIC BOLIN

ABSTRACT

Recently an analysis model has been developed to address the large shear forces (the so-called "chevron effect") that can develop in the connection regions of chevron-braced frames (Fortney and Thornton, 2015, 2017; Hadad and Fortney, 2020). These shear forces (and the corresponding moments) are the result of the application of the brace forces at the beam flange, eccentric to the beam centerline. Prior to the presentation of these methods, such forces were not generally considered in design, without apparent incident. Sabelli and Saxey (2021) presented an alternative model that determines substantially higher resistance in these connections. Both models resolve the shear and moment within the connection region such that forces outside that region are consistent with those determined using a centerline model. Greater resistance can be determined if the flexural strength of braces and the beam outside the connection region are used to resist a portion of the chevron moment. This paper presents a complete plastic-mechanism strength of the chevron frame with yielding of the beam web due to the local shear forces. This complete plastic mechanism strength can confirm the adequacy of existing designs that did not consider the chevron effect.

Keywords: gusset plates, braced frames, truss connections, chevron braces, analysis.

INTRODUCTION

Recent publications (Fortney and Thornton, 2015, 2017; Hadad and Fortney, 2020) have drawn attention to potentially large shear forces in the beam web in the connection region of chevron-braced frames (the "chevron effect"). Members in the braced frame are typically designed using a centerline model where forces are in equilibrium at the point where the member centerlines meet (the "work point"). The chevron effect arises when the transfer of brace forces to the beam occurs along the beam flange, which is offset from the beam centerline. This eccentricity results in a moment along the length of the gusset and a corresponding shear in the beam web. Subsequently, Sabelli and Saxey (2021) presented an alternative model of internal forces that significantly reduces the required beam shear strength. They termed this model the Concentrated Stress Model (CSM) to distinguish it from the Uniform Stress Model (USM), the term they used to describe the Fortney and Thornton method (2015, 2017). The CSM is adapted from the "optimal plastic method," while the USM employs the "conventional plastic method" as described in the AISC *Steel Construction Manual*, Part 8 (2018). Sabelli

Rafael Sabelli, Director of Seismic Design, Walter P Moore, San Francisco, Calif. Email: rsabelli@walterpmoore.com (corresponding)

Eric Bolin, Senior Engineer, American Institute of Steel Construction, Chicago, Ill. Email: bolin@aisc.org

and Saxey presented design equations for both USM and CSM for new construction.

Prior to these publications, many building designs did not address such forces within the connection region, without apparent incident. Subsequently, Roeder et al. (2021) published an analysis of the seismic response of a complete frame, including flexural resistance at brace and beam connections. This analysis showed that (at least in the inelastic drift range) the local stresses in the beam web in the chevron-connection region were low. As such, there exists some reserve capacity in the chevron frame not accounted for in the CSM and USM methods.

This paper presents two methods for determining the adequacy of existing chevron beams not designed for this local effect. The first is an "internal mechanism" based on the CSM stress distribution. The second method is an "external mechanism," which includes the CSM strength and, in addition, takes advantage of the full plastic mechanism strength. This mechanism requires rotation at the beam-to-column connections and at each end of each brace. The authors consider the CSM method better suited for design of new construction due to both its relative simplicity and its independence from reliance on moments in adjoining members. The full-plastic-mechanism method is presented only as a method to check existing construction.

INTERNAL MECHANISM

Sabelli and Saxey (2021) provide guidance for beam selection and gusset sizing that ensures adequacy using CSM evaluation. The CSM methods can also be used to establish simple formulae for evaluating existing connection designs.

This approximate method is based on determining the gusset plate length required to develop the sum of the horizontal components of the brace forces.

The chevron moment is:

$$M_{ch} = \frac{d_b}{2} \sum F_{br} \cos\theta \tag{1}$$

where

F_{br} = brace axial force, kips
d_b = beam depth, in.
θ = brace angle, with respect to the horizontal, degrees

If no other information is available, the sum of the horizontal components of the brace forces can be assumed to be the sum of the axial forces in the beam segments adjoining the connection (which may be presented in the design drawings):

$$\sum F_{br} \cos\theta = \sum P_u \tag{2}$$

The shear in the beam due to the chevron moment is:

$$V_u = \frac{M_{ch}}{e_z} \tag{3}$$

where

L_g = gusset plate length, in.
e_z = length of moment arm (see Sabelli and Saxey, 2021), in.
$= L_g - 2z \tag{4}$
z = length required to transfer for V_u from gusset to beam considering weld strength, gusset strength, web local yielding, and web crippling.

For the USM, the moment arm length e_z is assumed to be $\frac{1}{2}L_g$. For the CSM, it is longer; for a rough estimate it may be assumed to be $0.8L_g$. This estimate must ultimately be confirmed by evaluation of the connection for required weld size, gusset thickness, beam shear strength, and web local yielding and web crippling. For new construction, Sabelli and Saxey present minimum gusset length equations based on these limit states.

The maximum force may be limited by the shear strength of the beam:

$$V_u = \phi V_n \tag{4}$$

where

ϕV_n = available shear strength of the beam determined in accordance with AISC *Specification* (2016) Chapter G, kips

This available shear strength should be reduced in cases in which the beam is required to resist shear in the gusset region due to gravity load or unbalanced vertical components of brace forces.

Thus, the approximate minimum gusset length for the CSM is:

$$L_g \geq 1.25 \frac{M_{ch}}{\phi V_n} \tag{5}$$

If the gusset does not meet this minimum length, the engineer may use the explicit evaluation presented by Sabelli and Saxey.

If the USM is used to evaluate the gusset length, the internal connection forces are consistent with conventional plastic method, which is likely consistent with the gusset and weld design. If the evaluation is made using the CSM, internal forces will be similar to the optimized plastic method, and connection forces may need to be investigated.

Chevron beams with only two braces connecting at the midpoint (i.e., beams in stacked V or stacked inverted V frames) can generally be shown to be adequate using this CSM method due to the design of the beam for the axial force corresponding to the brace forces. However, the gusset, welds, and local beam-web limit states must also have sufficient strength to transfer the moment with a force couple:

$$R_u \geq \frac{M_{ch}}{e_z} \tag{6}$$

This force couple is transferred in two zones, each approximately $z = \frac{1}{2}(L_g - e_z)$ in length. See Sabelli and Saxey (2021) for additional guidance.

EXTERNAL MECHANISM

It is possible to realize additional strength in the connection by taking advantage of the flexural strength of the frame members external to the connection. The development of a full plastic mechanism corresponding to beam shear yielding requires rotation at the beam-to-column connections and rotation at each end of each brace. If moment can be resisted at these locations and in these members, additional resistance to the formation of the plastic mechanism can be realized in the system.

The following is a derivation of the complete plastic mechanism strength of both single-story V-type bracing and two-story X-type bracing. This procedure is recommended for verifying the capacity of existing connections. For new construction, providing a gusset of sufficient length such that the internal mechanism suffices is recommended over the calculation and coordination effort required to take advantage of any additional strength from brace flexure. It is expected that the majority of existing chevron connections have sufficient strength regardless of whether the chevron effect was explicitly checked in design.

Single-Story Frame

The plastic mechanism strength of a single-story chevron-braced frame is derived using the geometry shown in Figure 1. Point 1 is the center of the beam at midspan, point 2 is the point at which the brace crosses the gusset (the location of a potential plastic hinge), point 3 is the centerline of the beam at the end of the dimension e_x (the ends of the potential shear-yielding zone per Equation 4), and point 4 is the intersection of beam and column centerlines. Note that point 3 does not precisely align vertically with the gusset edge nor with point 2.

The complete plastic mechanism is shown in Figure 2, along with the associated rotations and displacements.

The proposed plastic mechanism entails shear yielding in the chevron zone, similar to the inelastic deformation of a shear governed eccentrically braced frame (EBF). As with the link in the EBF mechanism, the rotation of the gusset, θ_1, is centered on the original position of point 1, not the displaced position. As shown in Figure 2, the gusset merely rotates with the shear-deformed beam segment and is not required to yield for this mechanism to occur. A similar mechanism with flexural plastic hinges in the beam

at each end of the gusset zone in lieu of shear yielding was not investigated.

To simplify the analysis, the shear yielding is assumed to result in rotation at each end of the length e_z, rather than at the end of the gusset. For conditions with sufficient weld strength and resistance to local web limit states, the dimension e_z will approach the full gusset length L_g using the CSM, and thus the assumption is reasonable. For conditions in which the maximum possible dimension e_z is significantly shorter than the gusset length L_g due to limitations of weld or web strength (and in which the system has insufficient strength considering the plastic mechanism analysis), shear yielding may be accompanied by failure of the weld or a local web limit state. In any case, however, sufficient plastic mechanism strength determined using the dimension e_z demonstrates adequacy, although it neglects some internal work corresponding to the separation of gusset and flange in the regions outside of e_z.

In addition to the work associated with shear yielding, the plastic mechanism engages flexural plastic hinges in the braces and in the beam at the beam-to-column connection. These members are subject to significant axial force,
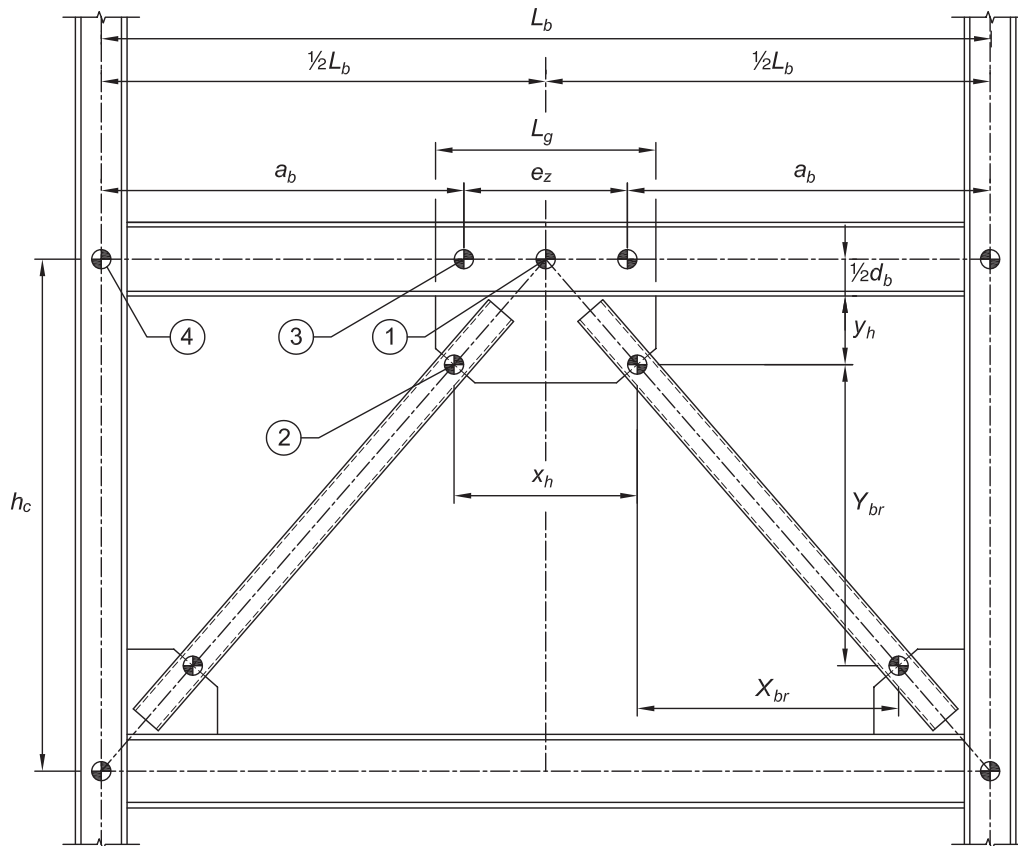

Fig. 1. Single-story chevron frame geometry.

and thus their flexural strength is reduced, as discussed in a later section.

From the geometry shown in Figure 1:

$$L_b = 2a_b + e_z \qquad (7)$$

Depending on the connection details, use of the CSM may be justified, or, more conservatively, this moment arm can be set to that of the USM.

From Figure 2:

$$\Delta_{x1} = \frac{d_b}{2}\gamma \qquad (8)$$

$$\Delta_{x4} = \Delta_{x1} \qquad (9)$$

$$\Delta_{x4} = h_c\theta_4 \qquad (10)$$

$$\Delta_{y2} = X_{br}\theta_2 \qquad (11)$$

$$\Delta_{y2} = \frac{x_h}{2}\theta_1 \qquad (12)$$

$$\Delta_{y3} = \frac{e_z}{2}\theta_1 \qquad (13)$$

$$\Delta_{y3} = a_b\theta_3 \qquad (14)$$

$$\gamma = \theta_1 + \theta_3 \qquad (15)$$

From Equations 11 and 12:

$$\theta_2 = \frac{x_h}{2X_{br}}\theta_1 \qquad (16)$$

From Equations 13 and 14:

$$\theta_3 = \frac{e_z}{2a_b}\theta_1 \qquad (17)$$

From Equations 15 and 17:

$$\gamma = \left(1 + \frac{e_z}{2a_b}\right)\theta_1 \qquad (18)$$

Using Equation 7, this simplifies to:

$$\gamma = \frac{L_b}{2a_b}\theta_1 \qquad (19)$$

From Equations 8 and 19:

$$\Delta_{x1} = \frac{L_b d_b}{4a_b}\theta_1 \qquad (20)$$

From Equations 9, 10, and 20:

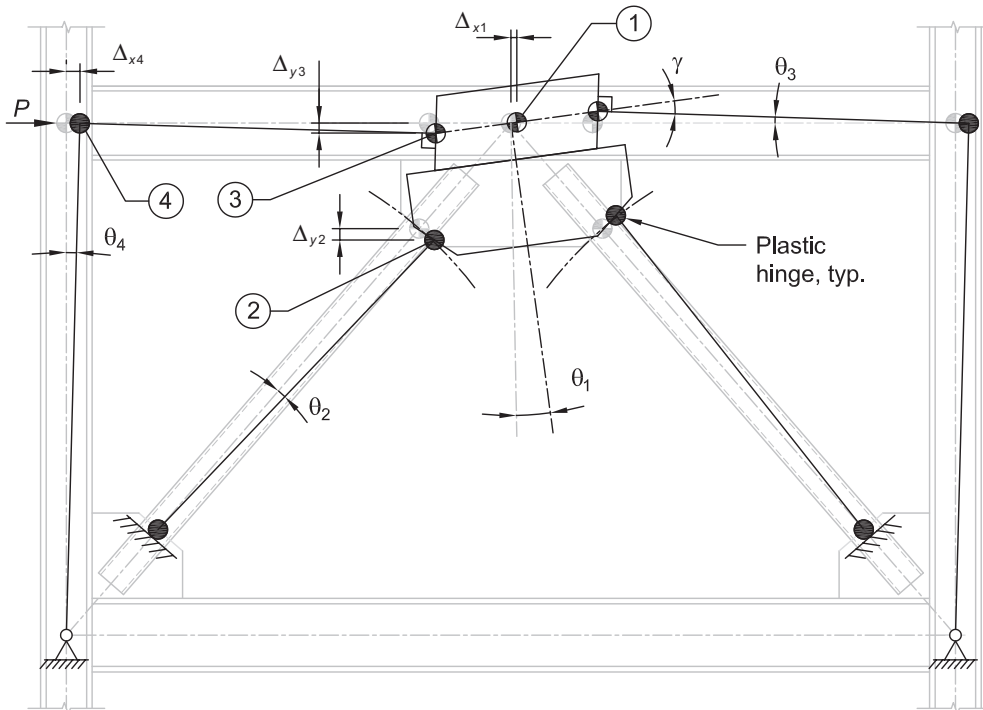$$\theta_4 = \frac{L_b d_b}{4a_b h_c}\theta_1 \qquad (21)$$

Fig. 2. Complete plastic mechanism for single-story chevron frame.

The external work applied to the frame is:

$$W_{external} = P\Delta_{x4} \tag{22}$$

which becomes:

$$W_{external} = P\frac{L_b d_b}{4a_b}\theta_1 \tag{23}$$

The internal work due to the frame mechanism is:

$$W_{internal} = \left[\gamma e_z V_n + 2|\theta_3 - \theta_4| M_{Pbm} + 2(2\theta_2 + \theta_1) M_{Pbr}\right] \tag{24}$$

where

M_{Pbm} = beam moment strength in the presence of axial force, kip-in

M_{Pbr} = brace moment strength in the presence of axial force, kip-in.

which becomes:

$$W_{internal} = \theta_1\left[\frac{L_b}{2a_b}e_z V_n + \frac{e_z}{a_b}\left|1 - \frac{L_b d_b}{2e_z h_c}\right| M_{Pbm} + 2\left(\frac{x_h}{X_{br}}+1\right) M_{Pbr}\right] \tag{25}$$

For $W_{external} = W_{internal}$:

$$P\frac{d_b L_b}{4a_b}\theta_1 = \left[\frac{L_b e_z}{2a_b}V_n + \frac{e_z}{a_b}\left|1 - \frac{L_b d_b}{2e_z h_c}\right| M_{Pbm} + 2\left(\frac{x_h}{X_{br}}+1\right) M_{Pbr}\right]\theta_1 \tag{26}$$

Solving for P:

$$P = \begin{bmatrix} \dfrac{2e_z}{d_b}V_n \\[2mm] +4\left|\dfrac{e_z}{d_b L_b} - \dfrac{2}{h_c}\right| M_{Pbm} \\[2mm] +\dfrac{8a_b}{L_b d_b}\left(\dfrac{x_h}{X_{br}}+1\right) M_{Pbr} \end{bmatrix} \tag{27}$$

This lateral force corresponds to yielding of the beam web in the connection region, as well as rotation of the brace ends and beam-to-column connection. If this lateral force is less than the required frame strength (or the capacity of the braces for seismic design), the chevron mechanism does not occur.

The beam moment, M_{Pbm}, is limited by the moment capacity of the beam end connection. This term can be neglected from Equation 27 to avoid having to check the moment capacity of the beam connection. If the plastic mechanism strength of the braces alone is insufficient to resist the forces, this term can be taken into consideration. The braces and their connections should be evaluated for the moment being transferred to them.

Two-Story Frame

The two-story plastic mechanism strength is derived using the geometry shown in Figures 3 and 4. The two-story frame has two differences compared to the single story. First, the internal work of the frame is supplemented by two additional braces. The beam contributions from both shear yielding at the chevron connection and flexural hinges at the column connection are the same as in the single-story case. Second, the external work contains contributions from loads at each of the two stories.

The external work applied to the frame is:

$$P_{ef} = P_1 + P_2\left(\frac{h_{c1}+h_{c2}}{h_{c1}}\right) \tag{29}$$

$$W_{external} = P_{ef}\Delta_{x4} \tag{30}$$

Combining Equations 10, 21, 29, and 30:

$$W_{external} = P_{ef}\frac{d_b L_b}{4a_b}\theta_1 \tag{31}$$

The internal work due to the frame mechanism is similar to that for the one-story mechanism (Equation 25), with the exception that two additional braces participate:

$$W_{internal} = \theta_1\left[\frac{L_b e_z}{2a_b}V_n + \frac{e_z}{a_b}\left|1 - \frac{L_b d_b}{2e_z h_c}\right| M_{Pbm} \right. \tag{32}$$

$$\left. + 2\left(\frac{x_{h1}}{X_{br1}}+1\right) M_{Pbr1} + 2\left(\frac{x_{h2}}{X_{br2}}+1\right) M_{Pbr2}\right]$$

Thus

$$P_{ef} = \begin{bmatrix} \dfrac{2e_z}{d_b}V_n \\[2mm] +4\left|\dfrac{e_z}{d_b L_b} - \dfrac{2}{h_c}\right| M_{Pbm} \\[2mm] +\dfrac{8a_b}{L_b d_b}\left(\dfrac{x_{h1}}{X_{br1}}+1\right) M_{Pbr1} \\[2mm] +\dfrac{8a_b}{L_b d_b}\left(\dfrac{x_{h2}}{X_{br2}}+1\right) M_{Pbr2} \end{bmatrix} \tag{33}$$

As with the one-story mechanism, this lateral force is compared to the forces corresponding to the required frame strength (or the capacity of the braces for seismic design).

Approximate Method

While Equations 27 and 33 are not complicated, for many cases, the contribution from the beam is fairly small, and the distinction between certain horizontal dimensions has negligible effect. A simpler version of Equation 27 can produce conservative values for rapid preliminary checks.

Setting

$$X_{br} \approx a_b \tag{34}$$

and

$$x_h \approx e_z \tag{35}$$

the amplification of the brace end moment becomes negligible for realistically small values of x_h/L_b.

Setting

$$M_{Pbm} = 0$$

for the one-story mechanism, the force that would cause the chevron mechanism is:

$$P \geq \frac{2e_z}{d_b} V_n + \frac{8}{d_b}\left(1 - \frac{a_b}{L_b}\right)M_{Pbr} \tag{36}$$

which can be conservatively reduced to:

$$P \geq \frac{2e_z}{d_b} V_n + \frac{4}{d_b} M_{Pbr} \tag{37}$$

If the lateral force does not exceed this value, the connection is adequate. A somewhat greater strength can be obtained form Equation 27.

For the two-story mechanism, the equivalent force per Equation 30 that would cause the chevron mechanism is:

$$P_{ef} \geq \frac{2e_z}{d_b} V_n + \frac{4}{d_b}(M_{Pbr1} + M_{Pbr2}) \tag{38}$$

Fig. 3. Two-story chevron frame geometry.

AVAILABLE FLEXURAL STRENGTH OF BRACES

The flexural strengths in the presence of axial force may be determined using AISC *Specification* Chapter H. Generally, braces will have axial forces such that AISC *Specification* Equation H1-1b will not apply. Equation H1-1a can be rewritten to solve for the available moment strength per *Specification* H1.3(a):

$$M_r \le \frac{9}{8}\left(1 - \frac{P_r}{P_c}\right)\phi M_{px} \tag{39}$$

Equation H1-3 can be rewritten to solve for this available moment strength:

$$M_r \le C_b M_{cx}\sqrt{1.0 - 1.5\frac{P_r}{P_{cy}} + 0.5\left(\frac{P_r}{P_{cy}}\right)^2} \tag{40}$$

For the mechanism in question, the brace undergoes reverse curvature with plastic hinging at each end. For this moment diagram:

$$
\begin{aligned}
C_b &= \frac{12.5M_{max}}{2.5M_{max} + 3M_A + 4M_B + 3M_C} \\
&= \frac{12.5M_u}{2.5M_u + 3(0.75M_u) + 4(0) + 3(0.75M_u)} \\
&= 1.79
\end{aligned}
$$

(*Spec.* Eq. F1-1)

For a preliminary evaluation, the brace flexural strength in the presence of axial force may be estimated as 25% of the full brace flexural strength. (This would correspond to approximately 75% axial utilization in Equation 39).
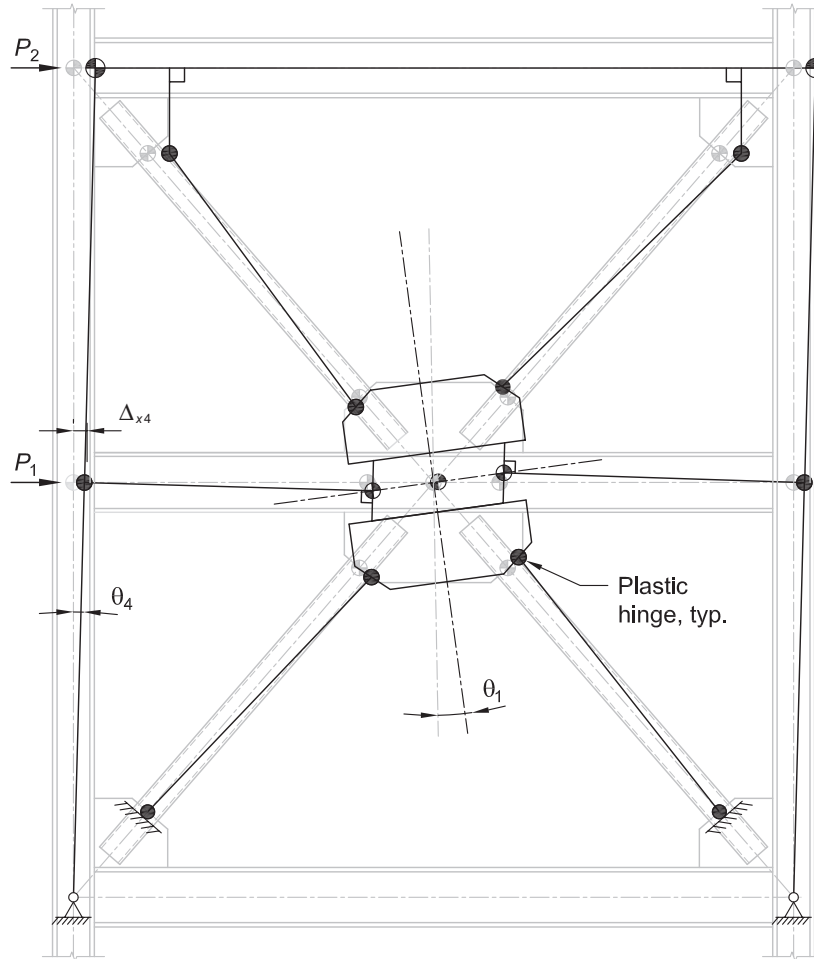

Fig. 4. External mechanism for two-story chevron frame.

EXAMPLE EVALUATION

Given:

The plastic mechanism strength will be used to evaluate an existing two-story chevron brace connection for which the available beam strength does not meet the required "chevron effect" forces determined using the Concentrated Stress Method. The connection detail and geometry of the frame are shown in Figures 5 and 6, respectively. The following brace dimensions are given for this example: $X_{br1} = 162$ in. and $X_{br2} = 164$ in. The brace forces and connection forces are summarized in Tables 1 and 2, respectively. Design is given for LRFD only. Both the beam and gusset plate are Grade 50 material. The braces are ASTM A500 Gr. C ($F_y = 50$ ksi).

Solution:

From AISC *Manual* Table 1-1:

W21×55
d = 20.8 in.
k_{des} = 1.02 in.
t_f = 0.522 in.
t_w = 0.375 in.

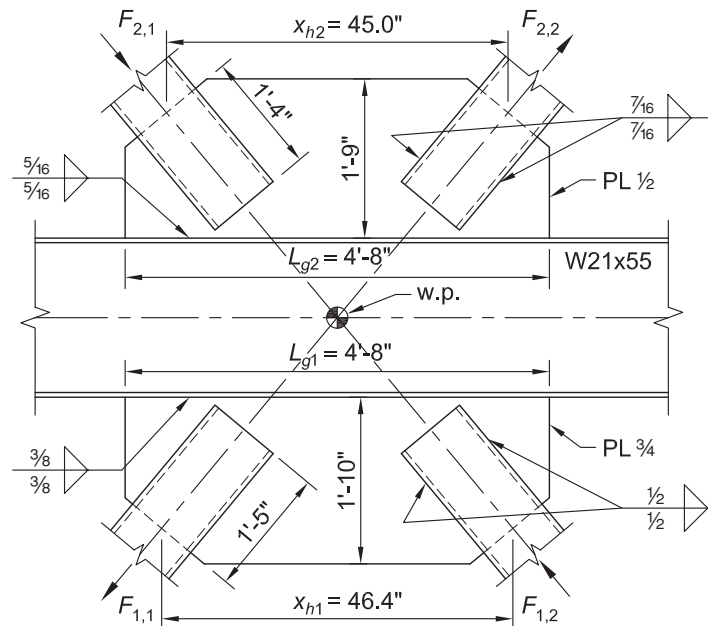From AISC *Manual* Table 6-1, for a W21×55:

ϕV_n = 234 kips

Fig. 5. Chevron connection detail.

Table 1. Summary of Brace Forces				
Brace	Brace Size	Brace Axial Force, F, kips	Shear Component, $F(\cos\gamma)$, kips	Normal Component, $F(\sin\gamma)$, kips
F1,1	HSS10×10×⅝	586	375	450
F1,2	HSS10×10×⅝	586	375	450
F2,1	HSS10×10×½	390	250	300
F2,2	HSS10×10×½	390	250	300

Table 2. Summary of Connection Forces			
	Gusset 1	Gusset 2	Combination (or Difference)
F_V, kips	750	500	1250
F_N, kips	0	0	0
M_f, kip-in.	7800	5200	13000

Concentrated Stress Method

First, the approximate method is attempted:

$$L_g \geq 1.25 \frac{M_{ch}}{\phi V_n} \tag{5}$$

$$= 1.25 \left(\frac{13{,}000 \text{ kip-in.}}{234 \text{ kips}} \right)$$

$$= 69.4 \text{ in.} > 56.0 \text{ in.} \quad \textbf{n.g.}$$

The gusset does not meet this requirement. The explicit method from Sabelli and Saxey (2021) is attempted for the bottom gusset.
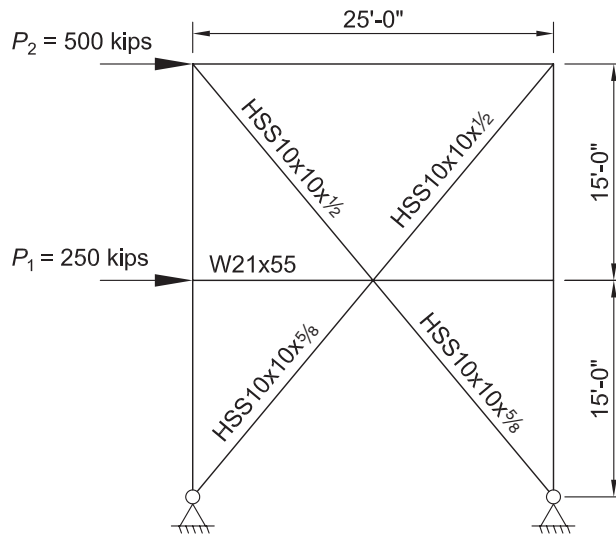

Fig. 6. Frame geometry.

From Sabelli and Saxey Equation 56:

$$V_{efTot} = \phi V_n - \left| \frac{F_{N1}}{2} - \frac{F_{N2}}{2} \right| - |V_m|$$
$$= 234 \text{ kips} - 0 - 0$$
$$= 234 \text{ kips}$$

From Sabelli and Saxey Equation 51:

$$V_{ef} = \frac{M_f}{M_{Tot}} V_{efTot}$$
$$= \left(\frac{7,800 \text{ kip-in.}}{13,000 \text{ kip-in.}} \right) (234 \text{ kips})$$
$$= 140 \text{ kips}$$

From Sabelli and Saxey Equation 39:

$$L_g > \frac{M_f}{V_{ef}} + \frac{V_{ef}}{\phi F_y t_g}$$
$$= \frac{7,800 \text{ kip-in.}}{140 \text{ kips}} + \frac{140 \text{ kips}}{0.90(50 \text{ ksi})(0.75 \text{ in.})}$$
$$= 59.9 \text{ in.} > 56.0 \text{ in.} \quad \textbf{n.g.}$$

A more precise (and less conservative) evaluation can be made by computing the largest possible value of the dimension e_z considering local web and gusset-yield limit states. Considering web local yielding, the minimum length, z, is determined using Sabelli and Saxey Equation 40:

$$z \geq \frac{L_g}{2} - \sqrt{\frac{L_g{}^2}{4} - \frac{M_f}{\phi_w F_y t_w}} - 5k$$
$$= \frac{56.0 \text{ in.}}{2} - \sqrt{\frac{(56.0 \text{ in.})^2}{4} - \frac{7,800 \text{ kip-in.}}{(1.00)(50 \text{ ksi})(0.375 \text{ in.})}} - 5(1.02 \text{ in.})$$
$$= 3.72 \text{ in.}$$

Considering web crippling, the minimum length, z, is determined using Sabelli and Saxey Equation 42:

$$z \geq \left[\frac{V_{ef}}{\phi_n 0.80 t_w^2 \sqrt{\frac{t_w}{EF_y t_f}}} - 1 \right] \left(\frac{d_m}{3} \right) \left(\frac{t_f}{t_w} \right)^{1.5}$$
$$= \left[\frac{140 \text{ kips}}{(0.75)(0.80)(0.375 \text{ in.})^2 \sqrt{\frac{0.375 \text{ in.}}{(29,000 \text{ ksi})(50 \text{ ksi})(0.522 \text{ in.})}}} - 1 \right] \left(\frac{20.8 \text{ in.}}{3} \right) \left(\frac{0.522 \text{ in.}}{0.375 \text{ in.}} \right)^{1.5}$$
$$= 1.91 \text{ in.}$$

Considering gusset yield, the minimum length, z, is determined using Sabelli and Saxey Equation 41:

$$z = \frac{L_g}{2} - \sqrt{\frac{L_g^2}{4} - \frac{M_f / \phi_t}{\sqrt{\left(F_y t_g\right)^2 - \left(\dfrac{F_V}{\phi_v 0.60 L_g}\right)^2}}}$$

$$= \frac{56.0 \text{ in.}}{2} - \sqrt{\frac{(56.0 \text{ in.})^2}{4} - \frac{\left(7{,}800 \text{ kip-in.} / 0.90\right)}{\sqrt{[(50 \text{ ksi})(0.75 \text{ in.})]^2 - \left[\dfrac{750 \text{ kips}}{(1.0)(0.60)(56.0 \text{ in.})}\right]^2}}}$$

$$= 5.72 \text{ in.}$$

Using the maximum length $z = 5.72$ in.:

$$e_z = L_g - 2z \tag{4}$$
$$= 56.0 \text{ in.} - 2(5.72 \text{ in.})$$
$$= 44.6 \text{ in.}$$

The reaction corresponding to this moment arm is:

$$R_u \geq \frac{M_{ch}}{e_z} \tag{6}$$
$$= \frac{13{,}000 \text{ kip-in.}}{44.6 \text{ in.}}$$
$$= 291 \text{ kips}$$

$$R_u = 291 \text{ kips} > V_{ef} = 140 \text{ kips} \quad \textbf{n.g.}$$

The CSM evaluation is discontinued at this point. If this check indicated adequacy, the other (top) gusset would be similarly evaluated, as would the weld and the local limit states of web local yielding and web crippling. See Sabelli and Saxey (2021) for additional information on the Concentrated Stress Method.

Plastic Method Strength

The required lateral force based on the frame loading is:

$$P_{ef} = P_1 + P_2 \left(\frac{h_{c1} + h_{c2}}{h_{c1}}\right) \tag{29}$$
$$= 250 \text{ kips} + 500 \text{ kips} \left(\frac{180 \text{ in.} + 180 \text{ in.}}{180 \text{ in.}}\right)$$
$$= 1{,}250 \text{ kip-in.}$$

$$V_p = V_{efTot}$$
$$= 234 \text{ kips}$$

Using the USM method:

$$e_z = 0.5 L_g$$
$$= 0.5(56.0 \text{ in.})$$
$$= 28.0 \text{ in.}$$

$$a_b = \frac{L_b - e_z}{2} \tag{7}$$

$$= \frac{300 \text{ in.} - 28.0 \text{ in.}}{2}$$

$$= 136 \text{ in.}$$

The flexural strength of the braces is checked in the presence of axial force. For the bottom and top braces, the available flexural and axial strengths are determined using AISC *Manual* Tables 3-13 and 4-4, respectively. The effective length for compression is conservatively assumed to be $L_c = 20$ ft.

Bottom braces (HSS10×10×⅝):

$\phi_b M_n = 275$ kip-ft

$\phi_c P_n = 706$ kips

Top braces (HSS10×10×½)

$\phi_b M_n = 228$ kip-ft

$\phi_c P_n = 583$ kips

The flexural strength of the braces is determined using Equations 39 and 40.

Bottom braces:

$$M_r \leq \frac{9}{8}\left(1 - \frac{P_r}{P_{cx}}\right)\phi M_{px} \tag{39}$$

$$= \frac{9}{8}\left(1 - \frac{586 \text{ kips}}{706 \text{ kips}}\right)(275 \text{ kip-ft})$$

$$= 52.6 \text{ kip-ft}$$

$$= 631 \text{ kip-in.}$$

$$M_r \leq C_b M_{cx}\sqrt{1.0 - 1.5\frac{P_r}{P_{cx}} + 0.5\left(\frac{P_r}{P_{cx}}\right)^2} \tag{40}$$

$$= 1.79(275 \text{ kip-in.})\sqrt{1.0 - 1.5\left(\frac{586 \text{ kips}}{706 \text{ kips}}\right) + 0.5\left(\frac{586 \text{ kips}}{706 \text{ kips}}\right)^2}$$

$$= 155 \text{ kip-ft}$$

$$= 1{,}860 \text{ kip-in.}$$

Use $M_r = 631$ kip-in.

Top braces:

$$M_r \leq \frac{9}{8}\left(1 - \frac{P_r}{P_{cx}}\right)\phi M_{px} \tag{39}$$

$$= \frac{9}{8}\left(1 - \frac{390 \text{ kips}}{583 \text{ kips}}\right)(228 \text{ kip-ft})$$

$$= 84.9 \text{ kip-ft}$$

$$= 1{,}020 \text{ kip-in.}$$

$$M_r \le C_b M_{cx} \sqrt{1.0 - 1.5\frac{P_r}{P_{cx}} + 0.5\left(\frac{P_r}{P_{cx}}\right)^2} \tag{40}$$

$$= 1.79(228 \text{ kip-in.})\sqrt{1.0 - 1.5\left(\frac{390 \text{ kips}}{583 \text{ kips}}\right) + 0.5\left(\frac{390 \text{ kips}}{583 \text{ kips}}\right)^2}$$

$$= 192 \text{ kip-ft}$$

$$= 2{,}300 \text{ kip-in.}$$

Use $M_r = 1{,}020$ kip-in.

$$P_{ef} = \frac{2e_z}{d_b}V_n + 4\left|\frac{e_z}{d_b L_b} - \frac{2}{h_c}\right|M_{Pbm} + \frac{8a_b}{L_b d_b}\left(\frac{x_{h1}}{X_{br1}} + 1\right)M_{Pbr1} + \frac{8a_b}{L_b d_b}\left(\frac{x_{h2}}{X_{br2}} + 1\right)M_{Pbr2} \tag{33}$$

$$= \frac{2(28.0 \text{ in.})}{20.8 \text{ in.}}(234 \text{ kips}) + 0 + \frac{8(136 \text{ in.})}{(300 \text{ in.})(20.8 \text{ in.})}\left(\frac{46.4 \text{ in.}}{162 \text{ in.}} + 1\right)(631 \text{ kip-in.})$$

$$+ \frac{8(136 \text{ in.})}{(300 \text{ in.})(20.8 \text{ in.})}\left(\frac{45.0 \text{ in.}}{164 \text{ in.}} + 1\right)(1{,}020 \text{ kip-in.})$$

$$= 630 \text{ kips} + 0 + 142 \text{ kips} + 227 \text{ kips}$$

$$= 999 \text{ kips} < 1{,}250 \text{ kips} \quad \textbf{n.g.}$$

Try the CSM method:

$$e_z = 44.6 \text{ in.}$$

$$a_b = \frac{L_b - e_z}{2} \tag{7}$$

$$= \frac{300 \text{ in.} - 44.6 \text{ in.}}{2}$$

$$= 128 \text{ in.}$$

$$P_{ef} = \frac{2e_z}{d_b}V_n + 4\left|\frac{e_z}{d_b L_b} - \frac{2}{h_c}\right|M_{Pbm} + \frac{8a_b}{L_b d_b}\left(\frac{x_{h1}}{X_{br1}} + 1\right)M_{Pbr1} + \frac{8a_b}{L_b d_b}\left(\frac{x_{h2}}{X_{br2}} + 1\right)M_{Pbr2} \tag{33}$$

$$= \frac{2(44.6 \text{ in.})}{20.8 \text{ in.}}(234 \text{ kips}) + 0 + \frac{8(128 \text{ in.})}{(300 \text{ in.})(20.8 \text{ in.})}\left(\frac{46.4 \text{ in.}}{162 \text{ in.}} + 1\right)(631 \text{ kip-in.})$$

$$+ \frac{8(128 \text{ in.})}{(300 \text{ in.})(20.8 \text{ in.})}\left(\frac{45.0 \text{ in.}}{164 \text{ in.}} + 1\right)(1{,}020 \text{ kip-in.})$$

$$= 1{,}000 \text{ kips} + 0 + 133 \text{ kips} + 213 \text{ kips}$$

$$= 1{,}350 \text{ kips} > 1{,}250 \text{ kips} \quad \textbf{o.k.}$$

The flexural strength provided by the braces is adequate to supplement the beam shear strength. Assuming the gusset and its welds are adequate to transfer the moment with the moment arm of e_z, the deficiency is only 1,250 kips − 1,000 kips = 250 kips. This is 250 kips/(133 kips + 213 kips) = 72% of the brace flexural strength determined earlier. Braces and their connections should be evaluated for this moment (in combination with the required axial strength) to show adequacy, as well as the corresponding shear.

For the brace-to-gusset welds at the bottom gusset plate:

$$M_u = 0.72(631 \text{ kip-in.})$$
$$= 454 \text{ kip-in.}$$

$$P_{eq} = P_u + 2\frac{M_u}{d}$$
$$= 586 \text{ kips} + 2\left(\frac{454 \text{ kip-in.}}{10 \text{ in.}}\right)$$
$$= 677 \text{ kips}$$

$$R_n = 1.392DL$$
$$= 1.392(8)(17 \text{ in.})(4 \text{ welds})$$
$$= 757 \text{ kips} > 677 \text{ kips} \quad \textbf{o.k.}$$

For the brace-to-gusset welds at the top gusset plate:

$$M_u = 0.72(1{,}020 \text{ kip-in.})$$
$$= 734 \text{ kip-in.}$$

$$P_{eq} = P_u + 2\frac{M_u}{d}$$
$$= 390 \text{ kips} + 2\left(\frac{734 \text{ kip-in.}}{10 \text{ in.}}\right)$$
$$= 537 \text{ kips}$$

$$R_n = 1.392DL$$
$$= 1.392(7)(16 \text{ in.})(4 \text{ welds})$$
$$= 624 \text{ kips} > 537 \text{ kips} \quad \textbf{o.k.}$$

The gusset connection to the beam flange must be able to transmit the force R_z over the length z.

LIMITATIONS AND FURTHER STUDY

The plastic mechanism strengths derived in this study have not been subject to verification by test or by nonlinear frame analysis. As such, they invite further investigation of the response of frames—in particular, the local behavior that follows the extension of shear yield beyond the length e_z. Additionally, the effects of the rotation capacity of different shapes would further inform the understanding of this mechanism.

CONCLUSIONS

The beam shear strength of an existing chevron bracing connections is typically acceptable whether or not the chevron effect was taken into consideration during design. If an existing chevron connection is deemed inadequate using the USM, additional strength may be found using the CSM. Alternatively, the complete plastic mechanism strength presented in this study can be used to confirm the adequacy of designs that did not consider the chevron effect. For this purpose, both complete and approximate equations are provided. Evaluations utilizing the CSM or the complete plastic mechanism should include assessment of the elements engaged to resist the chevron moment. For the CSM, this includes evaluation of the gusset and its weld for the stress concentrated at each end. For the plastic mechanism, this includes evaluation of the braces and their connections for the combination of axial force and moment. An example shows a frame for which the CSM considered on its own indicates significant insufficiency, but the complete plastic mechanism indicates adequacy.

SYMBOLS LIST

The following is a list of symbols used in this paper.

F_{br} — Brace axial force, kips

L_b — Beam span, in.

L_g — Gusset plate length, in.

M_{ch} — Chevron moment, kip-in.

M_{Pbm} — Beam moment strength in the presence of axial force, kip-in.

M_{Pbr} — Brace moment strength in the presence of axial force, kip-in.

M_{Pbr1}, M_{Pbr2} — For two-story frame, the brace moment strength in the presence of axial force for top and bottom braces, respectively, kip-in.

M_{px} — Major axis plastic moment strength, kip-in.

M_r — Required flexural strength, kip-in.

M_u — Required flexural strength. kip-in.

P — Horizontal force applied to the single-story frame, kips

P_c — Available axial strength, kips

P_{cy} — Available axial strength for out-of-plane flexural buckling, kips

P_{ef} — Effective horizontal force applied to the two-story frame, kips

P_r — Required axial strength, kips

P_1 — Horizontal force applied to the first story of a two-story frame, kips

P_2 — Horizontal force applied to the second story of a two-story frame, kips

V_u — Beam shear, kips

$W_{internal}$ — Internal work due to frame action, kip-in.

$W_{external}$ — External work applied to the frame, kip-in.

X_{br} — Horizontal distance between points where the brace ends cross the gusset plates, in.

X_{br1}, X_{br2} — For two-story frame, the horizontal distance between points where the brace ends cross the gusset plates of bottom and top braces, respectively, in.

Y_{br} — Vertical distance between points where the brace ends cross the gusset plates, in.

a_b — Length of beam from column centerline to e_z region, in.

d_b — Depth of beam, in.

e_z — Length of moment arm, in.

h_c — First-story frame height, in.

x_h — Horizontal distance from control point 2 (see Figure 1) of braces, in.

x_{h1}, x_{h2} — For a two-story frame, the horizontal distance from control point 2 (see Figure 1) of bottom and top chevron connections, respectively, in.

y_h — Vertical distance from beam flange to control point 2 (see Figure 1), in.

z — Length required to transfer V_u from gusset to beam considering weld strength, gusset strength, web local yielding, and web crippling, in.

Δ_{x1} — Horizontal displacement of control point 1 (see Figure 2), in.

Δ_{x4} — Horizontal displacement of control point 4 (see Figure 2), in.

Δ_{y2} — Vertical displacement of control point 2 (see Figure 2), in.

Δ_{y3} — Vertical displacement of control point 3 (see Figure 2), in.

γ — Shear angle of beam (see Figure 2)

θ — Brace angle, with respect to the horizontal, degrees

θ_1 — Rotation (see Figure 2)

θ_2 — Rotation (see Figure 2)

θ_3 — Rotation (see Figure 2)

θ_4 — Rotation (see Figure 2)

REFERENCES

AISC (2016), *Specification for Structural Steel Buildings*, ANSI/AISC 360-16, American Institute of Steel Construction, Chicago, Ill.

AISC (2018), *Steel Construction Manual*, 15th Ed., American Institute of Steel Construction, Chicago, Ill.

Fortney, P.J. and Thornton, W.A. (2015), "The Chevron Effect—Not an Isolated Problem," *Engineering Journal*, AISC, Vol. 52, No. 2, pp. 125–164.

Fortney, P.J. and Thornton, W.A. (2017), "The Chevron Effect and Analysis of Chevron Beams—A Paradigm Shift," *Engineering Journal*, AISC, Vol. 54, No. 4, pp. 263–296.

Hadad, A.A. and Fortney, P.J. (2020), "Investigation on the Performance of a Mathematical Model to Analyze Concentrically Braced Frame Beams with V-Type Bracing Configurations," *Engineering Journal*, AISC, Vol. 57, No. 2, pp. 91–108.

Roeder, C.W., Lehman, D.E., Tan, Q., Berman, J.W., and Sen, A.D. (2021), "Discussion—Investigation on the Performance of a Mathematical Model to Analyze Concentrically Braced Frame Beams with V-Type Bracing Configurations," *Engineering Journal*, AISC, Vol. 58, No. 1, pp. 1–9.

Sabelli, R. and Saxey, B. (2021), "Design for Local Member Shear at Brace Connections: Full-Height and Chevron Gussets," *Engineering Journal*, AISC, Vol. 58, No. 1, pp. 45–78.

Obliquely Loaded Welded Attachments Fatigue Categorization in Steel Bridges

Cem Korkmaz and Robert J. Connor

ABSTRACT

The detail category for base metal at the toe of transverse stiffener-to-flange and transverse stiffener-to-web fillet welds is defined as Category C′ in the current AASHTO *LRFD Bridge Design Specifications* (2020, 9th Ed.) and as Category C in the AREMA (2020) *Manual for Railway Engineering* and the AISC *Steel Construction Manual* (2017, 15th Ed.). These are often referred to as short attachments due to their very short length (<51 mm [2 in.]) in the direction of the primary stress range. Sometimes it is necessary to place a stiffener or a connection plate at an angle different than perpendicular to the web, such as in skewed bridges. Increases in the effective length of the stiffener along the flange in the longitudinal direction are seen as the plate is rotated away from being perpendicular to the web. The other extreme occurs when the stiffener is rotated completely 90° and is perfectly parallel to the web and the longitudinal stress range. In this instance, this is identical to the long attachment and classified as Category E (length > 102 mm [4 in.]). The current specifications and manuals, on the other hand, do not have classification on how to address the potential effects on fatigue performance of angles in between these two extremes. This paper summarizes finite element analysis studies based on local stress and structural hot-spot stress approaches that were conducted to investigate and classify welded attachments placed at angles other than 0° (transverse) or 90° (longitudinal) for a variety of stiffener geometries and thicknesses. This study includes new classification for incorporating the findings into the AASHTO *LRFD Bridge Design Specifications*, AREMA *Manual for Railway Engineering*, and the AISC *Steel Construction Manual*.

KEYWORDS: oblique, angular, fatigue categorization, welded attachments, transverse stiffener, local stress, hot spot.

INTRODUCTION

The American Association of State Highway and Transportation Officials' *LRFD Bridge Design Specifications*, 9th Ed. (AASHTO, 2020); the American Railway Engineering and Maintenance-of-Way Association's *Manual for Railway Engineering* (2020); and the American Institute of Steel Construction's *Steel Construction Manual*, 15th Ed. (2017), include a detail category for base metal at the toe of transverse stiffener-to-flange fillet welds and transverse stiffener-to-web fillet welds perpendicular to the web direction. In the AASHTO Specification Table 6.6.1.2.3-1, Condition 7.1, these details are identified as Category C′ (AASHTO, 2020), and the primary stress for this connection detail in the AREMA Manual is Category C in Table 15-1-8, Section 7 (AREMA, 2020), and

in the AISC *Manual* Appendix 3, Table A-3.1, Section 7 (AISC, 2017). In skewed steel girder bridges and a variety of other applications, it is occasionally necessary to angle the stiffener or connecting plate away from being perpendicular to the web. As the stiffener is rotated toward the web, thereby increasing the skew angle, the stiffener's effective "length" in the longitudinal direction rises. The most severe instance is when the stiffener is entirely rotated and made parallel to the primary stress range (90°). The detail category for base metal at the weld toe termination of welded attachments more than 102 mm (4 in.) in length and less than 25 mm (1 in.) in thickness is Category E in this situation. Clearly, if the stiffener is entirely rotated to be parallel with the web, it becomes similar to the long attachment, or Category E. These specifications, on the other hand, do not provide guidance on how to handle the potential impacts on fatigue performance of skew angles in between these two extremes.

This paper describes an analytical study focused on classifying the fatigue category for welded attachments placed at angles other than 0° or 90° for a variety of stiffener geometries and thicknesses using local stress and structural hot-spot stress methods. The results are then compared to data obtained through experimental fatigue testing to calibrate the recommendations to actual fatigue performance. Finally, the study includes recommendations for incorporating the findings into the current specifications and manuals.

Cem Korkmaz, PhD, Research Engineer, Lyles School of Civil Engineering, Purdue University, West Lafayette, Ind. Email: ckorkmaz@purdue.edu (corresponding)

Robert J. Connor, PhD, PE, Jack and Kay Hockema Professor, Lyles School of Civil Engineering, Purdue University, West Lafayette, Ind. Email: rconnor@purdue.edu

BACKGROUND

It is widely established that the fatigue life of welded attachments is affected by a variety of variables, some of which are difficult to quantify. Fisher et al. (1974) tested more than 150 beams and girders for fatigue strength of transverse stiffeners and attachments under constant amplitude loading to provide the best fit to the test data and limits of dispersion. These and other fatigue test data have confirmed the performance of the typical transverse stiffener as Category C′. Localized stress concentrations, the effect of weld toe defects, residual stresses, and other variables all have an effect on fatigue life. For the attachments discussed in this section, weld toe cracking is the predominant form of cracking. The likelihood of weld toe cracking is uniform regardless of the direction in which the detail is oriented as long as the toe is perpendicular to the applied stress range. In other words, the effects of residual stress and local weld toe defects are virtually identical regardless of the angle when the toe is perpendicular to the applied stress range. However, the local stress concentrations at the weld toe are significantly different as the length of the attachment varies, as evidenced by the reduction in fatigue resistance observed in Figure 1 taken from AASHTO LRFD Table 6.6.1.2.3-1, Condition 7.1 (AASHTO, 2020). As can be seen, the fatigue resistance of the detail reduces from Category C to E solely due to the increase in length. The residual stresses and defect distribution near the weld toe, on the other hand, remain effectively unchanged. Thus, the major element affecting the fatigue resistance of these details as the detail length increases is the stress concentration factor (SCF) near the weld toe.

In his experiments, Quadrato (2010) showed a decrease in fatigue life when the stiffener is obliquely loaded—in other words, when the skew angle was either 30° or 60°. However, there were only four experiments focused on the fatigue category for these welded attachments. Also, it is important to note here that after the Quadrato (2010) experiments, Quadrato et al. (2010) improved new cross-frame connection details for skewed supports as this was the primary focus of that work and was not explicitly focused on fatigue performance of a range of geometries of plate stiffeners. Nevertheless, very useful analytical and experimental data were obtained in that study that were consistent with the results of this more in-depth study on the hot-spot stresses of obliquely oriented stiffeners. Using split pipe bearing stiffeners, Quadrato et al. (2014) also showed an increase both in girder elastic buckling strength and fatigue life.

As indicated, when the welded attachment is rotated 90° and the length parallel to the stress range increases, the SCF also changes (increases) and transitions from the observed fatigue behavior compatible with Category C (or C′) to
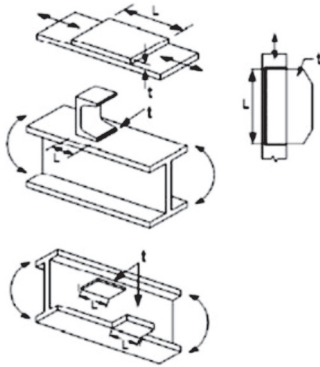
Description	Category	Constant A MPa³ (ksi)	Threshold (ΔF) MPa (ksi)	Potential Crack Initiation Point	Illustrative Examples
Section 7 - Longitudinally Loaded Welded Attachments					
7.1 Base metal in a longitudinally loaded component at a detail with a length L in the direction of the primary stress and a thickness t attached by groove or fillet welds parallel or transverse to the direction of primary stress where the detail incorporates no transition radius				In the primary member at the end of the weld at the weld toe	
$L < 51$ mm ($L < 2$ in.)	C	144×10^{10} (44×10^8)	69 (10)		
51 mm $\leq L \leq 12t$ or 102 mm (2 in. $\leq L \leq 12t$ or 4 in.)	D	72×10^{10} (22×10^8)	48 (7)		
$L > 12t$ or 102 mm ($L > 12t$ or 4 in.)					
$t < 25$ mm ($t < 1.0$ in.)	E	36×10^{10} (11×10^8)	31 (4.5)		
$t \geq 25$ mm ($t \geq 1.0$ in.)	E'	12.8×10^{10} (3.9×10^8)	17.9 (2.6)		
(Note: see Condition 7.2 for welded angle or tee section member connections to gusset or connection plates.)					

Fig. 1. Longitudinally loaded welded attachment (AASHTO, 2020).

Category	Threshold MPa (ksi)	Constant, A MPa^3 (ksi^3)	$A^{\frac{1}{3}}$ MPa (ksi)	Ratio of $A_C^{\frac{1}{3}}/A_x^{\frac{1}{3}}$
C′	83 (12)	144×10^{10} (44×10^8)	11300 (1640)	1.00
C	69 (10)	144×10^{10} (44×10^8)	11300 (1640)	Determined according to 49.5-mm (1.95-in.)-long welded attachment
D	48 (7)	72×10^{10} (22×10^8)	8970 (1300)	1.26
E	31 (4.5)	36×10^{10} (11×10^8)	7120 (1030)	1.59

Table 1. Ratio between the Estimated SCFs from Experimental Data for Detail Categories Normalized to Category C and C′

Category E. Unfortunately, estimating the SCF at the weld toe given the details of interest is a challenging problem. Fortunately, experimental data exist for both extremities of the skew angle of consideration, namely Category C (or C′) at 0° and Category E at 90°. Given that all other parameters affecting fatigue resistance effectively remain constant (i.e., weld toe defects, residual stresses, etc.), the ratios of the fatigue resistance curves for Categories C (or C′) and E can be used as "anchors" to which the estimated SCF at other angles can be calibrated.

There is some uncertainty whether Category C′ or Category C would be applicable based on the length of the attachment. For instance, a typical stiffener is around 13 mm (½ in.) thick; however, a 32-mm (1¼-in.)-thick bearing stiffener, plus the length added by the fillet welds, is over 50 mm (2 in.) long. It would appear that thicker stiffeners (e.g., bearing stiffeners) should be categorized as Category D; however, AASHTO (2020) makes no such distinction, and all transverse stiffeners are typically classified as C′ regardless of the actual toe-to-toe dimension in the longitudinal direction.

METHODOLOGY

Estimated Stress Concentration Factor Ratios

The purpose of this work was to conduct an analytical study in which the angle of the welded attachment was varied between 0° and 90° to determine the stress concentration factor (SCF). A mesh convergence analysis was conducted to verify that the ratio of estimated SCF ratios for Categories C′ and E remained constant. Again, it is not necessary to know the precise SCF value; rather, it is necessary to be able to anticipate the same ratio of fatigue life as that seen between the two categories that effectively "anchor" the extreme geometries and are based on experimental test results. As seen in Equation 1, the sole variable utilized to describe the difference in fatigue resistance across the various AASHTO details is the detail constant A. Due to the fact that the other parameters determining fatigue life are assumed to remain constant, the ratio of the cube roots of the detail constants is a good measure of the change in the SCF associated with Category C′ and E for a given value of N. In Table 1, this ratio is standardized to Category C′, and x symbolizes different categories (C′, C, D, or E).

$$\frac{(\text{SCF})_x}{(\text{SCF})_{C'}} = \frac{(\Delta F)_{C'}}{(\Delta F)_x} = \left(\frac{A_{C'}/N}{A_x/N}\right)^{1/3} = \frac{(A_{C'})^{1/3}}{(A_x)^{1/3}} \qquad (1)$$

While the actual SCF remains unknown, Table 1 indicates that the SCF associated with Category E is approximately 1.6 times that of Category C in the finite life portion of the *S-N* curve. As a result, the ratio of SCFs may be determined. These SCF values are also used in the second stage of the finite element analysis (FEA) to compare to the structural hot-spot stress approach.

Local Stress Finite Element Analysis Approach

The first step in conducting parametric research is to choose the specimen geometry to be examined. While other plate sizes might have been investigated, it was decided to employ components that were equivalent to those used in earlier NCHRP experiments by Fisher et al. (1974). The following plate sizes were modeled in detail:

- Flange width: 406.4 mm (16 in.)

- Flange thickness: 12.7 mm (0.5 in.) [7.2 mm was used in the original NCHRP experimental program (Fisher et al., 1974)]

- Flange length: 508 mm (20 in.)

- Attachment (stiffener) widths: 203.2, 254, and 304.8 mm (8, 10, and 12 in.) (transverse to web at 90°)

- Attachment (stiffener) thickness: 12.7 mm (0.5 in.)

- Weld thickness: 7.9 mm (5⁄16 in.)

The typical configuration is shown in Figure 2. As can be seen in the figure, the attachment was then rotated to evaluate the effect on the estimated SCF. The angles evaluated included 0°, 15°, 30°, 45°, 60°, 75°, and 90°. It is also important to note the stresses were transferred solely through the welds, the attachment plate was not directly tied to the flange.

ABAQUS (2017) was used to generate and evaluate finite element models of the aforementioned geometries.

All geometries were exposed to a 6.9 MPa (1 ksi) tensile stress on the gross section area throughout the plate's length. Three-dimensional models were built and subjected to quasi-static implicit analysis using large deformation theory.

A mesh convergence study was conducted with the goal of discovering a mesh with a constant ratio between the various estimated SCF ratios. The SCF ratios for the various meshes for longitudinal stresses on 203.2 mm (8 in.) wide stiffener are presented in Table 2, but in the final study, stiffeners with a width of 203.2, 254, and 304.8 mm (8, 10, and 12 in.) were examined. It should be mentioned
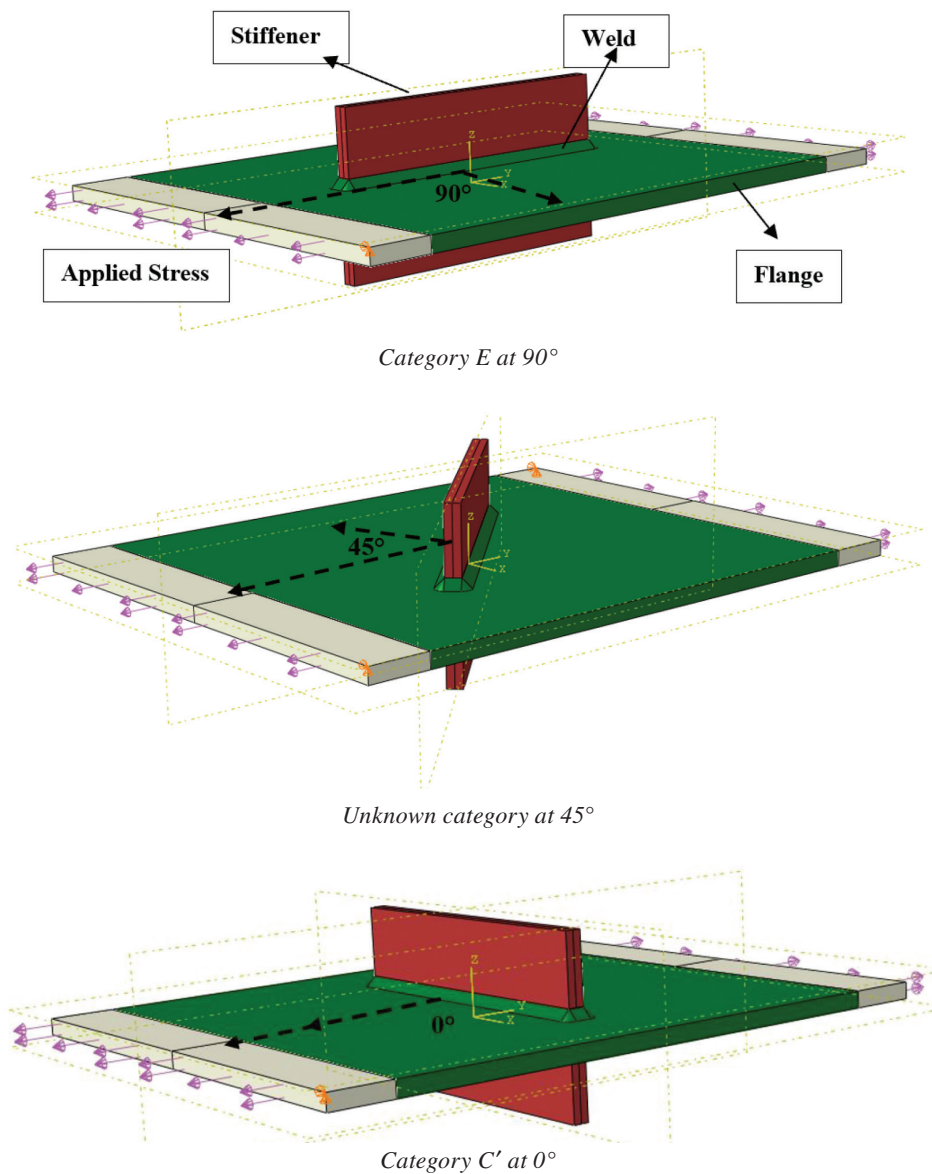

Category E at 90°

Unknown category at 45°

Category C′ at 0°

Fig. 2. Annotated sketches of attachments with different orientations modeled.

Table 2. Estimated SCF for the Various Meshes for Longitudinal Stresses of 200-mm (8-in.)-Wide Stiffener			
Angle (°)	3.81 mm (0.150 in.) Elements SCF Longitudinal Stress Range	3.18 mm (0.125 in.) Elements SCF Longitudinal Stress Range	2.54 mm (0.100 in.) Elements SCF Longitudinal Stress Range
90	2.37	2.65	2.85
75	2.40	2.58	2.80
60	2.38	2.44	2.59
45	1.94	2.12	2.30
30	1.78	1.80	1.98
15	1.67	1.75	1.88
0	1.63	1.72	1.85

Table 3. Ratio between the Estimated SCFs for the Various Meshes for 200-mm (8-in.)-Wide Stiffener—Each Angle Normalized to Category C′ (0°)			
Angle (°)	3.81 mm (0.150 in.) Elements Ratio to C′ (0°)	3.18 mm (0.125 in.) Elements Ratio to C′ (0°)	2.54 mm (0.100 in.) Elements Ratio to C′ (0°)
90	1.46	1.54	1.54
75	1.47	1.50	1.51
60	1.46	1.42	1.40
45	1.19	1.23	1.24
30	1.09	1.05	1.07
15	1.02	1.01	1.01
0	1.00	1.00	1.00

Table 4. Difference between 3.18 mm (0.125 in.) Mesh and 2.54 mm (0.100 in.) Mesh for 200-mm (8-in.)-Wide Stiffener			
Angle (°)	3.18 mm (0.125 in.) Elements Ratio to C′ (0°)	2.54 mm (0.100 in.) Elements Ratio to C′ (0°)	|Difference| (%)
90	1.54	1.54	0.25
75	1.50	1.51	0.77
60	1.42	1.40	1.40
45	1.23	1.24	0.65
30	1.05	1.07	2.01
15	1.01	1.01	0.01
0	1.00	1.00	0.00

that the authors also evaluated the SCF ratios using principal stresses and discovered that the findings were same as obtained when comparing the results using longitudinal stresses as expected.

Further mesh refinement resulted in higher estimations of the actual SCF, as predicted. However, as previously stated, the exact value of the SCF is unimportant. Rather than that, it is the ratio of the different SCF components that is significant. Thus, when the ratio of the SCF (shown in Tables 3 and 4) became virtually constant while the mesh size was changed, the mesh size was considered acceptable.

By examining Tables 3 and 4, it is clear that at a mesh size of 2.54 mm (0.100 in.), the ratio of estimated SCFs becomes virtually constant. With this mesh size, the average difference was 0.65%, while the maximum difference was 2%. As a result, this fine mesh size was determined to be suitable for the purposes of this study.

The mesh details of a typical design are seen in Figure 3. The finite elements used were 20-node quadratic brick elements with reduced integration (C3D20R, per ABAQUS designation). The quadratic formulation is classically utilized in the calculation of large strain gradients, such as the ones occurring at stress risers, in elastic problems.

The maximum longitudinal stresses in the flange were determined using finite element analysis, as seen in Figure 4. Because normal applied stresses were equal to 6.9 MPa (1 ksi), the stress concentration factor was equal to the highest FE longitudinal stress—that is, unlike main SCFs. (It should be mentioned that the authors assessed the ratios in the SCF for primary stresses and discovered that they were identical.)

Structural Hot-Spot Stress Approach

The second step in conducting FE research is to apply the structural hot-spot approach. The local stress approach as defined herein is similar to methods applied by the American Petroleum Institute (API) and American Welding Society (AWS) and is well documented in worldwide publications and readily available from Hobbacher at the International Institute of Welding (IIW) (Hobbacher, 2016). It is used extensively for the fatigue evaluation of tubular structures and plate-type structures with complex geometries by various industries, where there is no clearly defined nominal stress due to complicated geometric effects. The local stress approach recognizes that fatigue damage is caused by stress raisers that exist at details and attempts to quantify them by more refined analysis rather than classification.

This approach is based on assessment of the surface stress precisely at the weld toe of the joint. The baseline *S-N* curve is associated with butt weld or fillet weld details in a nominal stress field. In this method, the stress concentration factor accounts for effects associated with global geometry, and any local discontinuities and flaws are incorporated into the *S-N* curve. The reader is invited to review Niemi et. al (2018) for more information.

The same finite element models were used. In the hot-spot determination, the paths were drawn to obtain the base plate surface stresses. In Figure 5, the path lines were drawn from the maximum longitudinal stress location at the weld toe in the direction of stresses.

Because of the oblique orientation of the stiffeners, it is hard to use uniform meshes. According to Niemi et al. (2018) and Hobbacher (2016), when a nonuniform mesh is used, relatively fine meshes that are smaller than 0.4 times the thickness of the base plate should be preferred. The mesh sizes that are 3.18 mm (0.125 in.) and 2.54 mm (0.100 in.) utilized in this area are less than 0.4 times the thickness 5.08 mm (0.2 in.). Because there is no misalignment, the stress state is almost uniaxial, and the structural hot-spot stress can be estimated by extrapolating surface stress to the weld toe. Due to this nonuniformity and the complexity of the detail, the fine meshed models were preferred to be used to avoid mesh irregularities. The use of solid element modeling also enables explicit modeling of
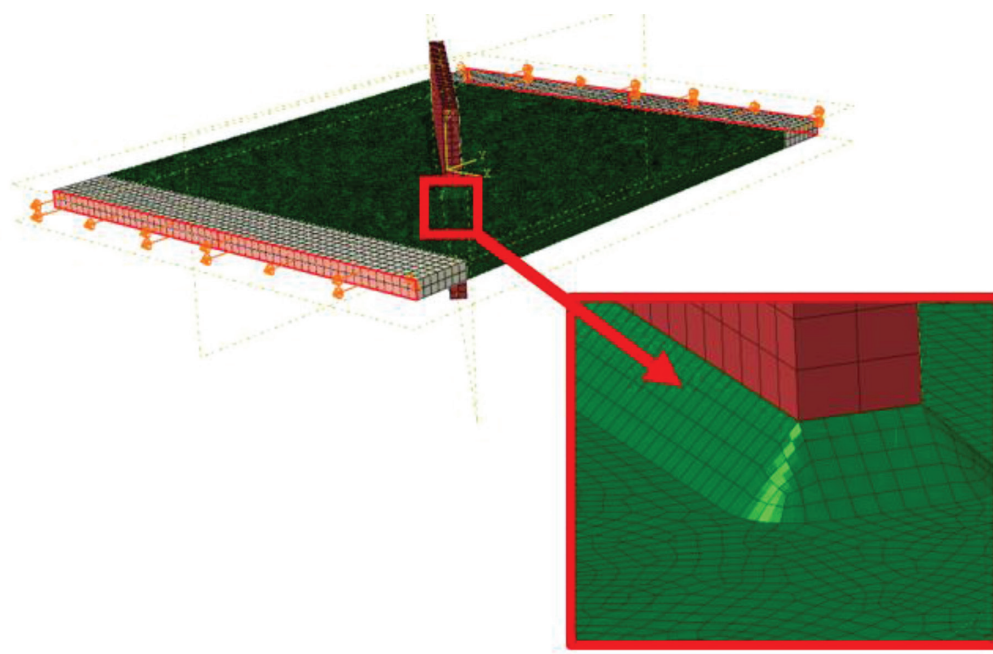

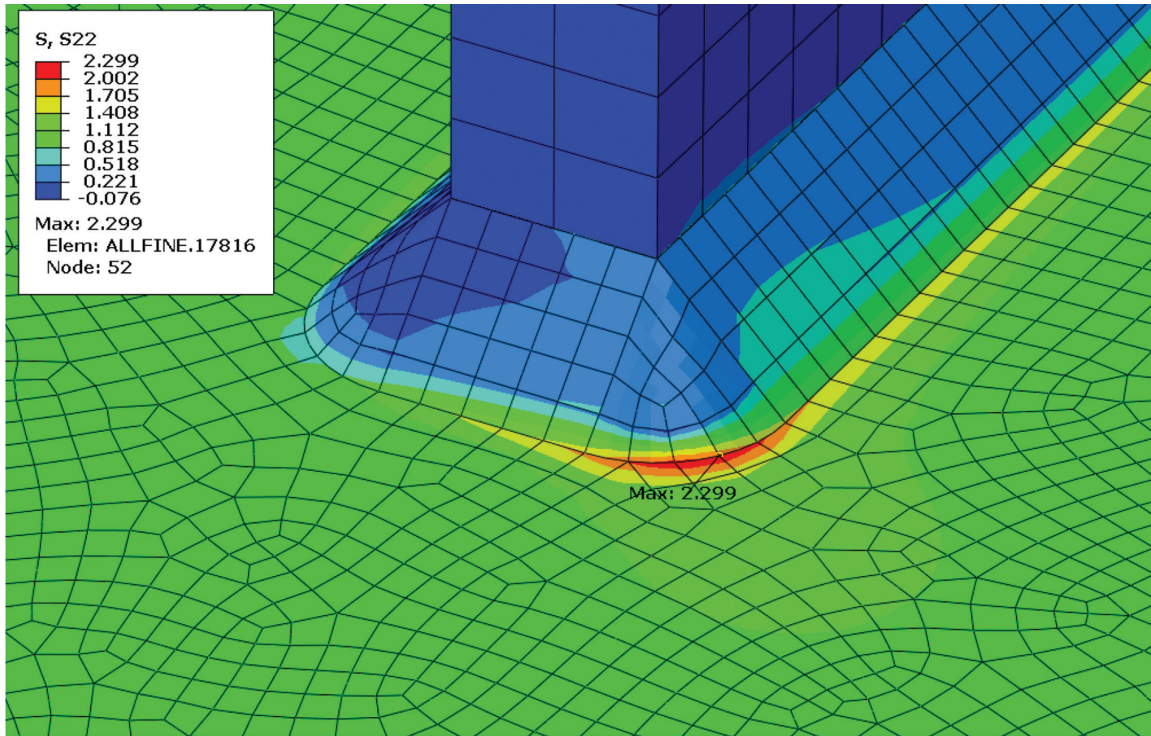*Fig. 3. Solid model (C3D20R) of the specimens.*

Fig. 4. Example of a solid model maximum longitudinal stresses (ksi) of the specimens.
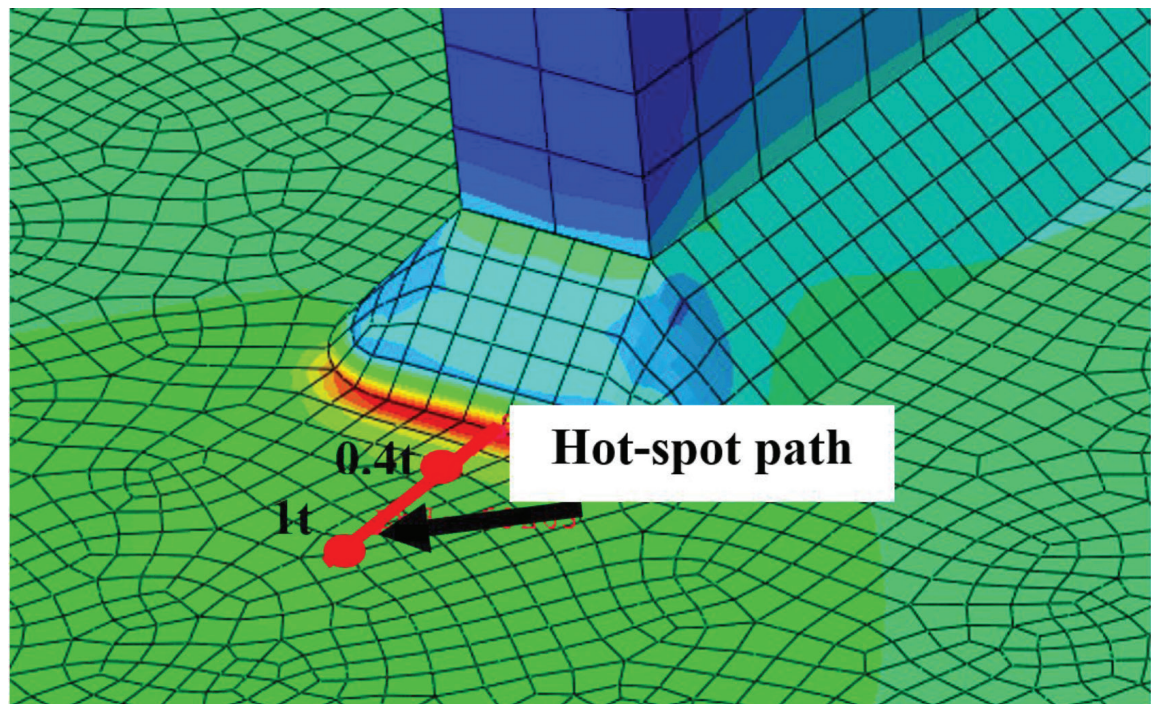

Fig. 5. Solid model maximum longitudinal stresses of the specimens.

Table 5. Structural Hot-Spot Stress Ratio between the Assessed and the Reference Detail		
Angle (°)	Hot-Spot Stress Ratio, $\sigma_{hs,assess}/\sigma_{hs,ref}$ for 3.18 mm (0.125 in.) Mesh Size	Hot-Spot Stress Ratio, $\sigma_{hs,assess}/\sigma_{hs,ref}$ for 2.54 mm (0.100 in.) Mesh Size
90	1.52	1.51
75	1.49	1.48
60	1.40	1.41
45	1.24	1.24
30	1.08	1.08
15	1.02	1.02
0	1.00	1.00

the weld geometry. When solid elements are used, Niemi et al. explain that when applied to Type "a" hotspots (only membrane stress), as seen in Equation 2, the linear extrapolation technique must make use of nodal stresses of 0.4 and 1.0 times of the base metal thickness, t, at the weld toe:

$$\sigma_{hotspot} = 1.67x\sigma_{0.4t} - 0.67x\sigma_{1t} \qquad (2)$$

Similar to the localized stress approach discussed earlier, the ratio between the structural hot-spot of the detail to be assessed, $\sigma_{hs,assess}$, and the structural hot-spot of the reference detail, $\sigma_{hs,ref}$, which is defined as Category C′, is important. As expected, further mesh refinement resulted in better estimations of these ratios. Two different fine mesh sizes are compared in Table 5 [3.18 mm (0.125 in.) and 2.54 mm (0.1 in.)]. It is seen that the ratios became virtually constant while the relatively fine mesh size was used.

By examining Table 5, it is clear that at a mesh size of 2.54 mm (0.1 in.), estimated results become virtually constant. With this mesh size, the maximum difference was less than 1%. As a result, this mesh size was determined to be suitable for the purposes of this study.

RESULTS

As stated before, the current study's goal is to estimate an appropriate AASHTO (2020) fatigue category for obliquely loaded welded attachments by comparing the ratio of estimated SCFs and hot-spot stresses to the value associated with Category C′ (90° perpendicular to the applied stresses). Other factors, such as residual stresses caused by weld defects, do not need to be explicitly considered because they are effectively constant regardless of the attachment angle. Additionally, it is known that there may be certain effects at welds that wrap around the stiffener as well as other small geometric effects not included in this research. These effects were deemed negligible, however, because they are

not explicitly considered in existing fatigue design or evaluation methodologies. Thus, the load-induced fatigue performance of these details can be estimated by comparing the calculated SCF calibration factor to the known fatigue resistance of welded stiffener connections transverse to the primary stress direction (Category C′) and longitudinally loaded welded attachments (Category E). The following variables are calculated for each geometry analyzed:

- *Longitudinal stress range, σ_L:* Total longitudinal force divided by the cross-sectional area of the plate. For all models, this equals the applied traction of 6.9 MPa (1 ksi).

- *Estimated stress concentration factor (SCF):* Stress concentration factors are defined as the maximum longitudinal stresses, σ_L, adjacent to the weld toe divided by remotely applied longitudinal (nominal) stress.

- *SCF calibration factor:* The factor used to scale the fatigue resistance of any attachment oriented between 0° (Category C′) and 90° (Category E) (shown in Equation 3):

$$\text{SCF calibration factor} = 1 \qquad (3)$$
$$+ \frac{\text{SCF}_{Angle} - \text{SCF}_{0(Category\ C')}}{\text{SCF}_{90(Category\ E)} - \text{SCF}_{0(Category\ C')}}$$
$$\times 0.59$$

The same approach was utilized to calibrate the factor for used with the structural hot-spot approach.

- *Principal, σ_P stress ranges:* Stress concentration factors and ratios are also obtained for the stress ranges of σ_P that are obtained from the FEA models for comparison purposes.

Due to the fact that the other parameters determining fatigue life remain constant, the ratio of the cube roots of
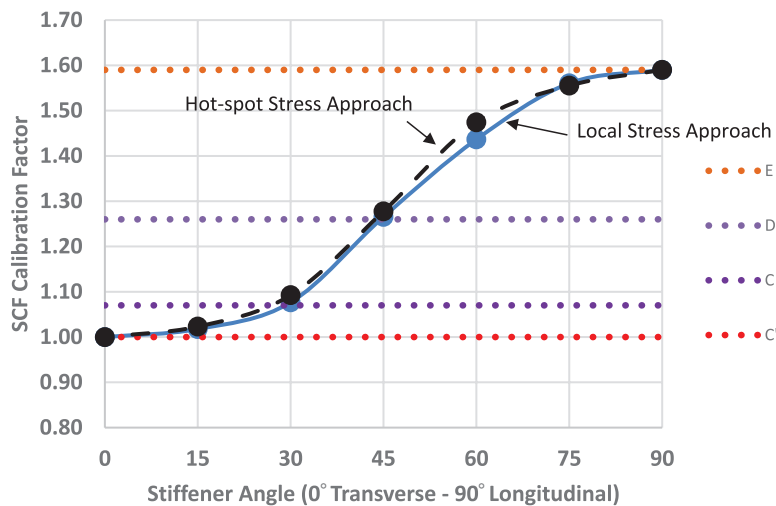
Table 6. Estimated SCF Values for Various Angles and Stiffener Lengths Based on FEA						
Angle (°)	200 mm (8-in.)-Wide Stiffener Longitudinal Stresses	200 mm (8-in.)-Wide Stiffener Principal Stresses	254 mm (10-in.)-Wide Stiffener Longitudinal Stresses	254 mm (10-in.)-Wide Stiffener Principal Stresses	305 mm (12-in.)-Wide Stiffener Longitudinal Stresses	305 mm (12-in.)-Wide Stiffener Principal Stresses
90	2.85	3.19	2.90	3.30	2.92	3.30
75	2.80	3.04	2.86	3.18	2.87	3.18
60	2.59	2.82	2.66	2.95	2.66	3.00
45	2.3	2.50	2.31	2.58	2.34	2.60
30	1.98	2.14	1.99	2.19	2.00	2.20
15	1.88	2.03	1.88	2.06	1.89	2.08
0	1.85	2.03	1.87	2.05	1.88	2.06

the detail constants is a reasonable indicator of the change in the SCF associated with Categories C and E for a given value of N. In Table 1, SCF is standardized to Category C (C′). Figure 6 presents (1) the factors based on AASHTO lower bound curves (shown as the horizontal dashed lines) and (2) the calibration factor of the estimated SCF from the FEA study normalized to the Category C′ and E. The dashed horizontal lines effectively represent lower bound fatigue resistance in AASHTO that are based on experimental data. The solid curved line represents the calibration factor of the SCF ratios from local stress approach, and the dashed curved line represents the factor of hot-spot stress approach obtained from the FEA when the stiffener angle

was changed. Where the dashed lines intersect with the curves, a reasonable estimate of the angle at which fatigue resistance falls into the next *lower* category is obtained. In other words, any values that lie below the dashed Category E line but above the dashed Category D line are best categorized as Category E. The same is true for Categories C/C′ and D.

As stated, Table 6 was generated through FEA and presents the predicted results [as reference to a nominal stress of 6.9 MPa (1 ksi)] for various angles; stiffener lengths of 200, 254, and 305 mm (8, 10, and 12 in.); and stresses (i.e., longitudinal, and principal). Comparing the SCF ratios in Table 6 for a given angle but for different stiffener lengths

Fig. 6. SCF calibration factor of the estimated SCF and hot-spot stresses from the FEA study vs. AASHTO lower-bound fatigue curves.

Table 7. Ratio Estimated SCF Values for Various Angles Based on FEA Normalized to 0°						
Angle (°)	200 mm (8-in.)-Wide Stiffener Longitudinal Stresses	200 mm (8-in.)-Wide Stiffener Principal Stresses	254 mm (10-in.)-Wide Stiffener Longitudinal Stresses	254 mm (10-in.)-Wide Stiffener Principal Stresses	305 mm (12-in.)-Wide Stiffener Longitudinal Stresses	305 mm (12-in.)-Wide Stiffener Principal Stresses
90	1.54	1.57	1.55	1.61	1.56	1.61
75	1.50	1.50	1.53	1.56	1.53	1.55
60	1.42	1.39	1.43	1.44	1.42	1.46
45	1.23	1.24	1.24	1.26	1.25	1.26
30	1.05	1.06	1.06	1.07	1.06	1.07
15	1.01	1.00	1.01	1.01	1.01	1.01
0	1.00	1.00	1.00	1.00	1.00	1.00

shows that the length of the attachment (for the lengths considered) has no appreciable influence as expected. This observation is consistent with the experimental work by Fisher et al. (1974) in which attachments greater than 4 in. were characterized by Category E. Since stiffeners and connections plates will almost always be at least 102 mm (4 in.) or longer, the results apply to the vast majority of cases.

The range of predicted SCF ratios for the various angles and stiffener widths evaluated are shown in Table 7. (These data are also plotted in Figure 6 for SCF ratios based on longitudinal stresses.) The angle of a typical transverse stiffener is standardized to 0° (i.e., the stiffener is perpendicular to the web). As can be seen, at about 45°, the ratio in the SCF is nearly 1.26 when longitudinal stresses are considered (i.e., 1.232) and almost exactly 1.26 for when principal or von Mises stresses are considered. As a result, when the stiffener is at 45°, it is determined that Category D should offer a reasonable estimate of the fatigue life. Additionally, good agreement is seen when data for Category E are included.

As shown in Figure 6, the data indicate that once the stiffener is angled more than about 20° to 25°, the SCF increases above that associated with Category C′. This indicates that Category C′ may be unconservative and the fatigue resistance should be estimated with the next unique lower category (i.e., Category D). Clearly, many bridges would be affected by a reduction to Category D due to the sheer number of bridges built that are slightly skewed (i.e., just below 90°). In order to reduce the impact and a significant drop in fatigue resistance (i.e., from C′ to D), incorporating Category C for this range of angles was studied as will be discussed later.

Based on the AASHTO fatigue illustrations, Category C is applicable to "short" attachments that are 50 mm (2 in.) or less in length. While Category C and C′ share the same finite life characteristics, the constant-amplitude fatigue threshold (CAFL) for Category C′ is slightly higher. This is because Category C′ details are generally shorter than 50 mm (2 in.) and possess a slightly lower SCF. Note, the residual stresses and defect distribution at the weld toe would be expected to be the same for both C and C′. Thus, while the finite life portion can be estimated easily, the authors attempted to identify the angle at which the SCF of a stiffener (i.e., C′) equals that associated with C. This was done by comparing the estimated SCF ratios as the length of the attachment approached up to 50 mm (2.0 in.) in length. Figure 7 illustrates the model used to obtain this estimated SCF.

Table 8 presents the estimated SCF for two transverse stiffeners or attachments of different thickness attached to the flange with only fillet welds. While the SCF for the 13 mm (0.5-in.)-thick stiffener corresponds to Category C′, the 49.5 mm (1.95-in.)-thick stiffener corresponds to Category C. In other words, the SCF of 1.981 for the 1.95-in.-long attachment effectively represents that associated with Category C [i.e., a detail that is almost 50 mm (2 in.) long and hence at the limit of Category C]. By taking the ratio of these two SCFs and plotting the value on Figure 6, the angle at which Category C can be applied can be estimated. As can be seen, this angle corresponds to about 30°. It is also apparent from the data in Table 7 and as plotted in Figure 6, that between 0° and about 15°, there is only about a 1.5% change in the ratio when normalized to the SCF of Category C′. Hence, there is really no need to drop below

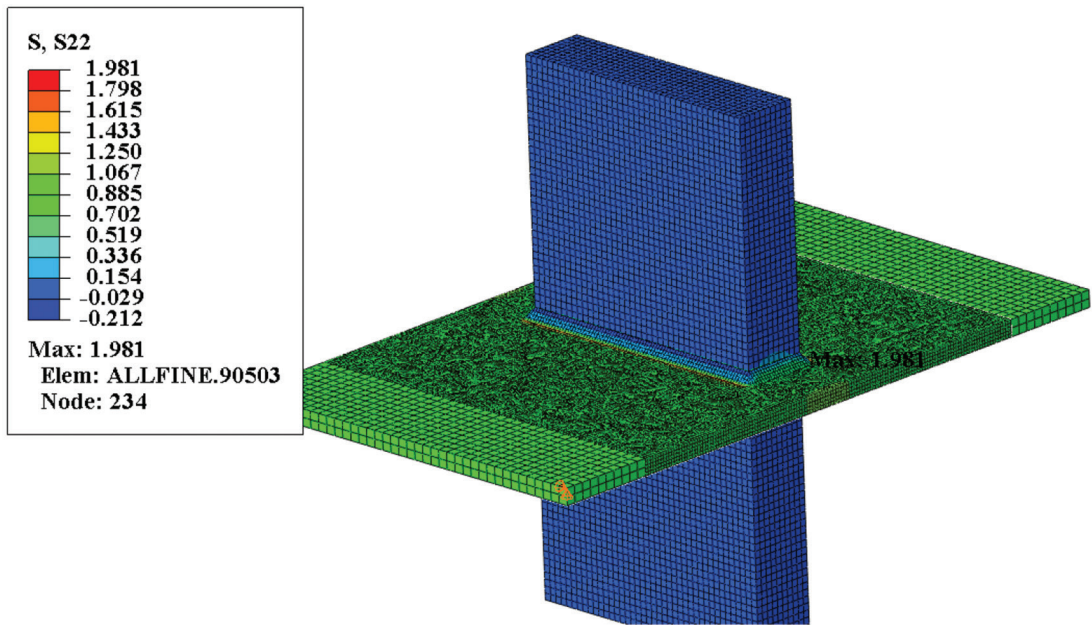| Table 8. Comparison of SCF Obtained from FEA for 12.7 and 49.5 mm-Thick Attachments		
Angle (°)	12.7 mm (0.5-in.)-Thick SCF	49.5 mm (1.95-in.)-Thick SCF
0	1.85	1.98

Fig. 7. FE model of 49.5 mm (1.95-in.)-thick stiffener to estimated SCF for Category C.

Category C′ for stiffeners angled between 0° and 15° and C can then be applied between 15° and 30°. Above 30° would thus apply.

$$\text{Category C (SCF)} = \frac{1.98}{1.85} = 1.07$$

It is also apparent that once the angle exceeds 45°, the increase in the SCF indicates that Category E is more applicable.

The final recommendations are summarized in Figure 8, where the proposed category versus skew angle is presented. It is noted that Figure 8 and throughout this study, the references to the skew angle are opposite from that typically used in AASHTO.

CONCLUSIONS

All stiffeners in the current research were 12.7 mm (0.5 in.) thick because this thickness is commonly utilized in steel bridge girders. Additionally, it is equivalent to the stiffener thickness used in the NCHRP experiments (Fisher et al., 1974) [7.2 mm (9/32 in.)]. Additionally, the stiffener's length was changed between 200, 254, and 305 mm (8, 10, and 12 in.). Additional FEA, and possibly experimental data,
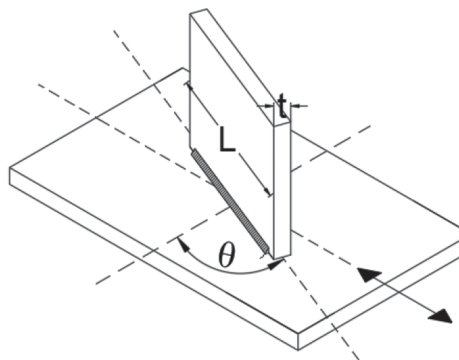
Description	Category	Constant A MPa³ (ksi³)	Threshold $(\Delta F)_{TH}$ MPa (ksi)	Potential Crack Initiation Point	Illustrative Examples
Base metal in a longitudinally loaded component at an obliquely oriented detail with an effective length L > 102 mm (4 in.) and a thickness t less than 25 mm (1 in.) attached by groove or fillet welds.				In the primary member at the weld toe	
$\theta \leq 15°$	C'	144 x 10¹⁰ (44 x 10⁸)	83 (12)		
$15° < \theta \leq 30°$	C	144 x 10¹⁰ (44 x 10⁸)	69 (10)		
$30° < \theta \leq 45°$	D	72 x 10¹⁰ (22 x 10⁸)	48 (7)		
$45° < \theta \leq 90°$	E	36 x 10¹⁰ (11 x 10⁸)	31 (4.5)		

Fig. 8. Recommended provisions for skewed plates based on the skew angle.

may be required for thicker stiffeners and associated angles of orientation. One possibility is to simply increase the recommendations for thicker stiffeners when they are used, but the authors feel this would require more research. Based on the results of the current study, it is noted that the transition between Categories C and C′ was best represented at an angle of 15°. The limit for Category D is 45°. Beyond 45°, it is recommended that higher angles are classified as Category E.

REFERENCES

AASHTO (2020), *LRFD Bridge Design Specifications (customary U.S. units)*, 9th Ed., American Association of State Highway and Transportation Officials, Washington, D.C.

ABAQUS (2017), Simulia, Dassault Systems, Boston, Mass.

AREMA (2020), *Manual for Railway Engineering*, American Railway Engineering and Maintenance-of-Way Association, Lanham, Md.

AISC (2017), *Steel Construction Manual*, 15th Ed., American Institute of Steel Construction, Chicago, Ill.

Fisher, J.W., Pedro, A.A., Yen, B.T., Klingerman, D.J., and Mcnamee, B.M. (1974), "Fatigue Strength of Steel Beams with Welded Stiffeners and Attachments," NCHRP Synthesis 147, National Academy Press, Washington, D.C.

Hobbacher, A.F. (2016), "Recommendations for Fatigue Design of Welded Joints and Components," *IIW Collections*, https://doi.org/10.1007/978-3-319-23757-2_7.

Niemi, E., Fricke, W., and Maddox, S.J. (2018), *Structural Hot-Spot Stress Approach to Fatigue Analysis of Welded Components Designer's Guide*, Springer Singapore, Singapore.

Quadrato, C. (2010), "Stability of Skewed I-Shaped Girder Bridges Using Bent Plate 227 Connections," PhD Dissertation, University of Texas, Austin, Texas.

Quadrato, C., Battistini, A., Frank, K., Helwig, T., and Engelhardt, M. (2010), "Improved Cross-Frame Connection Details for Steel Bridges with Skewed Supports," *Transportation Research Record: Journal of the Transportation Research Board*, Vol. 2200, No. 1, pp. 29–35.

Quadrato, C., Battistini, A., Helwig, T., Engelhardt, M., and Frank, K. (2014), "Increasing Girder Elastic Buckling Strength Using Split Pipe Bearing Stiffeners," *Journal of Bridge Engineering*, Vol. 19, No. 4, 04013017.

Guide for Authors

Scope *Engineering Journal* is dedicated to the improvement and advancement of steel construction. Its pages are open to all who wish to report on new developments or techniques in steel design, research, the design and/or construction of new projects, steel fabrication methods, or new products of significance to the uses of steel in construction. Only original papers should be submitted.

General Papers intended for publication should be submitted by email Margaret Matthew, editor, at **matthew@aisc.org**.

The articles published in the *Engineering Journal* undergo peer review before publication for (1) originality of contribution; (2) technical value to the steel construction community; (3) proper credit to others working in the same area; (4) prior publication of the material; and (5) justification of the conclusion based on the report.

All papers within the scope outlined above will be reviewed by engineers selected from among AISC, industry, design firms, and universities. The standard review process includes outside review by an average of three reviewers, who are experts in their respective technical area, and volunteers in the program. Papers not accepted will not be returned to the author. Published papers become the property of the American Institute of Steel Construction and are protected by appropriate copyrights. No proofs will be sent to authors. Each author receives three copies of the issue in which his contribution appears.

Manuscripts Manuscripts must be provided in Microsoft Word format. Include a PDF with your submittal so we may verify fonts, equations and figures. View our complete author guidelines at **aisc.org/ej**.